

SMIT, JACOBA ELIZABETH

A STUDY OF LASER INDUCED AND OTHER SIMILAR
PERIODIC SURFACE STRUCTURES USING OPTICAL TECHNIQUES

MSc

UP

1995

**A study of laser induced and other similar
periodic surface structures using optical
techniques.**

by

Jacoba Elizabeth Smit

Submitted in partial fulfilment of the requirements for the degree

Msc (Physics)

in the

Faculty of Science

University of Pretoria

Pretoria

October 1995

Supervisor: Prof D J Brink

A study of laser induced and other similar periodic surface structures using optical techniques.

by

Jacoba Elizabeth Smit

Submitted in partial fulfilment of the requirements for the degree

Msc (Physics)

in the

Faculty of Science

University of Pretoria

Supervisor: Prof D. J. Brink

In this study light scattering from periodically structured surfaces is investigated theoretically and experimentally. A mathematical model is developed which describes the diffraction characteristics of two examples of such surfaces, namely the regular grating-like micro structure on scales of the wing of the *Trichopusia orichalcea* moth, and the laser induced periodic surface (LIPS) structures formed on the surface of a semiconductor during irradiation by a pulsed high-power laser.

Predictions from these models are compared with experimental measurements using a conventional spectrometer (for the moth wing) and a novell ellipsometer-based technique (for LIPS).

‘n Studie van laser geïnduseerde en ander soortgelyke periodiese strukture met behulp van optiese tegnieke.

deur

Jacoba Elizabeth Smit

Voorgelê ter gedeeltelike vervulling van die vereistes vir die graad

Msc (Fisika)

aan die

Universteit van Pretoria

Studieleier: Prof D. J. Brink

In hierdie studie is die verstrooing van lig vanaf gestruktureerde oppervlakke teoreties en eksperimenteel ondersoek. ‘n Wiskundige model is ontwerp wat die diffraksie-eienskappe van twee voorbeelde van sulke oppervlakke, naamlik die periodiese mikrostruktuur op die vlerk van die *Trichoplusia orichalcea* mot, en die laser geïnduseerde periodiese oppervlak (LIPS) strukture wat gevorm word na bestraling met ‘n hoë-drywing laser, te verklaar.

Die voorspellings van hierdie modelle is met die eksperimentele metings vergelyk deur van ‘n gewone spektrometer (vir die mot) en ‘n ellipsometer gebaseerde tegniek (vir LIPS) gebruik te maak.

ACKNOWLEDGEMENTS

I would like to thank the following persons for their contributions towards the completion of this study:

My supervisor, Prof D. J. Brink for his guidance, support and constant encouragement.

Dr G. Myburg for the silicon samples and helpful discussions on the optical and electrical properties of semiconductors.

Prof M. E. Lee of the Electronmicroscopy Unit at the University of the North, Sovenga for providing the SEM-micrographs of the moth.

Messrs R. van Weele and G. Pretorius for technical assistance during this study.

Prof L. Strauss and Mrs R. Horak for the use of the computer facilities in the Exploratorium.

The Foundation for Research Development of South Africa for their financial assistance during this study.

The staff of the Physics department of the University of Pretoria for their interest, willingness to help and for their encouragement.

My parents, grandparents and sister for their support and encouragement.

CONTENTS

Chapter 1: Introduction	1
Part A: Background to the <i>Trichoplusia orichalcea</i> moth	1
Part B: Laser induced periodic surface structures	3
1 Theory of the LIPS-structures	3
2 Experimental observations	6
3 Techniques for observing the LIPS-structures	7
Chapter 2: Theory of light scattering from structured surfaces	10
1 Radiation from current distributions	10
1.1 Field equations	10
1.2 Linearity, superposition and boundary conditions	13
1.3 General solution to the field equations for a time-periodic field	15
1.4 Solution for fields arising from sources in an unbounded region	20
2 Diffraction and reflection from a rough surface with a regular pattern	21
2.1 The Aperture-field method	22
2.1.1 Introduction	22
2.1.2 Reflection of a plane wave by an infinite perfectly conducting plane surface	23
2.1.3 The Current-distribution method	26
2.1.4 The Fraunhofer region	28
2.1.5 Generalisation of the Silver formulation	31
Chapter 3: Mathematical modelling of the wing of the <i>Trichoplusia orichalcea</i> moth	33
1 Physical dimensions of the wing	35
2 Geometry of the wing	36
3 Further generalisations	42
4 Position vector (\vec{r}) of an arbitrary point on the wing	44
5 The directions of the input and output beams	46
6 The electric and magnetic fields	47
6.1 The polarized external electric field	47
6.2 Incidence and scattering from the local surface	49
6.3 The external scattered electric field	50
6.4 The incident and scattered magnetic fields	51
7 Solution to the Stratton-Silver-Chu integral	52
Chapter 4: Mathematical modelling of the laser induced periodic surface structures	57
1 Geometry of the LIPS-structure	57
2 The surface normals	58
3 The direction of the input and output beams	59
4 The height of the structure	60
5 The refractive index for silicon	62
5.1 The refractive index in the absence of photo-induced carriers	62
5.2 The refractive index with the effect of photo-induced carriers included	63
6 Solution to the Stratton-Silver-Chu integral	67

Chapter 5: Measuring techniques and equipment	69
Part A: The wing of the <i>Trichoplusia orichalcea</i> moth	
1 Experimental set-up	69
2 Equipment	70
2.1 Monochromator	70
2.2 Photomultiplier	73
3 Experimental techniques	75
3.1 Procedure to measure the angular spread of light scattered by the wing	75
3.2 Procedure to measure the effect of wing orientation on diffraction efficiency	76
3.3 Procedure to measure the spectral distribution of light scattered from the wing	77
4 Calculation of the total power diffracted from the wing	78
Part B: The laser-induced periodic surface structures	
1 Experimental set-up	82
2 Equipment	84
2.1 The oscilloscope and photomultiplier	84
2.2 The photo diode	85
2.3 The ellipsometer	85
2.4 The ruby laser	89
3 Experimental techniques	90
3.1 Alignment of the He-Ne system	90
3.1.1 Alignment of the He-Ne beam from the laser to the entrance aperture of the ellipsometer	90
3.1.2 Calibration of the analyser and polarizer circles and the $\lambda/4$ -compensator	91
3.1.3 Sample alignment	92
3.2 Alignment of the ruby laser beam	93
3.2.1 Alignment of the He-Ne beam with the ruby beam	93
3.2.2 Procedure to align the ruby spot with the probe beam spot on the sample	94
3.3 Calibration of the ellipsometer transmission	95
4 Calculation of some properties of the silicon and GaAs samples	98
4.1 The energy densities and peak intensities	98
4.2 Refractive indices and oxide layer thicknesses of the samples	99
Chapter 6: Results and discussion	100
Part A: The wing of the <i>Trichoplusia orichalcea</i> moth	
1 Angular spread of light on the wing	100
2 Wing orientation	103
3 Spectral distribution	103
4 Dispersion of the scale material	105
5 Angle of incidence	105
6 Dimensional variations	107
7 Conclusion	109
Part B: The laser-induced periodic surface structures	
1 The carrier-lattice interaction	110
2 Results: Experimental and theoretical	111

Chapter 7: Conclusions118
Appendices119
Appendix A119
Appendix B122
Appendix C142
Bibliography155

CHAPTER 1

INTRODUCTION

Light scattering from periodically structured and rough surfaces is a well studied phenomenon. In this study optical diffraction from two examples of such surfaces will be considered, namely the regular micro structure of a scale on the wing of the *Trichoplusia orichalcea* moth, and the laser induced periodic surface structures formed on the surface of a semiconductor after irradiation by a ruby laser.

In this chapter a short background to the two topics will be given. For clarity the chapter is divided into two parts. Part A will concentrate on the moth and part B on the laser induced periodic surface structures. Two mathematical models based on the solution to the Stratton-Silver-Chu integral will be used to explain the observed optical characteristics. The derivation of this integral due to Silver will be discussed in chapter 2. Chapters 3 and 4 will concentrate on the mathematical models used. The experimental equipment, results and conclusions will be discussed in chapters 5, 6 and 7 respectively.

Part A:

Background to the *Trichoplusia orichalcea* moth

Coloration due to structural architecture is a common and well studied phenomenon throughout the animal world [Anderson T. F. and Richards A. G. (1942) pp. 748-758; Greenewalt C. H. *et al.* (1960) pp. 1005-1013; Mossakowski D. (1979) pp. 351-364; Ghiradella H. (1991) pp. 3492-3500]. Most of the colours are ultraviolets, blues, greens and sometimes copper, while the longer wavelength colours such as red are not well represented. Land [Land M. (1972) pp. 75-106] discussed some of the functions of

coloration in fish, birds and insects, namely camouflage, courtship, display, optical filters and tapetal reflectors.

Insect colours can be divided into two types, namely coloration due to pigmentation and structural coloration. The first type is the more common phenomenon, where colour is determined by the selective absorption of light by the pigments, or by reflection of light by the pigment giving metallic colours. Pigments are not involved in the second type. Instead, the coloration is determined by the reflection of light by minute structures like the lines of a diffraction grating [Ghiradella H. (1991) pp. 3492-3500] or multilayer reflectors [Land M. (1972) pp. 75-106].

By far the most research has been done on the colour effects ascribed to thin-film interference phenomena [Land M. (1972) pp. 75-106] due to the reflection of incident light from several alternating layers of low and high refractive index materials. Land suggested a refractive index of 1.56 for chitin in a system based on chitin and air. Morris [Morris R. B. (1975) pp. 149-154] showed that in some cases diffraction from regular lattice structures seemed to be responsible for the coloration.

Neville [Neville A. C. and Caveney S. (1969) pp. 531-562] did some research on the optical properties of beetle exocuticles. They investigated interference colours due to lamellar spacing and reflection of circularly polarized light. Little attention was given to polarization and directional properties of biological diffractive reflectors.

In this work the optical properties of the wings of a particular moth species, *Trichoplusia orichalcea*, having a prominent, highly reflective, metallic-gold patch on the wings, will be investigated. SEM-micrographs (see chapter 3, Fig. 3.1(a) and (b)) show that the scales on the wing consist of a herringbone structure arranged in parallel strips similar to *Diachrysis balluca* (previously known as *Plusia balluca*) mentioned by Ghiradella. It is noteworthy that coloration is not due to thin-film structures and one can therefore conclude that the optical properties should be primarily related to diffraction.

Part B:

Laser induced periodic surface structures

1. Theory of the LIPS-structures

Periodic surface structures resulting from interaction between continuous wave or pulsed laser beams with solids have been reported by many researchers, such as Young *et al.* and Emmony *et al.*, over the past two decades [Young J. F. *et al.* (1983) pp. 1155-1172, Emmony D. C. *et al.* (1973) pp. 598-600]. Sipe [Sipe J. F. *et al.* (1983) pp. 1141-1154] noted that these grating-like patterns appeared on the surfaces of various intrinsic and extrinsic semiconductors, metals and dielectrics when irradiated with continuous wave to picosecond laser sources between 0.53 and 10.6 μm . The structures can be permanent or transient. Emmony discussed a very good example of this type of damage on the germanium output mirror of a TEA CO₂ laser at 10.6 μm .

These induced ripples have a substantial similarity to the well-known Wood's anomalies and are therefore called "stimulated Wood's anomalies". When a lightbeam is incident on a surface, like a diffraction grating, light is reflected and diffracted from the surface (see Fig. 1.1(a)). Wood [Wood R. W. (1902) pp. 269-275] noted that the light diffracted into one order would exhibit a sharp dip in intensity and diffraction efficiency whenever another order at the same wavelength was being diffracted tangentially, i.e. at grazing angle along the grating surface (see Fig. 1.1(b)). These dips occur only for the p-polarization.

Fig. 1.2 shows the results of first order diffraction for a 590 lines/mm grating and a 3mW 632.8 nm He-Ne laser. The lower trace (p-polarization) shows the intensity for normal angle of incidence. The anomaly can be seen at a diffraction angle of 15.3°. The top trace shows the case for s-polarization. Note that no dip is present.

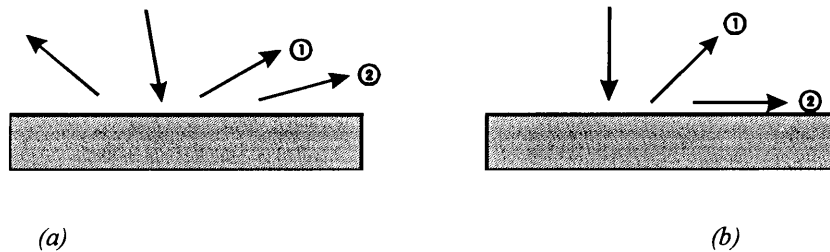


Fig. 1.1 (a) shows that light incident on a diffraction grating surface is reflected and diffracted into different orders. (b) shows the case for normal incidence.

Siegman shows a similar graph of the anomaly for the first order diffracted intensity in the vicinity of 30° diffraction angle for light incident at 2.5° off the normal (Fig. 1.3). For normal incidence only one dip occurs (Fig. 1.2), but now two dips are visible, corresponding to two wavelengths which become separately tangential to the grating surface in second order. In one case the second-order radiation is going to the right along the grating surface and in the other case to the left.

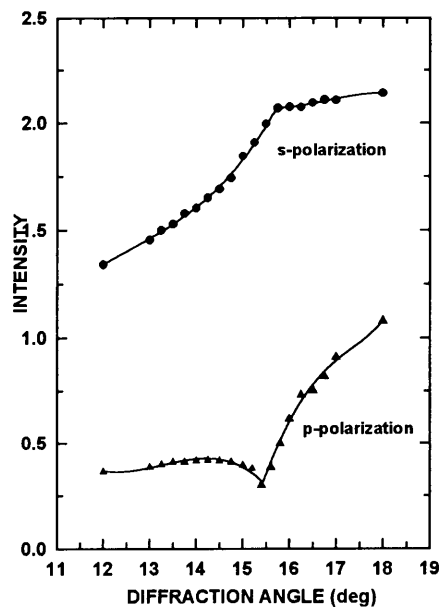


Fig. 1.2 The Wood anomaly for a 590 lines/mm grating. The upper curve shows the case for s-polarization and the lower curve the case for p-polarization.

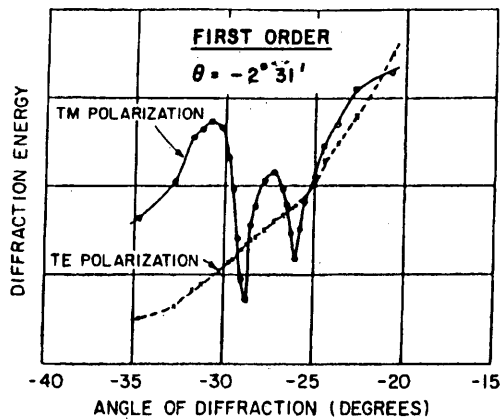


Fig. 1.3 The two Wood's anomalies near -30° for first order diffracted intensity for light incident 2.5° off normal incidence. Redrawn from Siegman [Siegman A. E. and Fauchet P. M. (1986) pp. 1390]

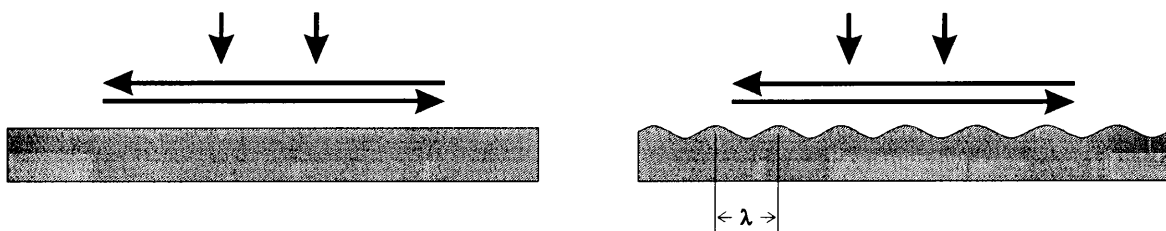


Fig. 1.4 (a) Some of the light incident on an object's surface is diffracted to the right and the left and a standing wave is formed on the surface. (b) The standing wave results in the formation of the LIPS-structure on the surface.

According to Siegman [Siegman A. E. and Fauchet P. M (1986) pp.1384-1403] the ripples appear as the result of a non-linear growth process which is initiated by the scattering of a small amount of light from the primary laser beam by random irregularities present on the illuminated surface. Wood's anomaly shows that the possibility of light diffracted along the surface is the highest. Light therefore gets diffracted to the right and the left along the surface and forms a standing wave (Fig. 1.4(a)). This standing wave has regions of high and low intensity repetitively. The semiconductor surface heats up in the high intensity regions and expands, while almost nothing happens in the low intensity regions. This forms a periodic surface structure with period equal to the wavelength of the laserlight (Fig. 1.4(b)). The surface then acts like a diffraction grating, scattering light in all

directions. Consider the grating equation $n\lambda = d \sin \theta$. When $\lambda = d$ and $n = 1$, i.e. first order diffraction, $\sin \theta = 1$ or $\theta = 90^\circ$. This causes a standing wave to form, the process gets repeated and the amplitude of the surface structure increases.

2. Experimental observations

Emmony [Emmony D. C. *et al.* (1973) pp. 598-600] found that for an opaque surface, like an unmelted semiconductor surface, the surface ripples will normally have a period close to the incident laser wavelength, λ , in the medium above the surface. Ehrlich [Ehrlich D. J. *et al.* (1982) pp. 630-632] reported that for molten semiconductor surfaces, layered or thin-film surfaces and metals, the ripple period depends significantly on the electromagnetic or waveguiding properties of the surface.

In general the surface ripples will take on a period such that one of their primary diffraction orders has a wave vector (\vec{k}) component along the surface. Ripples formed with linearly p-polarized light exhibit a spread of ripple \vec{k} vector direction distributed over 5° to 10° about the E-field direction. Brink [Brink D. J. and Smit J. E. (1993) pp.189-193] made use of the fact that the use of circularly polarized light at normal incidence often strongly inhibits the formation of ripples. Ripples will eventually form with circularly polarized light if the laser pulse energy or the number of repeated pulses is increased. The ripples will then have the same wavelength as the laser beam, but with \vec{k} vectors oriented in all directions along the surface.

In any of the above cases, if the primary beam moves away from normal incidence, the spontaneous surface structures changes to a more complex ripple pattern.

The ripple orientation are strongly dependent on incident angle. Young [Young J. F. *et al.* (1983) pp. 1155-1172] showed that for p-polarized light near normal incidence, two superimposed sets of ripples perpendicular to the polarization appear with a spacing of $1.06/(1 \pm \sin\theta) \mu\text{m}$ with θ the angle of incidence. The ripples become less distinct as θ

increases (Fig. 1.5(a) and 5(b)). For $\theta > 35^\circ$ a well-defined set of ripples appear parallel to the direction of the polarization with a spacing of $1.06/\cos\theta \mu\text{m}$ (Fig. 1.5(c)).

The ripple spacing also changes with increasing angle of incidence. Fig. 1.6 shows the ripple spacing for the three cases in Fig. 1.5. For s-polarized light as θ increases from 0° , a single set of ripples running perpendicular to the polarization with a spacing of $1.06/\cos\theta \mu\text{m}$ appears. For $\theta > 35^\circ$, two sets of ripples form which are neither parallel nor perpendicular to the polarization.

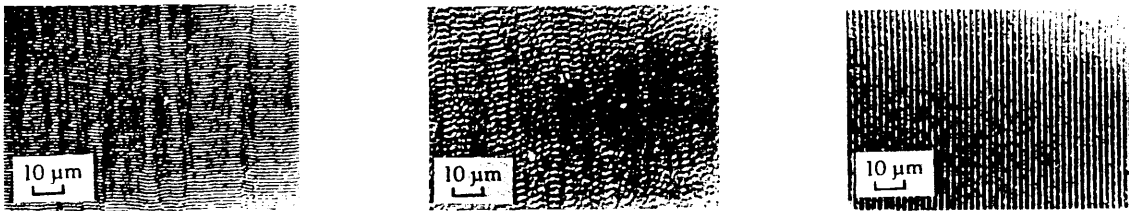


Fig 1.5 Photographs of the surface structure produced on Ge with p-polarized 1.06- μm radiation incident at angles of (a) 0° , (b) 30° , and (c) 60° . [Young J. F. *et al.* (1983) pp. 1159]

3. Techniques for observing the LIPS-structures

Since the ripple periods are so small, it is only with much effort that photomicrographs of the structure can be obtained and then only for permanent structures. Young [Young J. F. *et al.* (1984) pp. 2001-2015] therefore noted some other techniques such as time-resolved optical diffraction, electron-microscope (SEM) and optical-microscope studies of the surface topographies. It must be noted that SEM can only be used for permanent structures, but the diffraction techniques for both permanent and transient structures.

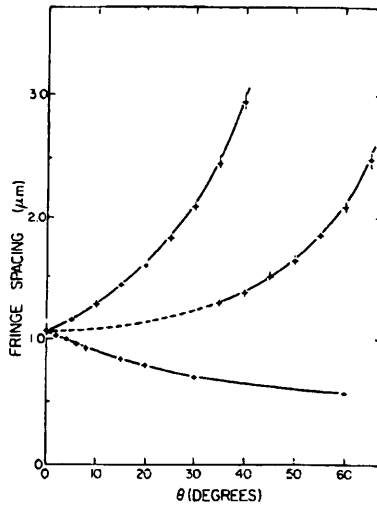


Fig. 1.6 Measured spacings of the dominant fringe patterns produced on Ge with p-polarized radiation as a function of θ , the angle of incidence. The curves are plots of the functions $1.06/(1-\sin\theta)$ (top), $1.06/\cos\theta$ (middle), and $1.06/(1+\sin\theta)$ (bottom). [Young J. F. *et al.* (1983) pp. 1158]

Siegman and Young found that it was best to study the back-diffraction properties of the ripples by an arrangement such as in Fig. 1.7. The technique requires a normally incident monitoring laser beam with a wavelength shorter than the writing beam and a screen to monitor the back-diffraction pattern. The grating vector components of the ripples then map directly into geometric patterns on the observation screen.

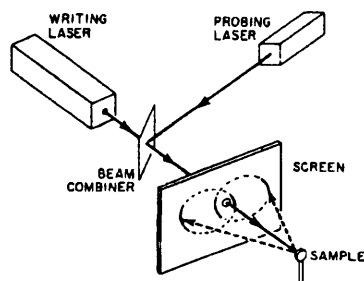


Fig. 1.7 Back-diffraction technique for observing periodic surface grating structures. [Siegman A. E. and Fauchet P. M. (1986) pp. 1387]

Young [Young J. F. *et al.* (1983) pp. 1155-1172] did some back-diffraction experiments and their results for p- and s-polarization for different diffraction angles are summarised in

Fig. 1.8. Each pattern consists of two overlapping circles of radius $2\pi/\lambda$, with λ the wavelength of the incident light. The extent to which the circles are filled out depends on the prominence of the ripple pattern, i.e. the more prominent the ripples, the more the diffraction efficiency.

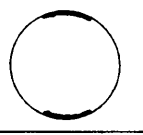
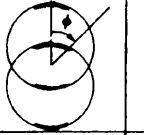
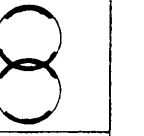

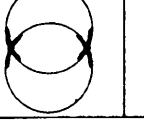
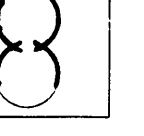
θ Pol	$\theta = 0^\circ$	$\theta \leq 45^\circ$	$\theta \geq 45^\circ$
P ↑			
S →			

Fig. 1.8 A table summarising the general trend of the Fourier transform of the damage structure observed on Ge at $1.06 \mu\text{m}$, as a function of θ and polarization. [Young J. F. *et al.* (1983) pp.1161]

Low modulation structures have a low diffraction efficiency and are therefore hard to observe. It is also not always practical or desirable to make use of SEM techniques to study LIPS-structures, since the SEM-techniques require the formation of permanent structures on the semiconductor surfaces.

Brink [Brink D. J. and Smit J. E. (1993) pp. 189-193] used an alternative technique based on the fact that the presence of LIPS-structures will change the state of polarization of a probe beam reflecting off such a surface. As ellipsometry, which is based on this principle, is known to be capable of resolving surface layers as thin as a few angstroms, it poses a viable alternative to observe transient LIPS-structures. This work is an extension of this method to see if one can extract more information regarding the height of the structure, the temperature distribution across the structure and to determine the effect of the light induced carrier density on the change in the refractive index of the material.

CHAPTER 2

THEORY OF LIGHT SCATTERING FROM STRUCTURED SURFACES

In scattering problems, it is often useful to know the scattered field at a point far from the scattering surface. In this chapter the formulation of Silver [Silver S. (1949) Chapter 3] will be used to derive an expression for the scattered electric field at a point in the far field in terms of the electric and magnetic fields on the scattering surface. It has been shown [Fung A. K. (1966) pp. 395-396] that this formulation is superior to the more well known Kirchhoff method when polarization effects are important and when the surface profile or roughness is prominent. In the final section of this chapter the Silver formulation is generalised to include the possibility of an arbitrary scattering direction and a finite complex refractive index for the scattering surface.

1. Radiation from current distributions

1.1 Field equations

The field equations are Maxwell's equations, relating the magnetic field vectors \vec{B} , \vec{H} and the electric field vectors \vec{E} , \vec{D} to each other and to the field sources, namely the electric charges and currents. In this section definitions of the quantities used will be given.

The sources are specified in terms of density functions. In a volume V , the excess positive charge is

$$Q = \iiint_V \rho dV, \quad (1)$$

with ρ the charge density per unit volume. The mks unit of ρ is Coulomb per cubic meter (C/m^3).

The current through the surface S enclosing the volume V is

$$I = -\oiint_S \vec{J} \cdot \hat{n} dS \quad (2)$$

where \hat{n} is the unit vector normal to S in the outward direction, and \vec{J} is the current density. The mks unit of \vec{J} is Ampere per square meter (A/m^2). A minus sign is used because I is considered positive when the direction of the nett flow of charge is into V . Making use of the divergence theorem (See App. A), the last integral then becomes

$$I = -\iiint_V \nabla \cdot \vec{J} dV. \quad (3)$$

Also:

$$I = \frac{dQ}{dt} = \frac{d}{dt} \iiint_V \rho dV. \quad (4a)$$

The time derivative operates only on ρ since V is fixed. Therefore:

$$I = \iiint_V \frac{\partial \rho}{\partial t} dV. \quad (4b)$$

Equating equations (3) and (4b):

$$\iiint_V \left(\frac{\partial \rho}{\partial t} + \nabla \cdot \vec{J} \right) dV = 0. \quad (5)$$

Since V is an arbitrary volume, the integrand of eq. (5) must vanish. The equation of continuity is therefore:

$$\frac{\partial \rho}{\partial t} + \nabla \cdot \vec{J} = 0. \quad (6)$$

In the case of finite charges and currents which are limited to surfaces of discontinuity, the excess positive charge on a surface S is

$$Q = \iint_S \xi dS, \quad (7)$$

with ξ the charge density per unit area.

Let C be a curve on the surface S and \hat{n}_1 a normal unit vector in the tangent plane. The total current across C is then given by

$$I = \int_C \vec{L} \cdot \hat{n}_1 ds, \quad (8)$$

with \vec{L} the surface current density. Analogous to the current density \vec{J} and the charge density ρ , the surface current density \vec{L} and the charge density ξ over the boundary of an infinitely conducting medium must satisfy an equation of continuity. Therefore,

$$\nabla_s \cdot \vec{L} + \frac{\partial \xi}{\partial t} = 0, \quad (9)$$

with the “surface divergence” of \vec{L} , $\nabla_s \cdot \vec{L}$, defined by

$$\nabla_s \cdot \vec{L} = \lim_{A \rightarrow 0} \frac{1}{A} \oint_C \vec{L} \cdot \hat{n}_1 ds, \quad (10)$$

C circumscribing the area A .

The forces exerted on the charges and currents are measured by the electric field vector \vec{E} and the magnetic induction \vec{B} respectively. The electric displacement \vec{D} and the magnetic intensity \vec{H} are related to \vec{E} and \vec{B} through

$$\vec{D} = \epsilon \vec{E}, \quad (11a)$$

$$\vec{B} = \mu \vec{H} \quad (11b)$$

where ϵ is the electric permittivity and μ the magnetic permeability. Both are considered to be constants. In vacuum their values are

$$\epsilon_0 = 8.85 \times 10^{-12} \text{ farad/meter}, \quad (12a)$$

$$\mu = 4\pi \times 10^{-7} \text{ henry/meter}. \quad (12b)$$

The field equations can then be written as:

$$\nabla \times \vec{E} + \frac{\partial \vec{B}}{\partial t} = 0, \quad (13a)$$

$$\nabla \times \vec{H} = \vec{J} + \frac{\partial \vec{D}}{\partial t}, \quad (13b)$$

$$\nabla \cdot \vec{B} = 0, \quad (13c)$$

$$\nabla \cdot \vec{D} = \rho \quad (13d)$$

with continuity equation

$$\nabla \cdot \vec{J} + \frac{\partial \rho}{\partial t} = 0. \quad (13e)$$

1.2 Linearity, superposition and boundary conditions

The superposition principle is widely used to describe interference and diffraction phenomena [Azzam R. M. A. and Bashara N. M (1972) pp. 4721-4729; Botten L. C. *et al.* (1980); Guenther R. (1990); Hecht (1987)].

There are two types of current that contribute to the density \vec{J} , namely convection and conduction currents. For this discussion only conductive currents are taken into account. Therefore, the density \vec{J} is proportional to the electric field vector \vec{E} :

$$\vec{J} = \sigma \vec{E}. \quad (14)$$

The constant σ is the medium's conductivity and it may depend on optical frequency. When a medium is conductive, it cannot support a free volume charge density ρ . Therefore, if a finite conductivity is assumed, ρ may be taken as zero.

When the parameters ϵ and μ are independent of the field strength, the relations between Maxwell's equations and the constitutive relation, i.e. eqs. (11a), (11b) and (14), are linear. The superposition principle applies. The principle states that if two sets of field vectors, $\vec{E}_1, \vec{B}_1, \vec{D}_1, \vec{H}_1, \vec{E}_2, \vec{B}_2, \vec{D}_2, \vec{H}_2$ and densities $\rho_1, \vec{J}_1, \rho_2, \vec{J}_2$ satisfy the field equations, their sums $\vec{E}_1 + \vec{E}_2, \dots, \vec{H}_1 + \vec{H}_2, \rho_1 + \rho_2, \vec{J}_1 + \vec{J}_2$ also satisfy the field equations and describes an electromagnetic field.

Consider the boundary surface between two media with constitutive parameters $\epsilon_1, \mu_1, \sigma_1$ and $\epsilon_2, \mu_2, \sigma_2$ respectively. The positive unit vector \hat{n} is considered normal to the boundary surface and is directed from medium 1 into medium 2. Let \vec{E}_1, \vec{E}_2 and \vec{H}_1, \vec{H}_2 be the field vectors on either side of the boundary. The boundary conditions are the following:

1. From Maxwell's equation (13a), the tangential component of \vec{E} is continuous across the boundary:

$$\hat{n} \times (\vec{E}_2 - \vec{E}_1) = 0. \quad (15)$$

If the medium is conductive, the field penetrates into the medium a distance inversely proportional to the square root of the conductivity. \vec{E}_1 must be zero when σ tends to infinity, and the above condition reduces to

$$\hat{n} \times \vec{E}_2 = 0. \quad (16)$$

2. From equation (13c), the normal component of \vec{B} is continuous across the boundary:

$$\hat{n} \cdot (\vec{B}_2 - \vec{B}_1) = \hat{n} \cdot (\mu_2 \vec{H}_2 - \mu_1 \vec{H}_1) = 0. \quad (17)$$

3. From equation (13d) it is clear that the normal component of \vec{D} is continuous across the boundary if no surface charge layer is present. If such a layer exists, the condition becomes

$$\hat{n} \cdot (\vec{D}_2 - \vec{D}_1) = \xi, \quad (18)$$

ξ being the charge density per unit area. Such a charge layer only occurs when one of the media has a finite conductivity.

4. From equation (13b), the tangential component of \vec{H} is continuous if there are no surface currents. If there is a surface current sheet on the boundary, the tangential component is discontinuous:

$$\hat{n} \times (\vec{H}_2 - \vec{H}_1) = \vec{L}, \quad (19)$$

\vec{L} being the surface current density. Such currents exist when one of the media is conducting.

1.3 General solution to the field equations for a time-periodic field

It is useful to consider the fields and sources as having a harmonic time dependence $e^{i\omega t}$. The real and imaginary parts of these complex solutions are in themselves real solutions of the fields. Maxwell's equations then become

$$\nabla \times \vec{E} + i\omega \vec{B} = 0, \quad (20a)$$

$$\nabla \times \vec{H} = \vec{J} + i\omega \vec{D} = (\sigma + i\omega \epsilon) \vec{E}, \quad (20b)$$

$$\nabla \cdot \vec{D} = \rho, \quad (20c)$$

$$\nabla \cdot \vec{B} = 0, \quad (20d)$$

$$\nabla \cdot \vec{J} + i\omega\rho = 0. \quad (20e)$$

Various solutions exist for the field equations. Plane and cylindrical waves form such solutions when it is assumed that their sources lie outside the domain of validity of the solution, else the energy densities will tend to infinity. The following discussion will focus on determining what fields will arise from a prescribed set of field sources inside a homogeneous medium.

Consider equation (20a-e) and the “vector” Helmholtz equations

$$\nabla \times \nabla \times \vec{E} - k^2 \vec{E} = -i\omega\mu\vec{J}, \quad (21a)$$

$$\nabla \times \nabla \times \vec{H} - k^2 \vec{H} = \nabla \times \vec{J} \quad (21b)$$

where $k^2 = \omega^2\epsilon\mu$. (These equations are derived in App. A.)

Equations (21a) and (21b) can be integrated according to Green’s Theorem (See App. A):

Suppose a volume V exists, such that \vec{E} and \vec{H} meet the conditions of continuity required of the Green’s vector \vec{F} . The aim is to express the field at an arbitrary point P in the volume, in terms of the field sources within this volume and the field values over the volume’s boundaries.

Define a vector function of position

$$\vec{G} = \frac{e^{-ikr}}{r} \vec{a} = \psi \vec{a}, \quad (22)$$

with \vec{a} an arbitrary constant vector and r the distance from P to any other point inside the volume. \vec{G} therefore satisfies the continuity requirement of the Theorem, except at P , where it has a singularity. This problem is avoided by surrounding P by a sphere Σ of

radius r_0 and considering the portion V' of V surrounded by surfaces S_1, \dots, S_n and Σ . \vec{G} and $\vec{F} = \vec{E}$ now fulfill all the requirements of Green's Theorem. Then

$$\begin{aligned} & \iiint_{V'} (\psi \vec{a} \cdot \nabla \times \nabla \times \vec{E} - \vec{E} \cdot \nabla \times \nabla \times \psi \vec{a}) dv \\ &= - \iint_{S_1 + \dots + S_n + \Sigma} (\vec{E} \times \nabla \times \psi \vec{a} - \psi \vec{a} \times \nabla \times \vec{E}) \cdot \hat{n} dS. \end{aligned} \quad (23)$$

In order to transform the volume integral to a surface integral, make use of the facts that \vec{a} is a constant vector and that ψ satisfies the scalar Helmholtz equation, and then introduce $\psi \vec{a}$ into the vector identity

$$\nabla \times \nabla \times \vec{P} = \nabla(\nabla \cdot \vec{P}) - \nabla^2 \vec{P}, \quad (24)$$

to give

$$\nabla \times \nabla \times \psi \vec{a} = \nabla(\vec{a} \cdot \nabla \psi) + k^2 \psi \vec{a}. \quad (25)$$

By using equations (25) and (21a), the integrand of the volume integral of eq. (23) reduces to

$$\psi \vec{a} \cdot \nabla \times \nabla \times \vec{E} - \vec{E} \cdot \nabla \times \nabla \times \psi \vec{a} = \vec{a} \cdot (-i\omega \mu \vec{J} \psi) - \nabla \cdot [\vec{E}(\vec{a} \cdot \nabla \psi)] - \frac{\rho}{\epsilon} \vec{a} \cdot \nabla \psi \quad (26)$$

where use has been made of the vector identities A.4 and A.5 in App. A. Equation (23) then becomes

$$\begin{aligned} & \vec{a} \cdot \iiint_{V'} \left(i\omega \mu \vec{J} \psi - \frac{\rho}{\epsilon} \nabla \psi \right) dv + \iiint_{V'} \nabla \cdot [\vec{E}(\vec{a} \cdot \nabla \psi)] dv \\ &= \iint_{S_1 + \dots + S_n + \Sigma} [(\vec{E} \times \nabla \times \psi \vec{a}) \cdot \hat{n} - (\psi \vec{a} \times \nabla \times \vec{E}) \cdot \hat{n}] dS. \end{aligned} \quad (27)$$

Transform the second integral on the lefthand side of eq. (27) to a surface integral:

$$\iiint_{V'} \nabla \cdot [\vec{E}(\vec{a} \cdot \nabla \psi)] dv = -\vec{a} \cdot \iint_{S_1 + \dots + S_n + \Sigma} (\hat{n} \cdot \vec{E}) \nabla \psi dS. \quad (28)$$

Transform the surface integral in eq. (27) in the following way:

$$[\vec{E} \times (\nabla \times \psi \vec{a})] \cdot \hat{n} = [(\hat{n} \times \vec{E}) \times \nabla \psi] \cdot \vec{a}, \quad (29)$$

$$\psi(\vec{a} \times \nabla \times \vec{E}) \cdot \hat{n} = i\omega\mu\psi\vec{a} \cdot (\hat{n} \cdot \vec{H}). \quad (30)$$

Substitute these results back into eq. (27). Then

$$\begin{aligned} & \vec{a} \cdot \iiint_{V'} \left(i\omega\mu\psi\vec{J} - \frac{\rho}{\epsilon} \nabla\psi \right) dv \\ &= \vec{a} \cdot \iint_{S_1+\dots+S_n+\Sigma} \left[-i\omega\mu\psi(\hat{n} \times \vec{H}) + (\hat{n} \times \vec{E}) \times \nabla\psi + (\hat{n} \cdot \vec{E})\nabla\psi \right] dS. \end{aligned} \quad (31)$$

Equation (31) must hold for every vector \vec{a} . The integrands must therefore be equal.

That is

$$\begin{aligned} & \iint_{\Sigma} \left[-i\omega\mu\psi(\hat{n} \times \vec{H}) + (\hat{n} \times \vec{E}) \times \nabla\psi + (\hat{n} \cdot \vec{E})\nabla\psi \right] dS \\ &= \iiint_{V'} \left(i\omega\mu\psi\vec{J} - \frac{\rho}{\epsilon} \nabla\psi \right) dv \\ & - \iint_{S_1+\dots+S_n} \left[-i\omega\mu\psi(\hat{n} \times \vec{H}) + (\hat{n} \times \vec{E}) \times \nabla\psi + (\hat{n} \cdot \vec{E})\nabla\psi \right] dS. \end{aligned} \quad (32)$$

This gives the relation between the field at P , and the volume integral over the field sources and also surface integrals involving the field itself.

Now consider the integral over Σ . On the sphere's surface

$$(\nabla\psi) = \left[\frac{d}{dr} \left(\frac{e^{-ikr}}{r} \right) \right]_{r=r_0} \hat{n} = - \left(ik + \frac{1}{r_0} \right) \frac{e^{-ikr_0}}{r_0} \hat{n}. \quad (33)$$

The normal vector \hat{n} is directed radially outward from P . Substitute equation (33) into eq.

(32). Then

$$\iint_{\Sigma} [\] dS = -i4\pi r_0 e^{-ikr_0} \left(\omega\mu \langle \hat{n} \times \vec{H} \rangle + k \langle \vec{E} \rangle \right) - 4\pi e^{-ikr_0} \langle \vec{E} \rangle, \quad (34)$$

where the mean value of the function over the surface is denoted by $\langle \dots \rangle$. Let the sphere Σ shrink to zero. The term containing r_0 disappears because the field vectors are considered finite near P by hypothesis. Also, $\langle \vec{E} \rangle$ approaches \vec{E}_P , with \vec{E}_P the value of $\langle \vec{E} \rangle$ at P .

Then

$$\lim_{r_0 \rightarrow 0} \iint_{\Sigma} [\] dS = -4\pi \vec{E}_P . \quad (35)$$

In this limit V' includes the entire region V . Equation (32) then becomes

$$\begin{aligned} \vec{E}_P = & -\frac{1}{4\pi} \iiint_{V'} \left(i\omega \mu \psi \vec{J} - \frac{\rho}{\epsilon} \nabla \psi \right) dV \\ & + \frac{1}{4\pi} \iint_{S_1 + \dots + S_n} \left[-i\omega \mu \psi (\hat{n} \times \vec{H}) + (\hat{n} \times \vec{E}) \times \nabla \psi + (\hat{n} \cdot \vec{E}) \nabla \psi \right] dS. \end{aligned} \quad (36)$$

\vec{H}_P satisfies an equation analogous to eq. (36), but since only the equation for \vec{E}_P is of interest, \vec{H}_P will not be discussed.

The surface integrals represent the contribution of sources outside V to the field inside V ; for example, the surface integral over S_i - where S_i encloses an exterior volume V_i - represents the effect of sources lying inside V_i .

It is interesting to note that in eq. (36), the terms $(\hat{n} \times \vec{H})$ and $(\hat{n} \cdot \vec{E})$ enter the surface integral in the same way that \vec{J} and ρ enter the volume integral. This shows that the effects of the sources inside an exterior volume V_i , bounded by S_i , are represented as arising from surface-charge and surface-current distributions in the boundary S_i , with surface densities

$$\vec{L} = (\hat{n} \times \vec{H}), \quad (37a)$$

$$\xi = \epsilon (\hat{n} \cdot \vec{E}), \quad (37b)$$

where \vec{E} and \vec{H} are the fields over the surface S_i .

1.4 Solution for fields arising from sources in an unbounded region

Consider the case where V represents an unbounded volume and where the sources are confined to a finite region of space. This means that there is only one boundary surface S_n .

Let S_n be a sphere of radius R around the point P . Choose a unit vector \hat{R}_1 directed outward from this sphere along its radius, so that $\hat{R}_1 = \hat{n}$. Substitute this and the explicit

form of ψ , namely $\psi = \frac{e^{-ikR}}{R}$ into eq. (36). Then

$$\vec{E}_P = \frac{1}{4\pi} \iint_{S(R)} \left\{ i\omega\mu \left[\hat{R}_1 \times \vec{H} \right] + \left(\frac{\epsilon}{\mu} \right)^{1/2} \vec{E} \right\} + \frac{\vec{E}}{R} \left\} \frac{e^{-ikR}}{R} dS. \quad (38)$$

Let R approach infinity. The sphere's surface will then increase as R^2 . As $R \rightarrow \infty$, the surface integral will disappear if the fields satisfy the following conditions:

$$\lim_{R \rightarrow \infty} R\vec{E} \text{ is finite,} \quad (39a)$$

$$\lim_{R \rightarrow \infty} R \left[\hat{R}_1 \times \vec{H} \right] + \left(\frac{\epsilon}{\mu} \right)^{1/2} \vec{E} = 0. \quad (39b)$$

Equation (39a) requires that the magnitudes of the field vectors must at least decrease as R^{-1} at large distances from the source. The "radiation condition" eq. (39b) states that all radiation across the sphere's boundary consists of waves diverging to infinity.

Therefore, if all the sources are inside a finite region of space and if the fields arising from those sources satisfy eqs. (39) at infinity, then

$$\vec{E}_P = -\frac{1}{4\pi} \iiint_V \left[i\omega\mu \vec{J} \frac{e^{-ikr}}{r} - \frac{\rho}{\epsilon} \nabla \left(\frac{e^{-ikr}}{r} \right) \right] dv. \quad (40)$$

This field is now expressed only in terms of the sources. It can also be expressed in terms of the current distributions and the equation of continuity (eq. (20e)). Taking $1/\omega\epsilon$ to the outside of the integral and letting $k^2 = \omega^2\epsilon\mu$, eq. (40) then becomes

$$\vec{E}_P = -\frac{1}{4\pi\omega\epsilon} \iiint_V [(\vec{J} \cdot \nabla)\nabla + k^2\vec{J}] \frac{e^{-ikr}}{r} dv. \quad (41)$$

Equation (41) is then the required solution.

2. Diffraction and reflection from a rough surface with a regular pattern

The introduction of an obstacle into the path of a wave gives rise to diffraction and reflection phenomena.

In this section the discussion of these phenomena will be restricted to an obstacle of infinite conductivity. The problem is stated as follows: A given system of sources produces an electromagnetic field \vec{E}^i, \vec{H}^i . The fields get diffracted from the infinitely conducting surface, resulting then in \vec{E}^d, \vec{H}^d . The requirement is to find the electric field, \vec{E} , at a point P from the surface.

In section 1.4 it was shown that the field at a point in space lying outside the surface that contains all the sources of the field, can be expressed in terms of the integrals of the field vectors over that surface. If Σ is a surface that surrounds the reflector completely, the scattered electric field at an external point P in space is given by eq. (36):

$$\vec{E}_P = \frac{1}{4\pi} \iint_{\Sigma} [-i\omega\mu\psi(\hat{n} \times \vec{H}) + (\hat{n} \times \vec{E}) \times \nabla\psi + (\hat{n} \cdot \vec{E})\nabla\psi] dS \quad (42)$$

where $\psi = \frac{e^{-ikr}}{r}$. The primary system of sources produces an electromagnetic field \vec{E}^i, \vec{H}^i , while the diffracted fields are given by \vec{E}^d, \vec{H}^d . The total field is then given by the superposition principle:

$$\vec{E} = \vec{E}^i + \vec{E}^d \text{ and } \vec{H} = \vec{H}^i + \vec{H}^d. \quad (43)$$

The normal unit vector \hat{n} is directed outward from the local surface S that surrounds a volume V occupied by the portion of the surface that is illuminated. Inside V the total field \vec{E}, \vec{H} is zero, since it is assumed that the surface is infinitely conducting. Therefore $\vec{E}^i = -\vec{E}^d$ and $\vec{H}^i = -\vec{H}^d$ everywhere inside V .

2.1 The Aperture-field method

2.1.1 Introduction

The diffracting surface acts as a reflector, which has the property that the entire family of rays that is reflected from the illuminated surface S , lie in one hemisphere of space, as shown in Fig. 2.1. It is also possible to draw a finite curve Γ_s near the reflector that circumscribes the entire family of reflected rays. The shadow boundary Γ on the surface then acts as an aperture through which the reflected rays exit, as if they were coming from a distribution of sources behind the obstacle. The diffracted field $\vec{E}(P)$ will concentrate largely in the hemisphere of space that contains the reflected rays. Σ will therefore be regarded as consisting of an infinite plane containing a curve such as Γ_s surrounding the area S .

The diffracted field must satisfy the radiation conditions (eqs. (39a) and (39b)) at infinity and therefore the hemispherical cap will make no contribution to the field integral in eq. (42). The terms in the integrand of eq. (42) can be set into correspondence with surface

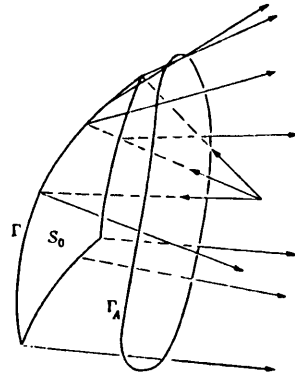


Fig. 2.1 The diffracting surface of the aperture-field method. [Silver S. (1949) pp. 159]

distributions of electric and magnetic charges and currents. This means that the electric and magnetic fields over the surface must satisfy the continuity equation for the integrands to satisfy Maxwell's equations. Since the distribution of Σ is discontinuous, with a non-zero field over the area circumscribed by Γ_S and a zero field over the area of Σ outside Γ_S , it is necessary to introduce line distributions of electric and magnetic charges along the boundary curve Γ_S .

2.1.2 Reflection of a plane wave by an infinite perfectly conducting plane surface

Two assumptions regarding the diffracting surface can be made, namely:

1. The surface sits in the far field so that the wavefronts reaching the surface can be considered to be plane waves.
2. The fields are considered to be time periodic.
3. The surface acts as an infinite perfectly conducting plane.

The initial field is

$$\vec{E}^i = \vec{E}_0 e^{i(\omega t - k\hat{k}^i \cdot \vec{r})} \tag{44a}$$

and the reflected field is

$$\vec{E}^d = \vec{E}_1 e^{i(\omega t - k\hat{k}^d \cdot \vec{r})} \quad (44b)$$

where $\hat{k}^{i,d}$ are the unit vectors in the incident and reflected directions respectively (see Fig. 2.2). It is important to note that $\hat{k}^{i,d}$ are chosen to lie in the XZ-plane.

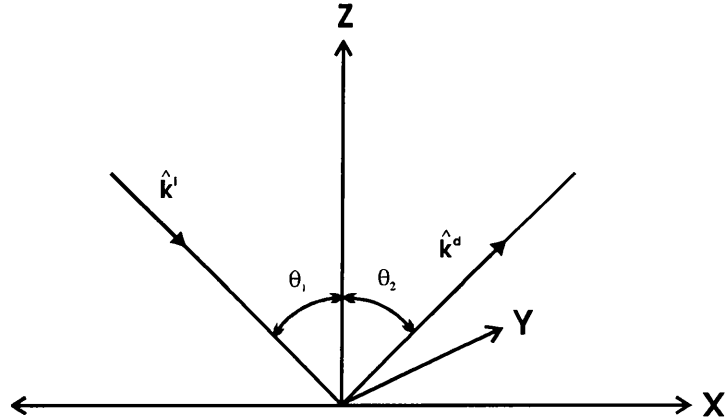


Fig. 2.2 Representation of unit vectors \hat{k}^i and \hat{k}^d .

According to Silver [Silver S. (1949) pp. 113], the plane wave in the \hat{k}^d direction is the mirror image of the wave travelling in the \hat{k}^i direction. Thus:

1. The magnitudes of \vec{E}^i and \vec{E}^d are equal,

$$|\vec{E}^i| = |\vec{E}^d| \quad (45a)$$

2. their components parallel to the XY-plane are equal in magnitude and direction,

$$\hat{n} \times \vec{E}^d = -\hat{n} \times \vec{E}^i, \quad (45b)$$

where \hat{n} is the unit vector in the positive Z-axis direction, and

3. their components normal to the XY-plane are equal in magnitude but opposite in direction

$$\hat{n} \cdot \vec{E}^d = -\hat{n} \cdot (-\vec{E}^i) = \hat{n} \cdot \vec{E}^i. \quad (45c)$$

It is thus clear that \hat{k}^i , \hat{n} and \hat{k}^d all lie in the XZ-plane and that

$$\hat{k}^i \cdot \hat{n} = -\hat{k}^d \cdot \hat{n}. \quad (46)$$

The relations between these vectors can also be expressed as

$$\hat{k}^d = \hat{k}^i - 2(\hat{n} \cdot \hat{k}^i)\hat{n}, \quad (47a)$$

$$\hat{k}^i = \hat{k}^d - 2(\hat{n} \cdot \hat{k}^d)\hat{n}. \quad (47b)$$

It is useful to define a few relations between \vec{E} , \vec{H} and \vec{L} which will be used in further discussions to follow.

The magnetic field vectors for the incident wave, \vec{H}^i and for the diffracted wave, \vec{H}^d can be derived directly from the Maxwell equations:

$$\vec{H}^i = \frac{1}{\eta}(\hat{k}^i \times \vec{E}^i), \quad (48a)$$

$$\vec{H}^d = \frac{1}{\eta}(\hat{k}^d \times \vec{E}^d) \quad (48b)$$

where $\eta = \sqrt{\mu_0/\epsilon_0}$, with μ_0 and ϵ_0 the permeability and permittivity of vacuum (or approximately of air).

Since the conductivity of the reflector is assumed infinite, the total \vec{E} and \vec{H} fields are zero everywhere inside the volume V and there is a charge and current distribution over the surface of the reflector:

$$\xi = \epsilon_0(\hat{n} \cdot \vec{E}), \quad (49a)$$

$$L = \hat{n} \times \vec{H}. \quad (49b)$$

Furthermore it can be shown that

$$\hat{n} \times \vec{H}^i = \hat{n} \times \vec{H}^d. \quad (50)$$

Equation (49b) then becomes

$$\vec{L} = 2(\hat{n} \times \vec{H}^i) = 2 \frac{1}{\eta} (\hat{n} \times (\hat{k}^i \times \vec{E}^i)) \quad (51a)$$

or alternatively

$$\vec{L} = 2(\hat{n} \times \vec{H}^d) = 2 \frac{1}{\eta} (\hat{n} \times (\hat{k}^d \times \vec{E}^d)). \quad (51b)$$

2.1.3 The Current-distribution method

This method gives a good approximation for the diffracted field by attempting to approximate the current distribution over the surface.

Let $\hat{\tau}$ be a unit vector along the boundary curve Γ_S and \hat{n}_1 a unit vector in the tangent plane normal to $\hat{\tau}$ (see Fig. 2.3). Let σ_e and σ_m denote the linear electric and magnetic density along Γ_S respectively and consider a small area ds by dl .

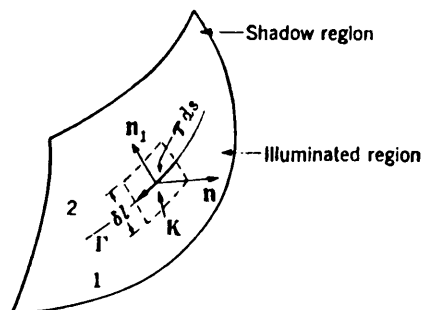


Fig. 2.3 Diagram showing the calculation of the electric charge on the shadow boundary curve. [Silver. S. (1949) pp. 147]

The nett current flow from the area is equal to the rate of decrease of the charge enclosed:

$$-\hat{n}_1 \cdot \vec{L} ds = -\frac{\partial \sigma_e}{\partial t} ds. \quad (52)$$

Substituting from eq. (49b) it follows that

$$\begin{aligned} \frac{\partial \sigma_e}{\partial t} &= \hat{n}_1 \cdot \vec{L} = \hat{n}_1 \cdot (\hat{n} \times \vec{H}) \\ &= \vec{H} \cdot (\hat{n}_1 \times \hat{n}) \\ &= -\hat{\tau} \cdot \vec{H}. \end{aligned} \quad (53)$$

Since the fields are time periodic, $\partial \sigma_{e/m} / \partial t = i\omega \sigma_{e/m}$, whence

$$\sigma_e = -\frac{1}{i\omega} \hat{\tau} \cdot \vec{H}. \quad (54)$$

Equation (42) then becomes

$$\begin{aligned} \vec{E}_P &= -\frac{1}{4\pi i\omega \epsilon_0} \oiint_{\Gamma_s} \nabla \Psi(\hat{\tau} \cdot \vec{H}) ds \\ &= \frac{1}{4\pi} \iint_S \left[-i\omega \mu_0 \Psi(\hat{n} \times \vec{H}) + (\hat{n} \times \vec{E}) \times \nabla \Psi + (\hat{n} \cdot \vec{E}) \nabla \Psi \right] dS \end{aligned} \quad (55)$$

where S is the area enclosed by Γ_s .

Since the gradient operations in the integrand of eq. (55) take the point P as origin (see Sec. 1.4), a rectangular co-ordinate system with P as origin can be constructed. Let the co-ordinates of a point on S be x_α ($x_1 = X$, $x_2 = Y$, $x_3 = Z$) and \hat{i}_α be unit vectors along the x_α -axis. Then

$$\frac{1}{4\pi i\omega \epsilon_0} \oiint_{\Gamma_s} \nabla \Psi(\hat{\tau} \cdot \vec{H}) ds = \frac{1}{4\pi i\omega \epsilon_0} \sum_{\alpha=1}^3 \hat{i}_\alpha \oiint_{\Gamma_s} \hat{\tau} \cdot \left(\vec{H} \frac{\partial \Psi}{\partial x_\alpha} \right) ds. \quad (56)$$

According to Stokes

$$\iint_{\Gamma_s} \hat{\tau} \cdot \left(\vec{H} \frac{\partial \Psi}{\partial x_\alpha} \right) ds = \iint_s \left(\nabla \times \vec{H} \frac{\partial \Psi}{\partial x_\alpha} \right) \cdot \hat{n} dS \quad (57)$$

but

$$\begin{aligned} \nabla \times \left(\vec{H} \frac{\partial \Psi}{\partial x_\alpha} \right) &= \nabla \frac{\partial \Psi}{\partial x_\alpha} \times \vec{H} + \frac{\partial \Psi}{\partial x_\alpha} \nabla \times \vec{H}, \\ \left(\nabla \frac{\partial \Psi}{\partial x_\alpha} \times \vec{H} \right) \cdot \hat{n} &= -(\hat{n} \times \vec{H}) \cdot \nabla \frac{\partial \Psi}{\partial x_\alpha}, \\ \left(\frac{\partial \Psi}{\partial x_\alpha} \nabla \times \vec{H} \right) \cdot \hat{n} &= i\omega \epsilon \frac{\partial \Psi}{\partial x_\alpha} (\hat{n} \cdot \vec{E}). \end{aligned} \quad (58)$$

Substituting eqs. (57) and (58) into (56), gives

$$\frac{1}{4\pi i\omega \epsilon_0} \iint_{\Gamma_s} \nabla \Psi (\hat{\tau} \cdot \vec{H}) ds = \frac{1}{4\pi} \sum_{\alpha=1}^3 \hat{i}_\alpha \iint_s \left[\hat{n} \cdot \vec{E} \frac{\partial \Psi}{\partial x_\alpha} - \frac{1}{i\omega \epsilon_0} (\hat{n} \times \vec{H}) \cdot \nabla \frac{\partial \Psi}{\partial x_\alpha} \right] dS \quad (59)$$

or

$$\frac{1}{4\pi i\omega \epsilon_0} \iint_{\Gamma_s} \nabla \Psi (\hat{\tau} \cdot \vec{H}) ds = \frac{1}{4\pi} \iint_s \left[(\hat{n} \cdot \vec{E}) \nabla \Psi - \frac{1}{i\omega \epsilon_0} (\hat{n} \times \vec{H}) \cdot \nabla \nabla \Psi \right] dS. \quad (60)$$

Substituting into eq. (55) gives

$$\vec{E}(P) = \frac{1}{4\pi\omega \epsilon_0} \iint_s \left[(\hat{n} \times \vec{H}) \cdot \nabla (\nabla \Psi) + k^2 (\hat{n} \times \vec{H}) \Psi + i\omega \epsilon_0 (\hat{n} \times \vec{E} \times \nabla \Psi) \right] dS. \quad (61)$$

2.1.4 The Fraunhofer region

The solution, equation (61), is based on the assumption that the sources all lie within a finite region of space. Choose a co-ordinate system with the origin near the region of sources and let \vec{p} be the vector from the origin to a source element at (x, y, z) (see Fig. 2.4). Let \hat{R}_1 be a unit vector and $R\hat{R}_1$ the vector from the origin to the observation point

P . Similarly, \hat{r}_1 is a unit vector and $r\hat{r}_1$ the vector from the source element to P . In the Fraunhofer region (far field) $r \gg R$.

In the integrand of eq. (61), the operator ∇ only acts on (x, y, z) - the source element's coordinates and P is treated as a fixed point. As an example, consider

$$\nabla \psi = \frac{d}{dr} \left(\frac{e^{-ikr}}{r} \right) = \left(ik + \frac{1}{r} \right) \frac{e^{-ikr}}{r} \hat{r}_1 \approx ik \frac{e^{-ikr}}{r} \hat{r}_1 \quad (62)$$

and

$$\begin{aligned} & ((\hat{n} \times \vec{H}) \cdot \nabla) \nabla \left(\frac{e^{-ikr}}{r} \right) \\ &= \left[-k^2 ((\hat{n} \times \vec{H}) \cdot \hat{r}_1) \hat{r}_1 + \frac{3}{r} \left(ik + \frac{1}{r} \right) ((\hat{n} \times \vec{H}) \cdot \hat{r}_1) \hat{r}_1 - \frac{(\hat{n} \times \vec{H})}{r} \left(ik + \frac{1}{r} \right) \right] \frac{e^{-ikr}}{r} \\ &\approx \left[-k^2 ((\hat{n} \times \vec{H}) \cdot \hat{r}_1) \hat{r}_1 \right] \frac{e^{-ikr}}{r}. \end{aligned} \quad (63)$$

Since r is large, terms in r^{-1} are dropped. Equation (61) then becomes

$$\vec{E}_P \approx \frac{-i}{4\pi\omega_0\epsilon_0} \iint_S \left[k^2 (\hat{n} \times \vec{H}) - k^2 ((\hat{n} \times \vec{H}) \cdot \hat{r}_1) \hat{r}_1 + \omega_0 \epsilon_0 k \hat{r}_1 \times (\hat{n} \times \vec{E}) \right] \frac{e^{-ikr}}{r} dS. \quad (64)$$

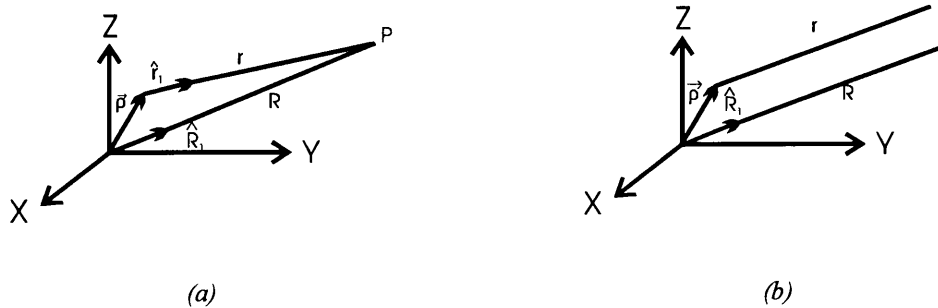


Fig. 2.4 (a) An arbitrary field point. (b) The simplifying relationships for a point in the far field. [Silver S. (1949) pp. 88]

A problem arising here is the fact that r and \hat{r}_1 vary with the variation in position of the different source elements. If the field point P is far away from the current distribution and origin, some simplifications can be made:

1. The angle between \hat{R}_1 and \hat{r}_1 can be neglected, thus giving $\hat{r}_1 = \hat{R}_1$.
2. The factor r^{-1} can be replaced by R^{-1} .
3. In the phase factor one has to be more careful. It is assumed that \hat{r}_1 and \hat{R}_1 are effectively parallel.

Therefore

$$r = R - \bar{\rho} \cdot \hat{R}_1. \quad (65)$$

Substituting all these approximation into eq. (64) gives

$$\vec{E}_P = \frac{-ik}{4\pi R} e^{-ikR} \hat{R}_1 \times \iint_S [(\hat{n} \times \vec{E}) - \eta \hat{R}_1 \times (\hat{n} \times \vec{H})] e^{ik\bar{\rho} \cdot \hat{R}_1} dS, \quad (66)$$

where $\eta = \sqrt{\frac{\mu_0}{\epsilon_0}}$.

It can be shown that eq. (66) satisfies the radiation condition (eq. (39b)). An analogous derivation can be done for \vec{H} , showing that \vec{E} and \vec{H} are related as in a plane wave, i.e. they are perpendicular to each other, and they lie in a plane normal to \hat{R}_1 .

In the aperture-field method, let $\rho = \vec{r}$ be the vector from the origin to the element dS of the aperture and $\hat{r}_1 = \hat{R}_1 = \hat{k}^d$. Then the analogue to eq. (65) is

$$r = R - \hat{k}^d \cdot \vec{r}. \quad (67)$$

Substituting eq. (67) into (66) gives:

$$\vec{E}(P) = -\frac{ike^{-ikR}}{4\pi R} \hat{k}^d \times \iint_S [(\hat{n} \times \vec{E}) - \eta \hat{k}^d \times (\hat{n} \times \vec{H})] e^{ik\hat{k}^d \cdot \vec{r}} dS, \quad (68)$$

which is the final result of the original Silver formulation.

2.1.5 Generalisation of the Silver formulation

The original Silver formulation is only valid for the case where the angle of incidence θ_i is equal to the angle of diffraction (or reflection), θ_d and for a perfectly conducting surface. It can be shown [Azzam R. M. A. and Bashara N. M. (1972) pp. 4721-4729] that the Silver formulation can be generalised to predict the amount of light scattered into an arbitrary direction from a surface with any finite (complex) refractive index by employing the so-called physical optics approximation. In this approach it is assumed that any tiny element of the scattering surface can be treated as part of an infinite plane. The magnitudes of the fields reflected from this plane are then obtained from the Fresnel coefficients:

$$E_p^d = E_p^i r_p \text{ and } E_s^d = E_s^i r_s,$$

with

$$r_s = \frac{\tilde{n}_1 \cos \theta_i - \tilde{n}_2 \cos \theta_t}{\tilde{n}_1 \cos \theta_i + \tilde{n}_2 \cos \theta_t}$$

$$r_p = \frac{\tilde{n}_1 \cos \theta_t - \tilde{n}_2 \cos \theta_i}{\tilde{n}_1 \cos \theta_t + \tilde{n}_2 \cos \theta_i},$$

with the \tilde{n}_i the refractive indices for air and the material of the medium,

$$\tilde{n}_1 \sin \theta_i = \tilde{n}_2 \sin \theta_t,$$

$$E_p^i = \vec{E}^i \cdot \hat{p}^i$$

$$E_s^i = \vec{E}^i \cdot \hat{s},$$

from which the net electric field directly above the plane can be obtained:

$$\vec{E} = \vec{E}^i + \vec{E}^d = \vec{E}^i + (E_s^d \hat{s} + E_p^d \hat{p}^d)$$

with \hat{p}^i , \hat{p}^d , \hat{s} unit vectors indicating the direction of the p- and s-polarized components of the incident and reflected fields. The net magnetic field is then given by:

$$\vec{H} = \vec{H}^i + \vec{H}^d = \frac{1}{\eta} (\hat{k}^i \times \vec{E}^i + \hat{k}^d \times \vec{E}^d).$$

In addition the generalised direction of the scattered beam with respect to the incident beam is incorporated by replacing \hat{k}^d in eq. (68) by $\hat{k}^d - \hat{k}^i$.

With these substitutions the Silver formulation becomes:

$$\vec{E}(P) = -A \hat{k}^d \times \iint_S \left[(\hat{n} \times \vec{E}) - \eta \hat{k}^d \times (\hat{n} \times \vec{H}) \right] e^{ik(\hat{k}^d - \hat{k}^i) \cdot \vec{r}} dS \quad (69)$$

where $\eta = \sqrt{\frac{\mu_0}{\epsilon_0}}$ with μ_0 and ϵ_0 the permeability and permittivity of air,

$k = \frac{2\pi}{\lambda}$ with λ the wavelength of the incident light,

$\hat{k}^{i,d}$ are unit vectors along the direction of the incident and scattered beams,

\vec{r} is the position vector of an arbitrary point on the diffracting surface, and

$A = \frac{ike^{ikR}}{4\pi R}$ with R the distance to the observation point P .

This generalised equation is used in chapters 3 and 4 to study optical diffraction from the wing of a moth and to interpret ellipsometric measurements of laser induced periodic surface structures on semiconductors.

CHAPTER 3

MATHEMATICAL MODELLING OF THE WING OF THE *TRICHOPLUSIA ORICHALCEA* MOTH

The golden patch on the wings of the *Trichoplusia orichalcea* moth, commonly known as the Golden *Plusia* moth, consists of a complicated herringbone-like microstructure that acts as a diffracting surface (see Fig. 3.1(a)). It is assumed that the electric (\vec{E}) and magnetic (\vec{H}) fields at any point on this surface follow the physical optics approximation discussed in ch. 2 sec. 2.1.5. The nett diffracted field at an observation point P in the far field is then given by the Stratton-Silver-Chu integral (Ch. 2 eq. (69)):

$$\vec{E}(P) = A\hat{k}^d \times \iint_S \left[\hat{n} \times \vec{E} - \eta\hat{k}^d \times (\hat{n} \times \vec{H}) \right] e^{ik(\hat{k}^d - \hat{k}^i) \cdot \vec{r}} dS, \quad (1)$$

where all symbols are defined in chapter 2.

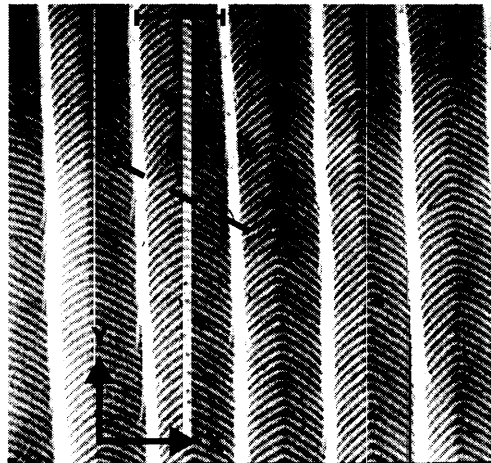


Fig. 3.1 (a) SEM-micrograph showing a top view of part of a scale from *Trichoplusia orichalcea*. The vertical lines are raised ridges spaced $1.6 \mu\text{m}$ apart (solid bar) and they are connected with a herringbone pattern of micro ribs spaced by 140 nm . Note that the centre of each herringbone strip is depressed by approximately 200 nm below the level of the vertical ridges.

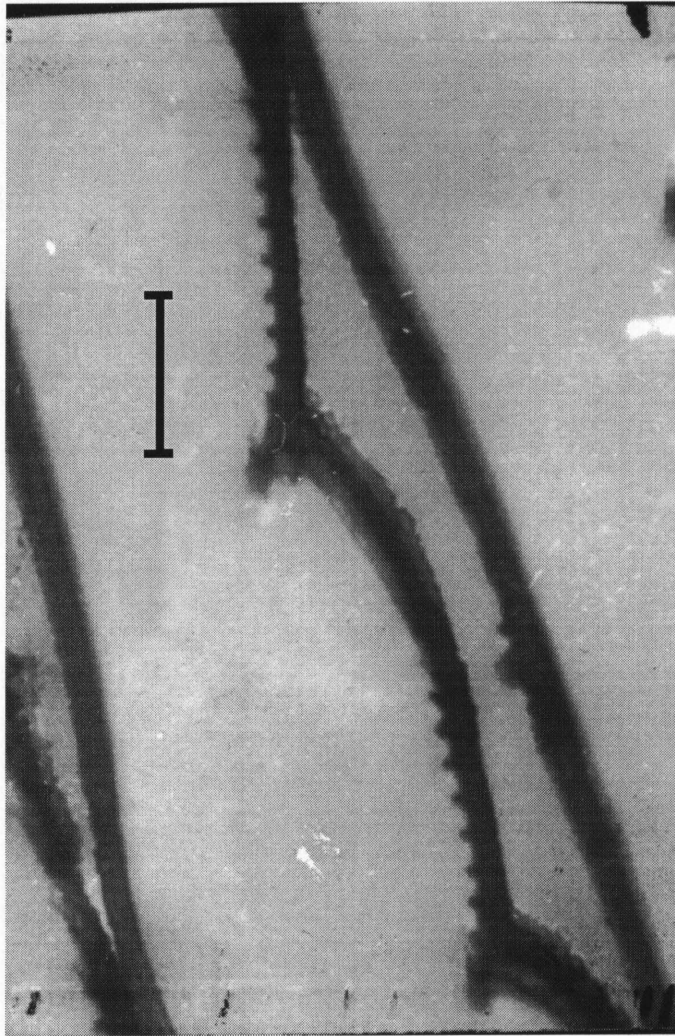


Fig. 3.1 (b) Oblique view of a wing scale. The solid bar is 0.5 μm . A dashed line on (a) indicates the view presented in this figure.

This chapter deals with the solution of eq.(1) for the moth wing and with the compilation of a computer program simulating the experimental results. The program is written in C++ and is listed in Appendix B. The model is also discussed by Brink [Brink D. J. *et al.* (1995) pp. 6049-6057].

1. Physical dimensions of the wing

Before commencing with the discussion of the solution to eq. (1), it is useful to define the physical dimensions of the wing. Values for the actual dimensions of the diffracting structure in the wing were obtained from the SEM-micrographs in Fig. 3.1(a) and (b) and are as follows:

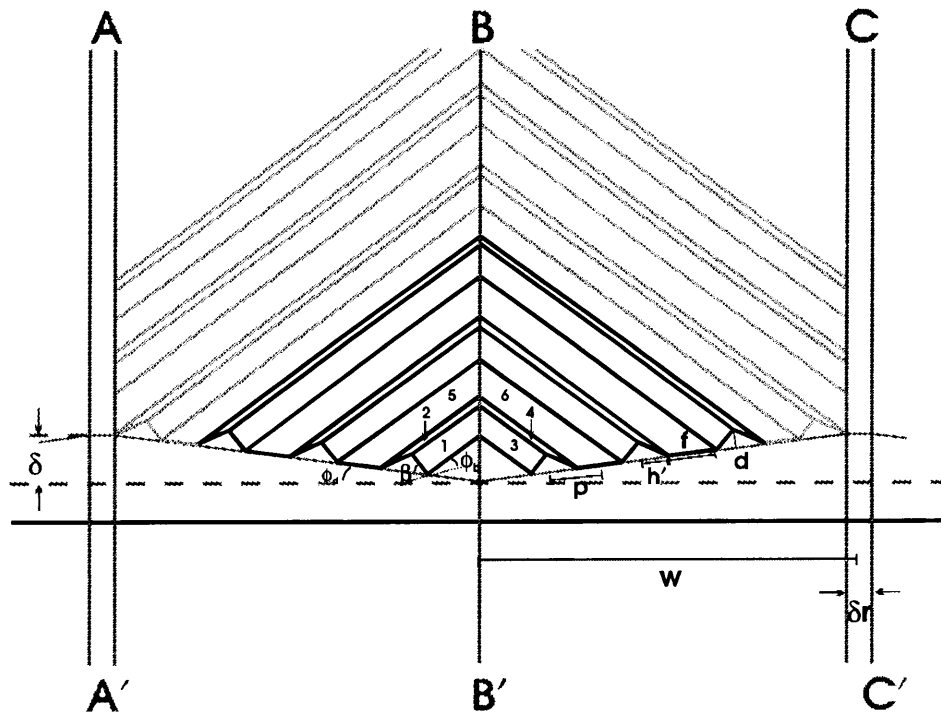


Fig. 3.2 Schematic representation of a part of the SEM-micrograph in Fig 3.1(a).

- Base angle: $\phi_b = 35^\circ$
- Wing depth: $d = 60 \text{ nm}$
- Pattern height: $h' = 60 \text{ nm}$
- Wing width, i.e. the length of one strip: $w = 810 \text{ nm}$
- Flat part of pattern: $f = 50 \text{ nm}$

- Wing half pattern repeat: $p = (f/2) + h' = 75 \text{ nm}$
- Wing ratio: $r = (f/2p) = 0.3$
- Depression of strip centre $\delta = 143 \text{ nm}$
- Angle of depression of the centre of the herringbone strip:

$$\phi_d = \arctan \frac{\delta}{\left(w - \frac{\delta r}{2}\right)} = \arctan \frac{143}{\left(810 - \frac{220}{2}\right)} \approx 10^\circ$$

A fixed real value of 1.56 [Land M. F. (1972)] was assumed for the index of refraction. In the program the index of refraction was treated as complex. In other words then: $\tilde{n} = n - ik$, where $n = 1.56$. For the simulations k was taken to be zero, except where stated otherwise.

2. Geometry of the wing

The wing of the moth can be approximated by a repetition of six differently orientated flat planes as shown in Fig. 3.3(a). Each type of plane can be described by a set of three orthogonal unit vectors: \hat{u} along the base of the rib, \hat{v} in the plane, but pointing to the top of the rib, and \hat{n} perpendicular to the plane pointing outward.

Fig. 3.3(b) shows the three co-ordinate systems used. They are as follows:

XYZ: This is a laboratory co-ordinate system. It includes the case where the wing is rotated in its own plane. The unit vectors for incidence and diffraction, \hat{k}^i and \hat{k}^d , lie in the XZ-plane.

$X'Y'Z'$: This co-ordinate system is fixed on the wing and represents the unrotated system. It is chosen in such a way that the base of the herringbone structure is parallel to the X' -axis.

$X''Y''Z''$: This is a local co-ordinate system. It is parallel to the $X'Y'Z'$ system and its origin is at a point $(x'_0, y'_0, 0)$ - the lower left corner of plane 1.

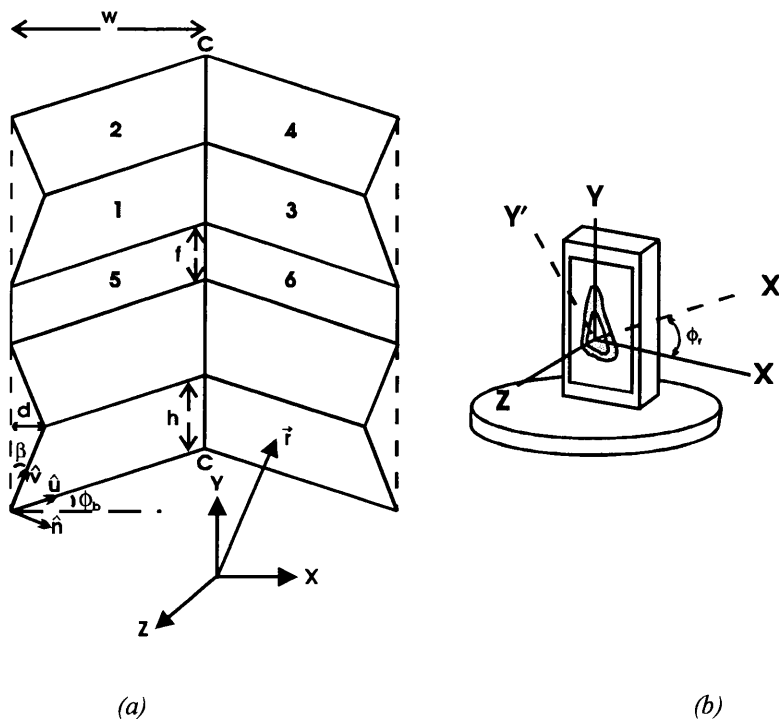


Fig. 3.3 (a) Schematic outline of the simplified diffracting structure. Line CC represents a valley between the raised ridges shown in Fig. 3.1(a). Distance d is the height of a micro rib along the Y-axis. If the depression of line CC is ignored, planes 5 and 6 would correspond to the plane of the wingscale.

(b) Schematic diagram of the three co-ordinate systems used in this work. XY is the lab system and includes the rotation of the wing. $X'Y'$ is the unrotated system and is fixed on the wing. The base of the herringbone structure is parallel to the X' -axis. $X''Y''$ is the local system and its X'' -axis is parallel to the X' -axis.

In order to evaluate the integral in eq. (1) all vectors and fields must be transformed to lie in the same co-ordinate system. The system that will be used is the local system. Since

the local and the unrotated system are parallel to each other, the quantities can be expressed in either system.

\hat{u} , \hat{v} and \hat{n} are thus unit vectors in the $X'Y'Z'$ system. Expression for \hat{u} , \hat{v} and \hat{n} will now be derived for the six different planes.

Plane 1:

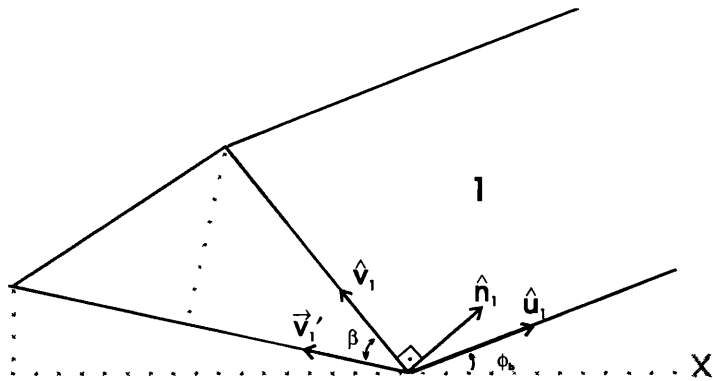


Fig. 3.4 Schematic drawing of plane 1. \hat{u} lies along the base of the rib, \hat{v} in the plane of the rib, pointing upwards and \hat{n} is perpendicular to both and to the plane of the rib.

From the geometry in Fig 3.4, \hat{u}_1 , \hat{v}_1 and \hat{n}_1 can be found in the following way:

Since \hat{u}_1 is a unit vector, $|\hat{u}_1| = 1$. Then:

$$u_{1x'} = \cos \phi_b$$

$$u_{1y'} = \sin \phi_b$$

$$u_{1z'} = 0$$

$$\text{or } \hat{u}_1 = (\cos \phi_b, \sin \phi_b, 0). \quad (2)$$

\vec{v}'_1 is the projection of \hat{v}_1 , projected onto the $X'Y'$ -plane through an angle β , while still keeping $\vec{v}'_1 \perp \hat{u}_1$. Since $\hat{v}_1 \perp \hat{u}_1$, $\hat{v}_1 \cdot \hat{u}_1 = 0$. Therefore

$$v_{1x'}u_{1x'} + v_{1y'}u_{1y'} = 0$$

or $\frac{v_{1x'}}{v_{1y'}} = -\tan \phi_b$.

Since $|\hat{v}_1| = 1$, $|\vec{v}'|$ can be written as $|\vec{v}'| = \cos \beta$. Thus

$$v_{1x'} = v'_{x'} = |\vec{v}'| \cos(90^\circ + \phi_b)$$

$$= -\cos \beta \sin \phi_b$$

$$v_{1y'} = v'_{y'} = |\vec{v}'| \sin(90^\circ + \phi_b)$$

$$= \cos \beta \cos \phi_b$$

$$v_{1z'} = v'_{z'} = \sqrt{1 - \cos^2 \beta (\cos^2 \phi_b + \sin^2 \phi_b)}$$

$$= \sqrt{1 - \cos^2 \beta}$$

or $\hat{v}_1 = (-\cos \beta \sin \phi_b, \cos \beta \cos \phi_b, \sqrt{1 - \cos^2 \beta})$. (3)

Since \hat{u}_1, \hat{v}_1 and \hat{n}_1 form a rectangular co-ordinate system,

$$\hat{n}_1 = \hat{u}_1 \times \hat{v}_1$$
 (4)

Plane 2:

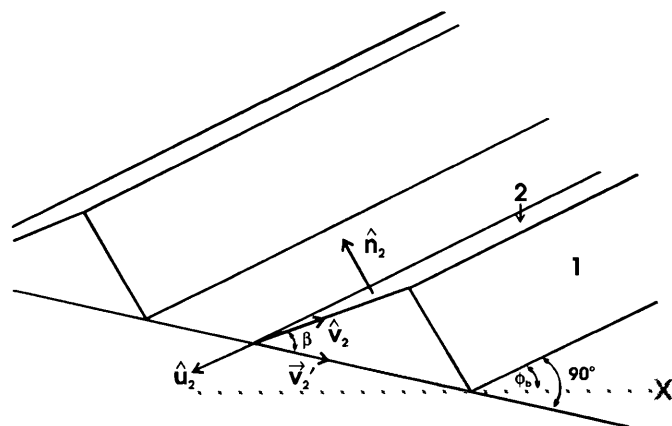


Fig. 3.5 Schematic drawing of plane 2. Now $\hat{u}_2 = -\hat{u}_1$ and $\hat{v}_2 = -\hat{v}_1$.

From Fig. 3.5 it is clear that $\hat{u}_2 = -\hat{u}_1$ or

$$\hat{u}_2 = (-\cos\phi_b, -\sin\phi_b, 0). \quad (5)$$

\hat{v}_2 can be found in the same way as \hat{v}_1 . As before $|\hat{v}_2| = \cos\beta$. Since the structure is assumed to be symmetric, the angle β is the same for all the planes. It follows that

$$\hat{v}_2 = (\cos\beta\sin\phi_b, -\cos\beta\cos\phi_b, \sqrt{1-\cos^2\beta}). \quad (6)$$

As before the local normal \hat{n}_2 is given by

$$\hat{n}_2 = \hat{u}_2 \times \hat{v}_2. \quad (7)$$

For planes 3 and 4, consider ridges which make an angle γ with planes 1 and 2.

Plane 3:

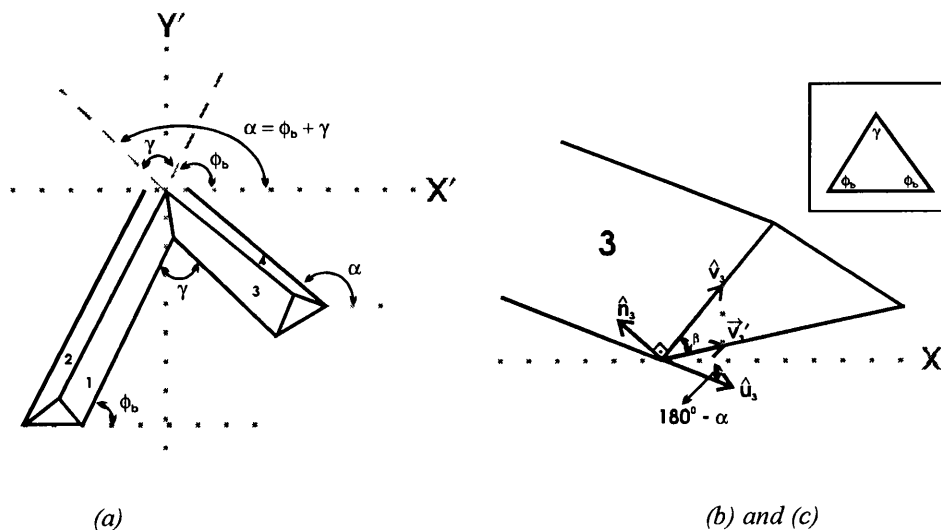


Fig. 3.6 (a) Schematic outline that depicts the relations between planes 1, 2 and 3, 4. γ is the angle between the two sets of planes. The angle (α) that plane 4 makes with the X' -axis is equal to the sum of γ and the base angle ϕ_b . (b) Schematic drawing of plane 3. (c) shows the relationship between γ and ϕ_b .

From the geometry in Fig. 3.6 it follows that

$$u_{3x'} = \cos(180^\circ - \alpha) = -\cos \alpha = -\cos(\phi_b + \gamma)$$

$$u_{3y'} = -\sin(180^\circ - \alpha) = -\sin \alpha = -\sin(\phi_b + \gamma)$$

$$u_{3z'} = 0.$$

Consider Fig. 3.6(c). It is clear that $\gamma + 2\phi_b = 180^\circ$ so that

$$\phi_b + \gamma = \phi_b + 180^\circ - 2\phi_b = 180^\circ - \phi_b.$$

\hat{u}_3 then becomes

$$\hat{u}_3 = (\cos \phi_b, -\sin \phi_b, 0). \quad (8)$$

Using the same reasoning as for planes 1 and 2

$$v_{3x'} = \cos \beta \sin \alpha_3 = \cos \beta \sin(\phi_b + \gamma) = \cos \beta \sin \phi_b$$

$$v_{3y'} = -\cos \beta \cos \alpha_3 = \cos \beta \cos \phi_b$$

$$v_{3z'} = \sqrt{1 - \cos^2 \beta}$$

$$\text{or } \hat{v}_3 = (\cos \beta \sin \phi_b, \cos \beta \cos \phi_b, \sqrt{1 - \cos^2 \beta}) \quad (9)$$

$$\text{and } \hat{n}_3 = \hat{u}_3 \times \hat{v}_3. \quad (10)$$

Plane 4:

Fig. 3.7 shows that similar to the case for plane 2,

$$\hat{u}_4 = -\hat{u}_3 = (-\cos \phi_b, \sin \phi_b, 0). \quad (11)$$

$$\hat{v}_4 = \left(-\cos\beta \sin\phi_b, -\cos\beta \cos\phi_b, \sqrt{1 - \cos^2\phi_b} \right). \quad (12)$$

$$\hat{n}_4 = \hat{u}_4 \times \hat{v}_4. \quad (13)$$

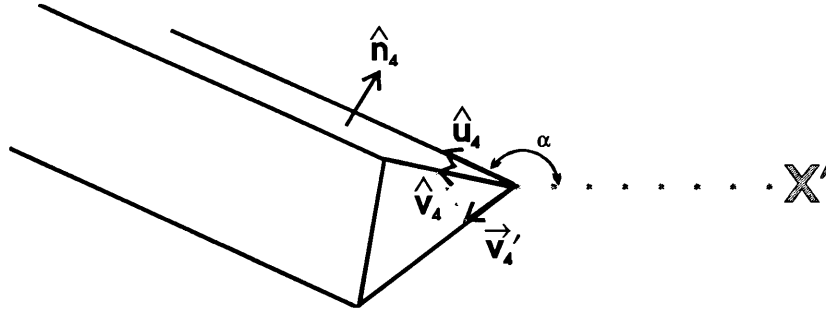


Fig. 3.7 Schematic drawing of plane 4.

Planes 5 and 6:

These planes are flat, so that the expressions for \hat{n}_5 and \hat{n}_6 are simply

$$\hat{n}_5 = \hat{n}_6 = (0, 0, 1). \quad (14)$$

3. Further generalisations

Before substituting the expressions for the surface normals into eq. (1), two further generalisations should be made. First, the wing can be rotated in its own plane (see Fig. 3.3). The surface normals of all the planes should then be rotated through an angle ϕ_r .

This rotation operation is accomplished by the transformations:

$$n_{jx'} = n_{jx} \cos\phi_r - n_{jy} \sin\phi_r$$

$$n_{jy'} = n_{jx} \sin\phi_r + n_{jy} \cos\phi_r$$

or in matrix form

$$\begin{bmatrix} n_{jx'} \\ n_{jy'} \end{bmatrix} = \begin{bmatrix} \cos \phi_r & -\sin \phi_r \\ \sin \phi_r & \cos \phi_r \end{bmatrix} \begin{bmatrix} n_{jx} \\ n_{jy} \end{bmatrix} \quad j = 1, \dots, 6. \quad (15)$$

Next, the centre of each herringbone strip is depressed by an angle ϕ_d (see Fig. 3.2). The surface normals of planes 1, 2 and 5 should thus be rotated clockwise through ϕ_d around the line CC in Fig. 3.3(a) and the normals of planes 3, 4 and 6 should be rotated counter clockwise through ϕ_d . The rotation operations are then:

Planes 1, 2 and 5:

$$n_{jx'} = n_{jx} \cos \phi_d + n_{jz} \sin \phi_d$$

$$n_{jy'} = n_{jy}$$

$$n_{jz'} = -n_{jy} \sin \phi_d + n_{jz} \cos \phi_d.$$

Planes 3, 4 and 6:

$$n_{jx'} = n_{jx} \cos \phi_d - n_{jz} \sin \phi_d$$

$$n_{jy'} = n_{jy}$$

$$n_{jz'} = n_{jx} \sin \phi_d + n_{jz} \cos \phi_d.$$

or in matrix form

$$\begin{bmatrix} n_{jx'} \\ n_{jz'} \end{bmatrix} = \begin{bmatrix} \cos \phi_d & \pm \sin \phi_d \\ \mp \sin \phi_d & \cos \phi_d \end{bmatrix} \begin{bmatrix} n_{jx} \\ n_{jz} \end{bmatrix} \quad j = 1, \dots, 6. \quad (16)$$

4. Position vector (\vec{r}) of an arbitrary point on the wing.

In Fig. 3.8(a), let \vec{f} be a vector from the origin to a point (x, y, z) on the plane. \hat{e} is a unit vector perpendicular on the plane from the origin. Then

$$\vec{f} \cdot \hat{e} = d, \quad (17)$$

where d is the distance from the origin to the plane.

In the local system (see Fig. 3.3(b)), the lower left corner of a plane is the origin, thus the distance from the origin to the plane is zero. The equation of a plane, in the local system is then according to equation (17):

$$x''n_{jx'} + y''n_{jy'} + z''n_{jz'} = 0 \quad (18a)$$

$$\text{or} \quad n_{jx'}(x' - x'_0) + n_{jy'}(y' - y'_0) + n_{jz'}(z' - z'_0) = 0. \quad j = 1, \dots, 6. \quad (18b)$$

where (x'_0, y'_0, z'_0) are the co-ordinates of the lower left corner of a plane in the non-local co-ordinate system fixed on the wing. For planes 1, 3, 5 and 6 $z'_0 = 0$ so that

$$z' = -\frac{n_{jx'}}{n_{jz'}}(x' - x'_0) - \frac{n_{jy'}}{n_{jz'}}(y' - y'_0). \quad (19a)$$

For planes 2 and 4 $z'_0 = d$, giving

$$z' = d - \frac{n_{jx'}}{n_{jz'}}(x' - x'_0) - \frac{n_{jy'}}{n_{jz'}}(y' - y'_0). \quad (19b)$$

Fig. 3.8(b) shows the indexing used in the program. The index in the X' direction is p and the index in the Y' direction is q . Note that planes 2 and 5 and again 4 and 6 are represented by the same index. For the simulation of the moth wing values of 2 and 40 were used for p and q respectively. This choice will be discussed in more detail in the chapter on results and discussions.

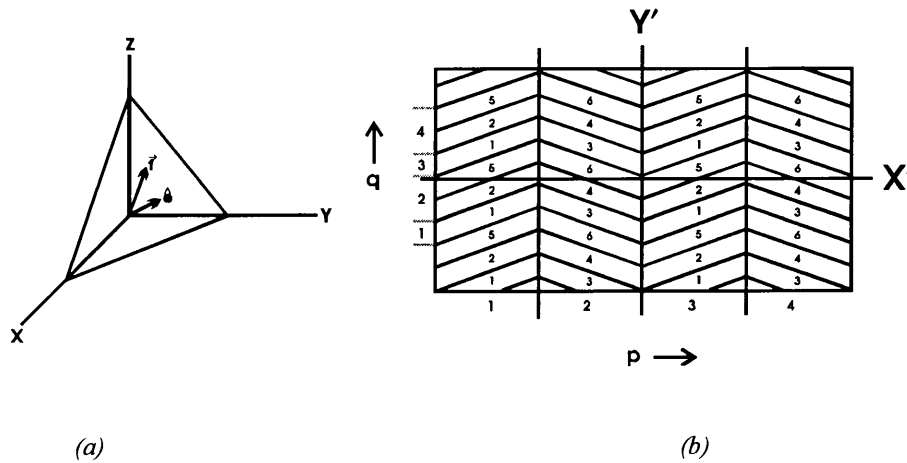


Fig. 3.8 (a) Diagram of an arbitrary plane surface. Vector \vec{r} is the vector from the origin to a point (x, y, z) on the plane and \hat{e} is a unit vector perpendicular to the plane from the origin. (b) Schematic diagram showing the indexing in the X' -axis and Y' -axis directions.

Therefore

$$\begin{aligned}
 x_p &= x'_0 \\
 y_q &= y'_0 \\
 z_{pq} &= z'_0
 \end{aligned}
 \tag{20}$$

so that equations (19a) and (19b) change to

$$z' = -\frac{n_{jx'}}{n_{jz'}}(x' - x_p) - \frac{n_{jy'}}{n_{jz'}}(y' - y_q).
 \tag{21a}$$

$$z' = d - \frac{n_{jx'}}{n_{jz'}}(x' - x_p) - \frac{n_{jy'}}{n_{jz'}}(y' - y_q).
 \tag{21b}$$

Since the vector \vec{r} is the vector from the origin to an arbitrary point (x', y', z') on the wing, it follows that

$$\vec{r}_{pq} = \left(x', y', z_{pq} - \frac{n_{jx'}}{n_{jz'}}(x' - x_p) - \frac{n_{jy'}}{n_{jz'}}(y' - y_q) \right).
 \tag{22}$$

At this point the geometry of the wing is completely defined in a format suitable for substitution in the Stratton-Silver-Chu integral.

5. The directions of the input and output beams

As in Chapter 2 Section 2.1.2, the unit vectors along the directions of incidence and diffraction, \hat{k}^i and \hat{k}^d respectively, are chosen to lie in the XZ-plane (see Fig. 2.2). In this case the angle of incidence is θ_i and the angle of diffraction is $\theta_d = \theta_i \pm \Delta$. By considering the incidence along a line $z = -x \tan(90^\circ - \theta_i) = -x \cot \theta_i$, it is possible to define vector \hat{k}^i as the vector from the origin to a point $(1, 0, -\cot \theta_i)$. From the definition of the unit vector it then follows that

$$\begin{aligned}\hat{k}^i &= \frac{(1, 0, -\cot \theta_i)}{\sqrt{1 + \cot^2 \theta_i}} \\ &= (\sin \theta_i, 0, -\cos \theta_i).\end{aligned}\tag{23a}$$

If reflection / diffraction along the line $z = x \tan(90^\circ - \theta_d) = x \cot \theta_d$ is considered, then \hat{k}^d can be defined as the vector from the origin to a point $(1, 0, \cot \theta_d)$. Then

$$\begin{aligned}\hat{k}^d &= \frac{(1, 0, \cot \theta_d)}{\sqrt{1 + \cot^2 \theta_d}} \\ &= (\sin \theta_d, 0, \cos \theta_d).\end{aligned}\tag{23b}$$

θ_i and θ_d lie in the XYZ-system. To find their corresponding angles, θ_i^L and θ_d^L in the local system, i.e. the X'Y'Z'-system, use the transformations

$$\cos \theta_j^L = -\hat{k}^i \cdot \hat{n}_j \quad j = 1, \dots, 6.\tag{24a}$$

and

$$\cos\theta_i^L = \sqrt{1 - \frac{\sin^2(\cos^{-1}\theta_i^L)}{\tilde{n}^2}}. \quad (24b)$$

Equations (24a) and (24b) will be used in the next section to calculate the Fresnel reflection coefficients.

6. The electric and magnetic fields

The total electric (\vec{E}) and magnetic (\vec{H}) fields in eq. (1) are equal to the sum of the incident \vec{E}^i, \vec{H}^i and scattered \vec{E}^d, \vec{H}^d fields respectively. It is the same as the formalism used in Ch. 2 and many of the expressions used in Ch. 2 Sec. 2.1.2 are applicable here. The purpose of this section is to find expressions for the electric and magnetic fields in the external and local co-ordinate systems.

6.1 The polarized external electric field

The external incident and scattered beams may be polarized, so an external polarization angle θ_p is defined as follows: consider a set-up as in Fig. 3.9(a), where θ_p is the angle in the YZ-plane between the electric vector (\vec{E}) and the Y-axis. Every electric vector can be decomposed into two components, namely a p-component parallel to the plane of incidence and a s-component perpendicular to the plane. Therefore, when $\theta_p = 0^\circ$ or 90° s- or p-polarization is indicated respectively.

It is possible to write any polarized electric field \vec{E} in the form of a Jones vector [Hecht E. (1989) pp. 323-324]:

$$\vec{E} = \begin{bmatrix} \tilde{E}_x(t) \\ \tilde{E}_y(t) \end{bmatrix} \quad (25)$$

where $\tilde{E}_x(t)$ and $\tilde{E}_y(t)$ gives the two components in the different states of polarization of \tilde{E} respectively. There can be a phase difference between $\tilde{E}_x(t)$ and $\tilde{E}_y(t)$, since both are complex.

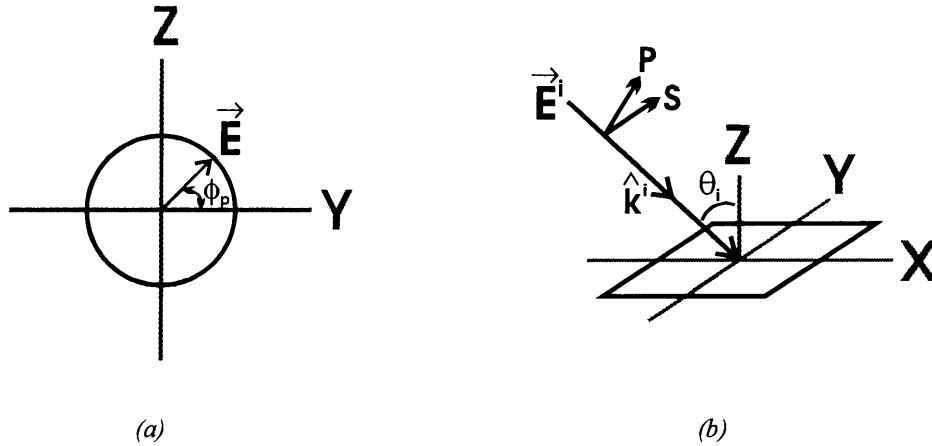


Fig. 3.9 (a) Schematic drawing showing the polarization angle θ_p . (b) Schematic drawing showing the incident electric vector \tilde{E}^i . The unit vector in the direction of incidence is \hat{k}^i . The s-component of the electric vector lies in the Y-axis direction and the p-component in the Z-axis direction and both are perpendicular to \hat{k}^i .

The incident electric field \tilde{E}^i can therefore be written as a Jones vector in terms of its p- and s-components as:

$$\tilde{E}^i = \begin{bmatrix} E_{is}^E \\ E_{ip}^E \end{bmatrix} = \begin{bmatrix} \cos\theta_p \\ \sin\theta_p \end{bmatrix}. \quad (26)$$

By letting $\tilde{E}^i = (E_{ix}, E_{iy}, E_{iz})$, it follows that

$$\begin{aligned} E_{ix} &= E_{ip}^E \cos\theta_i = \sin\theta_p \cos\theta_i \\ E_{iy} &= E_{is}^E = \cos\theta_p \\ E_{iz} &= E_{ip}^E \sin\theta_i = \sin\theta_p \sin\theta_i. \end{aligned} \quad (27)$$

It is thus clear that an s-polarized input beam ($\theta_p = 0$) has an electric field along the Y-axis, i.e. the external s-component lies in the XY-plane along the Y-axis.

6.2 Incidence and scattering from the local surface

\vec{E}^i can now be transformed to its local counterpart.

From Fig. 3.5(b) it can be seen that the s- and p-components lie in a plane perpendicular to \hat{k}^i , which is also true for the local s- and p-components.

Let the local incident electric field be

$$\vec{E}^{iL} = \begin{bmatrix} E_{is}^L \\ E_{ip}^L \end{bmatrix} \quad (28)$$

and let the local unit vectors along E_{is}^L and E_{ip}^L be \hat{e}_{is}^L and \hat{e}_{ip}^L respectively. Since \hat{e}_{is}^L is perpendicular to the local plane of incidence, it is perpendicular to \hat{k}^i and \hat{n}_j , $j = 1, \dots, 6$. Therefore

$$\hat{e}_{is}^L = \frac{\hat{n}_j \times \hat{k}^i}{|\hat{n}_j \times \hat{k}^i|} \quad j = 1, \dots, 6. \quad (29a)$$

Now, \hat{e}_{ip}^L is perpendicular to both \hat{e}_{is}^L and \hat{k}^i and therefore

$$\hat{e}_{ip}^L = \hat{e}_{is}^L \times \hat{k}^i. \quad (29b)$$

The components of the local incident electric field are then

$$\begin{aligned} E_{is}^L &= \vec{E}^i \cdot \hat{e}_{is}^L \\ E_{ip}^L &= \vec{E}^i \cdot \hat{e}_{ip}^L. \end{aligned} \quad (30)$$

When an electric field is incident on a surface of a material, part of it is scattered and part of it is transmitted into the material. The relationships between these three electric

vectors are given by the Fresnel equations [see for example Hecht E. (1989) pp. 94-104]. From these equations one can find the Fresnel reflection coefficients

$$\begin{aligned}
 r_s &= \frac{n_0 \cos \theta_i^L - \tilde{n} \cos \theta_t^L}{n_0 \cos \theta_i^L + \tilde{n} \cos \theta_t^L} \\
 r_p &= \frac{\tilde{n} \cos \theta_i^L - n_0 \cos \theta_t^L}{\tilde{n} \cos \theta_i^L + n_0 \cos \theta_t^L},
 \end{aligned}
 \tag{31}$$

where n_0 is the index of refraction of air (≈ 1),

$\tilde{n} = 1.56 - 0i$ is the index of refraction of the wing and

θ_t^L is given by Snell's law: $\tilde{n} \sin \theta_t^L = n_0 \sin \theta_i^L$.

Note that θ_t^L and therefore also r_p and r_s can be complex.

Let the local scattered electric field (\vec{E}^{dL}) be given by

$$\vec{E}^{dL} = \begin{bmatrix} E_{ds}^L \\ E_{dp}^L \end{bmatrix}.
 \tag{32}$$

Using equations (31) gives

$$\vec{E}^{dL} = \begin{bmatrix} r_s E_{is}^L \\ r_p E_{ip}^L \end{bmatrix}
 \tag{33}$$

for the local scattered electric field.

6.3 The external scattered electric field

To complete the picture for the scattered electric field (\vec{E}^d) it must be transformed back to its external counterpart.

In the local system the unit vector in the scattered direction, \hat{k}^d , is given by eq. (47a) in Ch. 2:

$$\hat{k}^d = \hat{k}^i - 2(\hat{n}_j \cdot \hat{k}^i)\hat{n}_j \quad j = 1, \dots, 6. \quad (34)$$

Following the same reasoning as was used to find \hat{e}_{is}^L and \hat{e}_{ip}^L , \hat{e}_{ds}^L and \hat{e}_{dp}^L are given by

$$\hat{e}_{ds}^L = \frac{\hat{n}_j \times \hat{k}^d}{|\hat{n}_j \times \hat{k}^d|} \quad j = 1, \dots, 6 \quad (35a)$$

$$\hat{e}_{dp}^L = \hat{e}_{ds}^L \times \hat{k}^d. \quad (35b)$$

It then follows that

$$\vec{E}^d = \vec{E}^{dL} \cdot \hat{e}^{dL} \quad (36)$$

where $\hat{e}^{dL} = \begin{bmatrix} \hat{e}_{ds}^L \\ \hat{e}_{dp}^L \end{bmatrix}$.

The total electric field is then given by the sum of the incident and scattered electric fields.

6.4 The incident and scattered magnetic fields

To find the magnetic fields is straightforward. In Ch. 2 Sec. 2.1.2 the expressions for the incident (\vec{H}^i) and scattered (\vec{H}^d) magnetic fields were given by eqs. (48a) and (48b):

$$\vec{H}^i = \frac{1}{\eta}(\hat{k}^i \times \vec{E}^i)$$

$$\vec{H}^d = \frac{1}{\eta}(\hat{k}^d \times \vec{E}^d).$$

The total magnetic field (\vec{H}) is then simply equal to the sum of these two components.

7. Solution to the Stratton-Silver-Chu integral

All the quantities in eq. (1) have now been addressed and the integral can now be evaluated.

In order to evaluate this integral for the moth wing, approximated by a large number of oriented flat planes, it is useful to split it into a sum of terms, one for each plane:

$$\vec{E}(P) = A \sum_{j=1}^6 \hat{k}^d \times \left[(\hat{n}_j \times \vec{E}_j) - \eta \hat{k}^d \times (\hat{n}_j \times \vec{H}_j) \sum_{p,q} \iint e^{ik(\hat{k}^d - \hat{k}^i) \cdot \vec{r}_{pq}} dx' dy' \right] \quad (37)$$

First, define $\Delta \vec{k} = k(\hat{k}^d - \hat{k}^i) = (\Delta k_{x'}, \Delta k_{y'}, \Delta k_{z'})$.

Substituting \vec{r}_{pq} from eq. (22) allows evaluation of the surface integral:

$$I = \iint e^{ik(\hat{k}^d - \hat{k}^i) \cdot \vec{r}_{pq}} dx' dy'. \quad (38)$$

The integral in eq. (38) will be evaluated in full for plane 1 and the results for planes 2 to 6 will only be stated since the arguments are very similar.

For plane 1 \vec{r}_{pq} is given by

$$\vec{r}_{pq} = \left(x', y', \delta - \frac{n_{jx'}}{n_{jz'}}(x' - x_p) - \frac{n_{jy'}}{n_{jz'}}(y' - y_q) \right) \quad (39)$$

where δ is defined in Fig. 3.2. Taking the dot product of $\Delta \vec{k}$ and \vec{r}_{pq} gives:

$$\begin{aligned} \Delta \vec{k} \cdot \vec{r}_{pq} = & \left(\Delta k_{x'} - \Delta k_{z'} \frac{n_{jx'}}{n_{jz'}} \right) x' + \left(\Delta k_{y'} - \Delta k_{z'} \frac{n_{jy'}}{n_{jz'}} \right) y' \\ & + \Delta k_{z'} x_p \frac{n_{jx'}}{n_{jz'}} + \Delta k_{z'} y_q \frac{n_{jy'}}{n_{jz'}} + \delta \Delta k_{z'} \end{aligned} \quad (40)$$

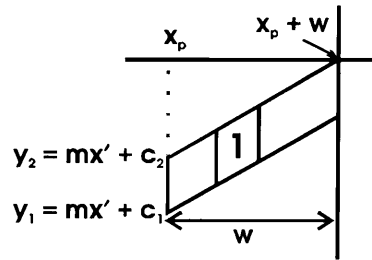


Fig. 3.10 A schematic drawing to show the boundaries over x' and y' where x_p and y_q are the coordinates of the lower corner of the plane.

The next step is to consider the boundaries of the surface integral. The boundaries for x' is simply x_p and $x_p + w$ (see Fig. 3.10). The lower and upper boundaries for y' can be written in terms of the equations for a straight line, namely

$$y_1 = mx' + c_1 \text{ and } y_2 = mx' + c_2 \quad (41)$$

where c_1 , c_2 and m are given by

$$y_q = mx_p + c_1 \Rightarrow c_1 = y_q - mx_p$$

$$y_q + h = mx_p + c_2 \Rightarrow c_2 = y_q + h - mx_p \quad (42)$$

$$m = \tan \phi_b .$$

Substituting equations (40), (41) and (42) into (39) gives

$$I_1 = \iint e^{ik(\hat{k}^d - \hat{k}^i) \cdot \vec{r}_{pq}} dx' dy' \\ = e^{i\left(\Delta k_x x_p \frac{n_{jx'}}{n_{jz'}} + \Delta k_x y_q \frac{n_{jy'}}{n_{jz'}} + \delta \Delta k_x\right)} \int_{x_p}^{x_p+w} e^{i\left(\Delta k_x - \Delta k_x \frac{n_{jx'}}{n_{jz'}}\right) x'} dx' \int_{y_1}^{y_2} e^{i\left(\Delta k_y - \Delta k_x \frac{n_{jy'}}{n_{jz'}}\right) y'} dy' \quad (43)$$

Integrating to y' gives:

$$I_1 = e^{i\left(\Delta k_x x_p \frac{n_{jx'}}{n_{jz'}} + \Delta k_x y_q \frac{n_{jy'}}{n_{jz'}} + \delta \Delta k_x\right)} \int_{x_p}^{x_p+w} e^{i\left(\Delta k_x - \Delta k_x \frac{n_{jx'}}{n_{jz'}}\right) x'} dx' \left\{ \frac{1}{i\Delta_1} \left[e^{i\Delta_1 y_2} - e^{i\Delta_1 y_1} \right] \right\} \\ = e^{i\left(\Delta k_x x_p \frac{n_{jx'}}{n_{jz'}} + \Delta k_x y_q \frac{n_{jy'}}{n_{jz'}} + \delta \Delta k_x\right)} \int_{x_p}^{x_p+w} e^{i\left(\Delta k_x - \Delta k_x \frac{n_{jx'}}{n_{jz'}} + m\Delta_1\right) x'} dx' \left\{ \frac{h}{i\theta_1} e^{i\Delta_1(y_q - mx_p)} \left[e^{i\theta_1} - 1 \right] \right\} \quad (44a)$$

$$\text{where } \theta_1 = \Delta_1 \cdot h = \left(\Delta k_{y'} - \Delta k_{z'} \frac{n_{jy'}}{n_{jz'}} \right) \cdot h. \quad (44b)$$

Now integrate equation (44) to x' :

$$\begin{aligned} I_1 &= e^{i \left(\Delta k_{z'} x_p \frac{n_{jx'}}{n_{jz'}} + \Delta k_{z'} y_q \frac{n_{jy'}}{n_{jz'}} + \delta \Delta k_{z'} \right) x_p + w} \int_{x_p}^{x_p+w} e^{i \left(\Delta k_{x'} - \Delta k_{z'} \frac{n_{jx'}}{n_{jz'}} + m \Delta_1 \right) x'} dx' \left\{ \frac{h}{i \theta_1} e^{i \Delta_1 (y_q - m x_p)} [e^{i \theta_1} - 1] \right\} \\ &= \frac{h}{i \theta_1} e^{i \left(\Delta k_{z'} x_p \frac{n_{jx'}}{n_{jz'}} + \Delta k_{z'} y_q \frac{n_{jy'}}{n_{jz'}} + \delta \Delta k_{z'} + (y_q - m x_p) \cdot \frac{\theta_1}{h} \right)} [e^{i \theta_1} - 1] \left\{ \int_{x_p}^{x_p+w} e^{i \left(\Delta k_{x'} - \Delta k_{z'} \frac{n_{jx'}}{n_{jz'}} + m \frac{\theta_1}{h} \right) x'} dx' \right\} \quad (45a) \\ &= \frac{h}{i \theta_1} e^{i \left(\Delta k_{z'} x_p \frac{n_{jx'}}{n_{jz'}} + \Delta k_{z'} y_q \frac{n_{jy'}}{n_{jz'}} + \delta \Delta k_{z'} + (y_q - m x_p) \cdot \frac{\theta_1}{h} \right)} [e^{i \theta_1} - 1] \left\{ \frac{w}{i \theta_2} e^{i \Delta_2 x_p} [e^{i \theta_2} - 1] \right\} \end{aligned}$$

$$\text{where } \theta_2 = \Delta_2 \cdot w = \left(\Delta k_{x'} - \Delta k_{z'} \frac{n_{jx'}}{n_{jz'}} + \frac{m \theta_1}{h} \right) \cdot w. \quad (45b)$$

The final solution is therefore

$$\begin{aligned} I_1 &= -h w \cdot e^{i \left(\Delta k_{z'} x_p \frac{n_{jx'}}{n_{jz'}} + \Delta k_{z'} y_q \frac{n_{jy'}}{n_{jz'}} + \delta \Delta k_{z'} + (y_q - m x_p) \cdot \frac{\theta_1 + \theta_2}{h} \right)} \left(\frac{e^{i \theta_1} - 1}{\theta_1} \right) \left(\frac{e^{i \theta_2} - 1}{\theta_2} \right) \\ &= -h w \cdot \left(\frac{e^{i \theta_1} - 1}{\theta_1} \right) \left(\frac{e^{i \theta_2} - 1}{\theta_2} \right) e^{i \theta_3} \quad (46a) \end{aligned}$$

$$\text{where } \theta_3 = \Delta k_{x'} x_p + \Delta k_{y'} y_q + \Delta k_{z'} \delta. \quad (46b)$$

In general then the integral will be

$$\iint e^{i k (\hat{k}^d - \hat{k}^l) \cdot \vec{r}_{pq}} dx' dy' = -l \cdot w \left(\frac{e^{i \theta_1} - 1}{\theta_1} \right) \left(\frac{e^{i \theta_2} - 1}{\theta_2} \right) e^{i \theta_3} \quad (47)$$

$$\text{where } \theta_1 = \left(\Delta k_{y'} - \Delta k_{z'} \frac{n_{jy'}}{n_{jz'}} \right) \cdot l$$

with $l = h$ for planes 1, 2, 3, 4 and $l = f$ for planes 5 and 6,

$$\theta_2 = \left(\Delta k_{x'} - \Delta k_{z'} \frac{n_{jx'}}{n_{jz'}} + \frac{m\theta_1}{h} \right) w,$$

$$\theta_3 = \Delta k_{x'} x_p + \Delta k_{y'} y_q + \Delta k_{z'} z_{pq}$$

$$\text{and } \Delta \vec{k} = k(\hat{k}^d - \hat{k}^i).$$

The values of m and z_{pq} for planes 2 to 6 are:

$$m = \begin{cases} \tan \phi_b & \text{for planes 2 and 5} \\ -\tan \phi_b & \text{for planes 3, 4 and 6,} \end{cases}$$

$$z_{pq} = \begin{cases} \delta & \text{for plane 5} \\ 0 & \text{for planes 3 and 6} \\ \delta + d & \text{for plane 2} \\ d & \text{for plane 4} \end{cases}$$

Under certain conditions the integral in eq. (47) develops an apparent singularity when either θ_1 or $\theta_2 \rightarrow 0$. Consider a general term

$$T = \left(\frac{e^{i\theta} - 1}{\theta} \right). \quad (48)$$

This can be rewritten as

$$T = \frac{\cos \theta + i \sin \theta - 1}{\theta} = \frac{\cos \theta - 1}{\theta} + \frac{i \sin \theta}{\theta}. \quad (49)$$

Application of L'Hopitals rule to the two terms on the right hand side leads to:

$$T = 0 + i \text{ as } \theta \rightarrow 0. \quad (50)$$

In the program θ is considered zero when it is smaller than 1×10^{-30} .

The last point that has to be considered is the case of shadowing. In section 5 the cosine of the local angle of incidence (eq. (24a)) was given as

$$\cos\theta_i^L = -\hat{\mathbf{k}}^i \cdot \hat{\mathbf{n}}_j \quad j = 1, \dots, 6. \quad (51)$$

Shadowing occurs when the LHS (or RHS) of eq. (51) becomes negative. This means that no light falls on that part of the surface and accordingly nothing is scattered from the surface. The total electric and magnetic fields for that part of the surface are thus zero.

The Stratton-Silver-Chu integral is now solved for the moth wing. It does not explain in full all the phenomena seen in the experimental measurements due to shortcomings inherent to some of the assumptions Silver made (see Chapter 2). The nature of the shortcomings will be discussed in the chapter on results and discussions.

CHAPTER 4

MATHEMATICAL MODELLING OF THE LASER INDUCED PERIODIC SURFACE (LIPS) STRUCTURES

In chapter 3 the Stratton-Silver-Chu integral was used to model the wing of the *Trichoplusia orichalcea* moth. The modelling of the laser induced periodic surface (LIPS) structures, studied in this work and previously described by Brink [Brink D. J. and Smit J. E. (1993) pp. 189-193] is based on the same model, except for a few alterations which will be discussed here. The revised computer model is listed in Appendix C.

1. Geometry of the LIPS-structure

As was previously shown in chapter 1, the LIPS-structure can be approximated by a sinusoidal pattern with a period Λ equal to the wavelength of the ruby laser. Fig. 4.1(a) is a schematic drawing of part of the LIPS-structure, with height H . Each period is subdivided into s_{\max} divisions. The position (x_s) and the height (z_s) of each division can be described by

$$x_s = \frac{s}{s_{\max}} \Lambda - \frac{\Lambda}{2s_{\max}} \quad s = 1, \dots, s_{\max} \quad (1)$$

and

$$z_s = \frac{H}{2} \left[\sin \left(\frac{2\pi x_s}{\Lambda} - \frac{\pi}{2} \right) + 1 \right] \quad (2)$$

respectively. The factor $\frac{\Lambda}{2s_{\max}}$ in (1) ensures that x_s indicates the centre position of a subdivision.

The co-ordinate systems used here is the same as that for the moth-model. The indexing of the total structure (see Fig. 4.1(b)) is given by p_{\max} units in the X-direction (where each p is subdivided into s_{\max} units) and q_{\max} units in the Y-direction.

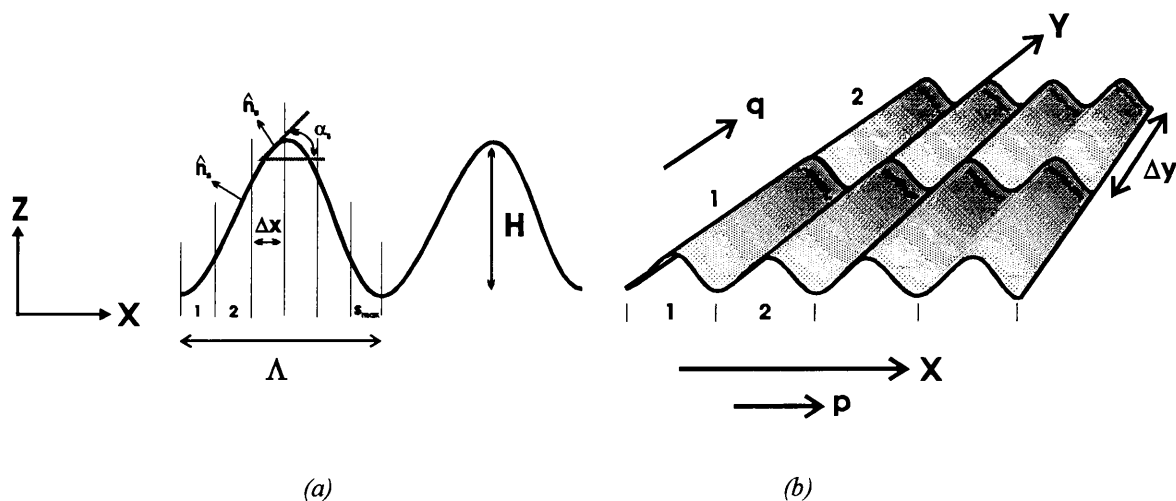


Fig. 4.1 (a) A drawing showing the geometry of the LIPS-structure. Each period, Λ , is subdivided into s_{\max} units, each having a width Δx . The height of the structure is H . (b) Another view of the LIPS-structure showing the indices in the X- and Y- directions.

2. The surface normals

In the moth-model the surface normals were specified for each plane, but here the surface normals must be specified for each subdivision, s , of the period Λ . They are of the form

$$\hat{n}_s = (n_{xs}, 0, n_{zs}) \quad s = 1, \dots, s_{\max} \quad (3)$$

where $(n_{xs})^2 + (n_{zs})^2 = 1$, since \hat{n}_s is a unit vector. To find \hat{n}_s , one first needs to find the gradient \vec{g}_s of the surface. Now

$$\begin{aligned} g_s &= \frac{dz_s}{dx_s} = \frac{d}{dx_s} \left\{ \frac{H}{2} \left[\sin \left(\frac{2\pi x_s}{\Lambda} - \frac{\pi}{2} \right) + 1 \right] \right\} \\ &= \frac{\pi H}{\Lambda} \cos \left(\frac{2\pi x_s}{\Lambda} - \frac{\pi}{2} \right). \end{aligned} \quad (4)$$

Then

$$\tan \alpha_s = g_s \quad (5)$$

with α_s defined in Fig. 4.1(a). The gradient of the surface is then given by

$$\vec{g}_s = (\cos \alpha_s, 0, \sin \alpha_s). \quad (6)$$

Since $\hat{n}_s \cdot \vec{g}_s = 0$ it follows that the surface normal is given by:

$$\hat{n}_s = (-\sin \alpha_s, 0, \cos \alpha_s). \quad (7)$$

The minus sign ensures that the surface normal is directed outwards.

3. The direction of the input and output beams

The unit vectors for the input and output beams do not differ from ch. 3, but here the angles of incidence and diffraction, θ_i and θ_d , are the same, i.e. $\theta_i = \theta_d = 70^\circ$.

In the moth-model it was shown that (see ch. 3 eqs. (23a) and (23b))

$$\begin{aligned} \hat{k}^i &= (\sin \theta_i, 0, -\cos \theta_i) \\ \hat{k}^d &= (\sin \theta_d, 0, \cos \theta_d). \end{aligned}$$

Therefore

$$\Delta \vec{k} = k(\hat{k}^d - \hat{k}^i) = k(0, 0, 2 \cos \theta_i). \quad (8)$$

The counterparts of $\hat{k}^{i,d}$ in the local system ($X'Y'Z'$ -system), will change accordingly.

4. The height of the structure

The input for the computer model (app. C) included the energies at the top (E_{max}) and bottom (E_{min}) of the structure, and the penetration depth (d). From these energies the temperatures at the bottom and the top of the structure are calculated by an approximate expression [Brink D. J. and Smit J. E. (1993) pp. 189-193]

$$\Delta T = \frac{(1-R)tE_{out}}{\rho C_p a d} \quad (9)$$

where ΔT is the temperature rise from 300 K, R is the reflectivity of the silicon surface, t is the transmission of the beam delivery system (70%), E_{out} is the output energy between E_{min} and E_{max} of the ruby laser, ρ and C_p are the density and heat capacity of silicon, and a and d are the effective illuminated area and penetration depth. It should be noted that the detailed dynamics of heat diffusion is ignored in eq. (9) which only gives an average value for the temperature rise immediately after the laser pulse. It is therefore only accurate if the laser pulse length is short compared to the thermal diffusion time. The values of a and t are taken from the chapter on measuring techniques and apparatus. Expressions for ρ and C_p are given by [Marais T. K. *et al.* (1990) pp. 111-119] :

$$\rho = \begin{cases} 2.33 \text{ gcm}^{-3} & T \leq 1685K \\ 2.53 \text{ gcm}^{-3} & T > 1685K \end{cases} \quad (10)$$

and

$$C_p = \begin{cases} 0.8406 + 1.1773 \times 10^{-4} T + 1.4723 \times 10^{-8} T^2 & Jg^{-1}K^{-1} & T \leq 1685K \\ 0.8531 + 4.173 \times 10^{-5} T + 3.0217 \times 10^{-8} T^2 & Jg^{-1}K^{-1} & T > 1685K \end{cases} \quad (11)$$

To calculate ΔT in eq. (9) the values for ρ and C_p were taken as 2.33 gcm^{-3} and an average (for solid silicon) of $0.98 \text{ J g}^{-1} \text{ K}^{-1}$ respectively. An average of 0.37 (for solid silicon) was used for R .

When the material melts, there is a phase transition. The energy needed for melting can be readily calculated from the latent heat of fusion (1800 Jg^{-1}) for solid silicon [Wood R. F. *et al.* (1984) pp.189]. Only when the energy rises above this melting energy, will the temperature start to rise again.

The height (H) of the structure can be approximated by

$$H = d(\beta_{\max} T_{\max} - \beta_{\min} T_{\min}) \quad (12)$$

with β the linear expansion coefficient which is also temperature dependent. Soma [Soma T. and Matsuo Kagaya H. (1987) RN=15706 pp. 33] derived an expression for β , namely

$$\beta = 3.725 \times 10^{-6} \left[1 - \exp(-5.88 \times 10^{-3} \{T - 124\}) \right] + 5.548 \times 10^{-10} T \quad \text{K}^{-1}. \quad (13)$$

This expression gives accurate values for the linear expansion coefficient between 120 K and 1500 K, but can also be applied for values of the temperature greater than 1500 K. Soma listed values for the expansion coefficient, for example a value of $4.612 \times 10^{-6} \text{ K}^{-1}$ at 1600 K, which is still in agreement with eq. (13). Due to insufficient knowledge about the expansion coefficient of molten silicon, the assumption is made that eq.(13) will still be valid after melting occurs.

5. The refractive index for silicon

5.1 The refractive index in the absence of photo-induced carriers

The treatment of the electric and magnetic fields is the same as in ch. 3 with the exception of the refractive index.

The refractive index of silicon is complex and is also temperature dependent. Marais [Marais T. K. *et al.* (1990) pp. 111-119] gave expressions for the reflectivity R at normal incidence and the absorption coefficient α_0 as

$$R = \begin{cases} 0.324 + 4 \times 10^{-5} T & T \leq 1000K \\ 0.584 - 4.5 \times 10^{-4} T + 2.6 \times 10^{-7} T^2 & 1000K < T \leq 1685K \\ 0.72 & T > 1685K \end{cases} \quad (14)$$

and

$$\alpha_0 = \begin{cases} 1340 \exp[T / 427] \text{ cm}^{-1} & T \leq 1685K \\ 1 \times 10^6 \text{ cm}^{-1} & T > 1685K \end{cases} \quad (15)$$

Since the reflection coefficient \tilde{r} for normal incidence is given by [Smith R. A. (1978) pp. 293]

$$\tilde{r} = \frac{1 - \tilde{n}}{1 + \tilde{n}} = \frac{1 - (n - ik)}{1 + (n - ik)}$$

and $R = |\tilde{r}|^2$, R becomes

$$R = \frac{(n-1)^2 + k^2}{(n+1)^2 + k^2}. \quad (16)$$

Solving for n from eq. (16) gives

$$n = \frac{(1+R) \pm \sqrt{(1+R)^2 - (1-R)^2(1+k)^2}}{(1-R)}. \quad (17)$$

Since $\alpha_0 = \frac{4\pi k}{\lambda}$, it follows that

$$k = \frac{\alpha_0 \lambda}{4\pi}. \quad (18)$$

For solid silicon the + sign gives values in good agreement with known listed values. Clearly n and k are also temperature dependent. The temperature was continuously varied over the LIPS-structure, with $T_{\min} \sim 300$ K in the valleys and a higher temperature T_{\max} at the top of the structure, resulting in a variation of the refractive index across the structure.

When the melting temperature (1685 K) of silicon is reached, the complex refractive index changes. Shvarev [Shvarev K. M. *et al.* (1975) pp. 2111-2112] measured the values of n and k and found them to be 3.13 and 5.56 respectively. If equation (17) is used with the + sign to calculate n and k from the given values of R and α_0 , the value of n is found to be much larger than 3.13. The - sign, however gives a value of $n = 3.64$ and a corresponding value of 5.52 for k . In the model constant values of 3.64 and 5.52 were used for molten silicon in agreement with the work of Wood [Wood R. F. *et al.* (1984) pp.113].

5.2 The refractive index with the effect of photo-induced carriers included

In the previous paragraph the effect of photo-induced carriers on the medium's conductivity was ignored. This effect can be included by employing the following expression for the refractive index [Smith R. A. (1978) pp. 292]

$$\tilde{N}^2 = \frac{\epsilon}{\epsilon_0} - \frac{i\sigma}{\omega\epsilon_0} \quad (19)$$

where

ϵ/ϵ_0 is the square of the complex refractive index considered in section 5.1,

$\omega=2\pi c/\lambda$, with c the velocity of light in vacuum and λ the wavelength of the probe laser light,

ϵ_0 is the permittivity in vacuum ($= 8.85418 \times 10^{-14}$ F/cm) and

σ is the photo-induced conductivity of the silicon (in $\Omega^{-1} \text{ cm}^{-1}$).

The conductivity for solid silicon is given by [Sze S. M. (1981) pp. 31]

$$\begin{aligned}\sigma &= q(n\mu_n + p\mu_p) \\ &= qn_{NEQ}(\mu_n + \mu_p)\end{aligned}\tag{20}$$

since the density of electrons (n) is approximately equal to the density of holes (p) and thus equal to the carrier density n_{NEQ} . q is the elementary charge ($= 1.60218 \times 10^{-19}$ C) and μ_n and μ_p are the mobilities of the electrons and holes respectively. Their temperature dependence are given by [Mole P. J. (1987) RN=15740 pp. 129-130, Mole P. J. (1987) RN=15742 pp. 130]

$$\mu_i = \mu_{0i} \left(\frac{T}{300} \right)^{-m_i} \quad i = n, p\tag{21}$$

with $\mu_{0n} = 1360 \text{ cm}^2/\text{Vs}$,

$$\mu_{0p} = 473 \text{ cm}^2/\text{Vs},$$

$$m_n \approx 2.0 \text{ and}$$

$$m_p \approx 2.2 .$$

The carrier density can be obtained from a rate equation describing the balance between the generation rate of photo-induced carriers and various recombination processes [Emel'yanov V. I. and Kashkarov P. K. (1972) pp. 161-166]

$$\frac{\partial n_{NEQ}(z)}{\partial t} + \frac{n_{NEQ}(z)}{\tau} + \gamma_A n_{NEQ}^3(z) - D\Delta n_{NEQ}(z) = \sigma |E|^2 \exp(-\alpha_0 z) \quad (22)$$

where τ is the time of the linear recombination,

α_0 is the absorption coefficient,

$$\sigma_A = \frac{(1-R)\alpha_0 c}{2\pi\hbar\omega},$$

γ_A is the Auger recombination coefficient,

E is the electric field vector amplitude of the incident laser wave, and

D is the ambipolar diffusion coefficient.

Emel'yanov discussed the carrier density for different limiting cases. In the quasistationary regime, when $\alpha_0 D, \gamma_A (n_{NEQ})^2 > \tau_p^{-1}$, the carrier density is described by

$$n_{NEQ} = \frac{\sigma_A |E|^2 \tau_s}{1 + \alpha_0 (D\tau_s)^{1/2}} \text{ cm}^{-3} \quad (23)$$

with τ_s the time of surface recombination

It is often of more practical use to write the expression for the carrier density in terms of the intensity I :

$$n_{NEQ} = \frac{(1-R)\alpha_0 \lambda \tau_s I}{hc [1 + \alpha_0 (D\tau_s)^{1/2}]} \text{ cm}^{-3}. \quad (24)$$

Smith [Smith R. A. (1978) pp. 195] gives an expression for the ambipolar diffusion coefficient, D , as

$$D = \frac{2D_n D_p}{D_n + D_p} \quad (25)$$

where

$$D_i = \left(\frac{kT}{q} \right) \mu_i \quad i = n, p$$

with k the Boltzmann constant ($= 1.38066 \times 10^{-23} \text{ J K}^{-1}$).

In this study only a qualitative estimate is made of the effect of the carrier density on the refractive index and therefore eq. (25) can be approximated as

$$n_{NEQ} = KI = \frac{KE}{\Delta t} \quad (26)$$

with E the energy of the laser wave and Δt the pulse width. By using the values for E , Δt and n_{NEQ} from Emel'yanov, the value of K is 2×10^{12} . By assuming the same value of K for silicon, values of n_{NEQ} for the computer model were estimated.

The real part of the refractive index calculated in this section does not differ much from that obtained in section 5.1, but the imaginary part is affected significantly by the presence of the photo-induced carriers for densities around 10^{19} - 10^{20} cm^{-3} . For example, for a temperature $T = 1650 \text{ K}$ section 5.1 gives a refractive index of $5.804 - 0.353i$, and section 5.2 gives it as $5.967 - 1.43i$.

None of the above expressions for the conductivity, mobilities and carrier density are valid for molten silicon ($T > 1685 \text{ K}$), since silicon becomes metallic upon melting [Galvin G. J. *et al.* (1983) pp. 1079-1087]. This means that one can assume that the carrier density becomes very large ($\sim 6.02 \times 10^{23}$). Also there is a very large decrease in the electrical

resistivity of the silicon, so that $\rho \sim 80 \mu\Omega \text{ cm}$ [Galvin G. J. *et al.* (1983) pp. 1079-1087].

The conductivity then becomes $1/80 \times 10^{-6} = 1.25 \times 10^4 \Omega^{-1} \text{ cm}^{-1}$.

6. Solution to the Stratton-Silver-Chu integral

In chapter 2 the integral was derived and is given by eq. (69):

$$\begin{aligned} I &= A \hat{k}^d \times \iint_s \left[\hat{n} \times \vec{E} - \eta \hat{k}^d \times (\hat{n} \times \vec{H}) \right] e^{i\Delta \vec{k} \cdot \vec{r}} dS \\ &= A \iint_s \{ \Gamma(s) \} e^{i\Delta \vec{k} \cdot \vec{r}} dS. \end{aligned} \quad (27)$$

Equation (27) can be summed over all indices:

$$I = A \sum_q \sum_p \sum_s \Gamma(s) e^{i\Delta \vec{k} \cdot \vec{r}} \Delta x \Delta y. \quad (28)$$

The position vector of an arbitrary point on the silicon surface is given by $\vec{r} = (x_s, 0, z_s)$, giving

$$\Delta \vec{k} \cdot \vec{r} = \Delta k_z z_s. \quad (29)$$

Substituting eq. (29) into (28) gives

$$\begin{aligned} I &= A \left(\sum_q \Delta y \right) \left(\sum_p \Delta x \right) \sum_s \Gamma(s) e^{i\Delta k_z z_s} \\ &= A \left(\sum_q \Delta y \right) \left(\sum_p \frac{\Lambda}{S_{\max}} \right) \sum_s \Gamma(s) e^{i\Delta k_z z_s}. \end{aligned} \quad (30)$$

The sum over Δy is just the width of the illuminated region in the Y-direction (see Fig. 4.1) and the sum over p the width in the X-direction divided by S_{\max} . Thus eq. (30) reduces to

$$I = A \frac{\xi}{S_{\max}} \sum_{s=1}^{S_{\max}} \Gamma(s) e^{i\Delta k_z z_s} \quad (31)$$

with ξ the area of the illuminated spot on the sample.

The Stratton-Silver-Chu integral is now solved for the LIPS-structures. As in the case for the moth-model it suffers from some drawbacks, which will be discussed in the chapter on results and discussions.

CHAPTER 5

MEASURING TECHNIQUES AND EQUIPMENT

In this chapter the experimental measuring techniques and equipment will be listed and discussed. The chapter is divided into two parts: Part A will concentrate on the optical properties of the moth, and Part B will cover the laser-induced periodic surface (LIPS) structures.

Part A:

Part A will discuss the experimental set-up, the equipment used and experimental procedures performed for the moth wing experiments. This will be done in sections 1 to 3. In section 4 the calculation of the total diffracted power from the wing will be discussed.

1. Experimental set-up

Fig. 5.1(b) shows a schematic layout of the experimental set-up and instrumentation used in the moth experiments. All the optical measurements were made with a 0.64 m grating monochromator equipped with a S-20 photomultiplier and with both slits set to 1 mm. This gave a resolution of about 1.5 nm, which is adequate, since the spectra do not show any sharp features. The moth wing was mounted with the line CC (see Fig. 5.1(a)) vertical on a calibrated turntable and could be rotated in a horizontal plane about the Y-axis, to provide different angles of incidence and diffraction, and also in a vertical plane about the Z-axis, to observe diffraction for different wing orientations at rotation angles ϕ . The

illumination source was a small tungsten lamp, operated at 12 V, which provided a collimated, polarized beam of white light, about 1.5 mm wide. The light diffracted from the wing was passed through a collecting lens and then focused by a 100 mm focal length lens onto the entrance slit of the monochromator.

Since the monochromator has different transmissions for vertically and horizontally polarized light, and since the moth wing can change the state of polarization of the light, a second polarizer was placed before the entrance slit of the monochromator to allow independent recordings of the two polarizations. Due to practical considerations the angle of incidence was restricted to values between 30 and 60 degrees. Since absolute calibration of the monochromator and photomultiplier response is difficult, only relative measurements were made.

2. Equipment

In this section the operation of the monochromator and photomultiplier used in the experiments will be discussed.

2.1 Monochromator

The monochromator used was an asymmetric Czerny-Turner system shown in Fig. 5.2(a). The incident light falls on a plane mirror which directs the light to the first concave mirror. This mirror collimates the light which is then incident on the grating. The diffracted light falls onto a second concave mirror, which in turn directs and focuses the light onto the exit slit. By rotating the grating, different wavelengths are scanned. A 1200 lines/mm grating together with two 0.64 m focal length concave mirrors were used.

The resolution of the monochromator is a measure of its ability to separate adjacent spectral lines. The resolution can be calculated in the following way:

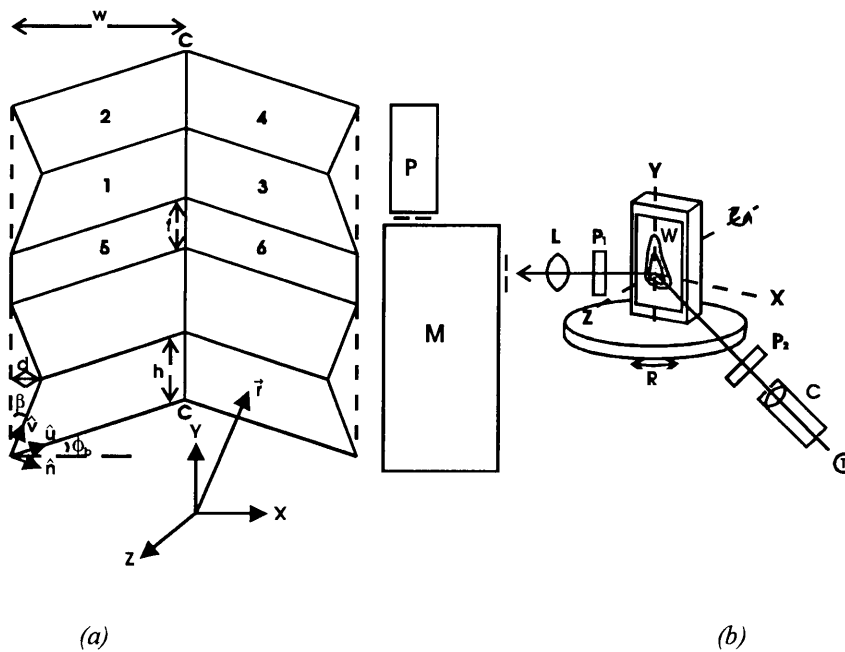


Fig. 5.1 (a) Schematic outline of the simplified diffraction structure. Line CC represents a valley between the raised ridges shown in chapter 3, Fig. 3.1(a). Distance d is the height of a micro rib above the plane of the wing scale in the Z-direction and h is the width of a micro rib along the Y-axis. If the depression of line CC is ignored, planes 5 and 6 would correspond to the plane of the wingscale. (b) Experimental layout showing the mounted wing (W) which can be rotated about the Y- and Z- axes, monochromator (M), photomultiplier (P), tungsten lamp (T), collimating telescope (C), polarizers (P_1 , P_2) and collecting lens (L).

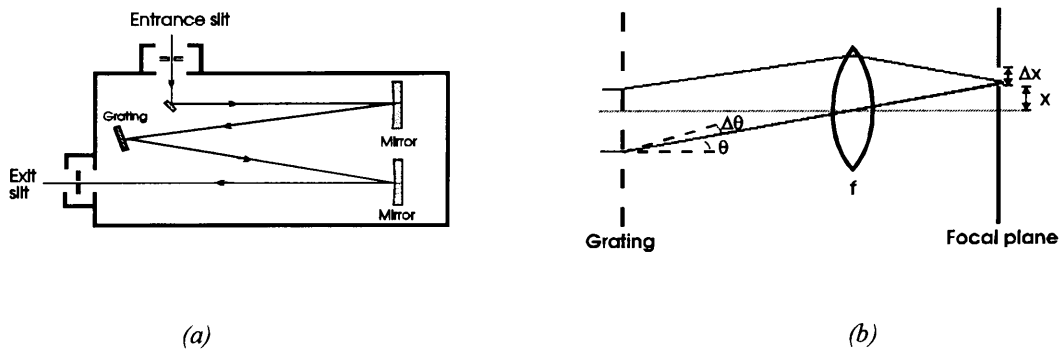


Fig. 5.2 (a) Schematic outline of a Czerny-Turner monochromator. Adapted from Pedrotti [Pedrotti F. L. and Pedrotti L. S. (1993) pp.362] (b) Schematic drawing showing the relationship between the angle of incidence, θ , the focal length of the mirrors and the slit width in the monochromator. The two mirrors are represented by a lens of the same focal length. Light leaving the grating at angle θ is focused at height x above the optical axis at the lower edge of the slit and light at $\theta + \Delta\theta$ will go to $x + \Delta x$, the upper edge of the slit.

Consider the grating equation in its simplest form:

$$\sin \theta = \frac{m\lambda}{d} \quad (1)$$

where m is the diffracted order of the light,

λ is the wavelength observed,

d is the distance between two grooves of the grating ($= 1/1200 = 0.833 \mu\text{m}$), and

θ is the angle of incidence on the grating.

Differentiating equation (1) gives

$$d\theta \cos \theta = \frac{m}{d} d\lambda \quad \text{or} \quad \Delta\lambda = \frac{d}{m} \cos \theta \Delta\theta. \quad (2)$$

$\Delta\theta$ can be expressed in terms of the focal length of the mirrors and the width of the exit slit. Consider a set-up as in Fig. 5.2(b). The mirrors can be represented by a lens with focal length 0.64 m. Simple geometry shows that $\theta = \frac{x}{f}$. Let the width of the slit be

given by Δx . Then θ can be changed by $\Delta\theta$ to cover the distance Δx . Therefore

$$\Delta\theta = \frac{\Delta x}{f}. \quad (3)$$

Substituting eq. (3) into (2) gives

$$\Delta\lambda = \frac{d}{m} \cos \theta \frac{\Delta x}{f}. \quad (4)$$

It then follows that

$$\Delta\lambda = \frac{\Delta x}{f} \sqrt{\frac{d^2}{m^2} - \lambda^2}. \quad (5)$$

Substituting values of $\Delta x = 1000 \mu\text{m}$, $f = 0.64 \times 10^6 \mu\text{m}$, $m = 1$ and $\lambda \approx 0.50 \mu\text{m}$ gives a resolution of $\Delta\lambda \approx 1.1 \text{ nm}$. A more exact calculation taking into account the oblique angle of incidence on the grating and the presence of two slits, yields a value of 1.5 nm .

2.2 Photomultiplier

The photomultiplier used was a S-20 with the cathode made of $\text{Na}_2\text{KSb-Cs}$ with a wide spectral coverage ($0.4 \mu\text{m} < \lambda < 0.9 \mu\text{m}$) and a low work function. Fig. 5.3 shows a schematic diagram of the photomultiplier. It is subdivided into a photocathode, an electron-optical input system, a secondary emission multiplier chain, and an anode.

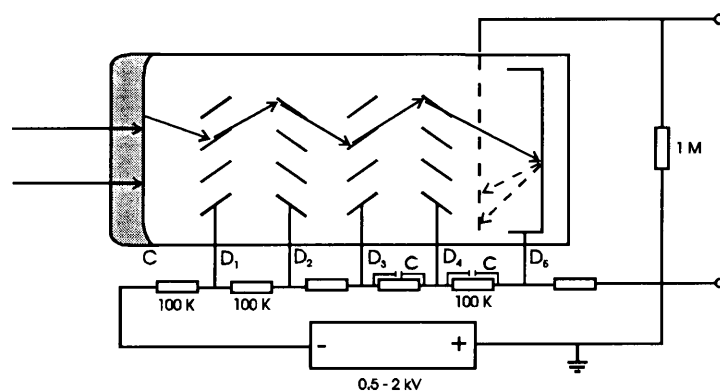


Fig. 5.3 Schematic outline of a photomultiplier.

Photons fall onto the photomultiplier's front part (cathode) and electrons are released. These electrons are guided to the first dynode of the secondary emission multiplier by means of the electron-optical input system. The electrons that fall on the first dynode release secondary electrons which are then accelerated to the next dynode, where they, in turn, release secondary electrons. A resistor chain is used to maintain a potential gradient between the dynode stages. The dynodes are usually made of CsSb , because of the material's good stability and high gain [EMI catalogue]. The last dynode is in the form of a shallow box and the anode mesh is stretched over it. The secondary electrons pass

through the mesh to strike the last dynode and the low energy secondary electrons produced are collected at the mesh.

Important parameters of the photomultiplier are as follows:

a. The Quantum efficiency $Q(\lambda)$

The quantum efficiency of the photocathode is the number of electrons emitted from the cathode per incident photon. For the S-20, $Q(\lambda_{\text{peak}}) \sim 0.22$.

b. Cathode current

The incident power P (Watt) contains $P/h\nu$ photons/sec and it will release $PQ(\lambda)/hc$ electrons/sec from the cathode. Therefore the cathode current will be

$$I_K = \frac{P\lambda eQ(\lambda)}{hc} \text{ Amps,}$$

where all symbols have their usual meaning.

c. Cathode sensitivity

The radiant cathode sensitivity is given by

$$E(\lambda) = \frac{I_K}{P} = \frac{\lambda eQ(\lambda)}{hc} \text{ AW}^{-1}.$$

The cathode sensitivity is usually quoted in units of $\mu\text{A/lumen}$ to remove the wavelength dependence.

f. Noise

The anode current is given by $I_A = GI_K$. This current shows considerable noise which limits the lowest signal that can be detected. Two kinds of noise can be distinguished, namely

- thermal or dark noise due to thermionic emission of electrons, and

- shot noise due to a statistical fluctuation in the output.

Thermal noise can be limited by reducing the cathode temperature. In this work this was accomplished by a Peltier cooler operating at $-25\text{ }^{\circ}\text{C}$. Shot noise is an inherent feature of the photon statistics on the cathode and cannot be eliminated. The noise produces a background signal which must be subtracted from the measured readings.

All measurements for the moth wing were made with a PM voltage of 1200 V, except where stated differently.

3. Experimental techniques

In this section the experimental procedures for the different measurements will be discussed. The procedures listed include the measurement of the angular spread of light scattered by the wing, and the influence of the wing orientation and the wavelength on the diffraction efficiency of the wing.

3.1 Procedure to measure the angular spread of light scattered by the wing

The moth wing resembles a metallic film which follows the law of reflection and therefore reflects light specularly. This was investigated by using the following procedure:

- Set the monochromator to read a wavelength of 550 nm.
- The angle between the incident beam and observation direction is fixed to 120° . It is done by replacing the wing with a quartz plate with a matted second surface. The collimating telescope (C in Fig. 5.1(b)) is fixed at the desired angle of 120° . The table on which the wing/quartz plate is mounted is then rotated so that the reflection falls on

the entrance slit of the monochromator. The quartz plate is then replaced with the wing. Note that the tungsten light source and the polarizer (P2) nearest to the collimating telescope is attached to the telescope and therefore all three are rotated as a unit.

- Set polarizer P2 for vertical (S-) polarization.
- Change the setting of the polarizer (P1) nearest to the monochromator to vertical (S-) polarization.
- Optimise the position of the collecting lens (L).
- Rotate the wing about the Y-axis to change the angles of incidence (θ_i) and diffraction (θ_d). For only one position is the reflection condition ($\theta_i = \theta_d = 60^\circ$) satisfied and any rotation from this increases (decreases) θ_i and decreases (increases) θ_d .
- Change the settings of polarizers P1 to horizontal (P-) polarization and repeat the measurements. However, DO NOT optimise the collecting lens again, otherwise the two sets of measurements cannot be compared. The reason for this will be explained in section 4.

3.2 Procedure to measure the effect of wing orientation on diffraction efficiency

The intensity of diffracted light depends strongly on the angle of incidence and the orientation of the wing in its own plane. The following procedure was used for the measurements:

- Set the monochromator to read a wavelength of 550 nm.
- Replace the wing with a quartz plate with a matted second surface. Move the collimating telescope (C in Fig. 5.1(b)) so that the angle of incidence is 30° , i.e. the

angle between the incident beam and observation direction is 60° . Rotate the table on which the wing/quartz plate is mounted so that the reflection falls on the entrance slit of the monochromator. Replace the quartz plate with the wing.

- Set polarizers P1 and P2 to vertical (S-) polarization.
- Optimise the position of the collecting lens (L).
- Rotate the wing in steps of 15° about the Z-axis from -90° to 90° .
- Repeat the above for angles of incidence of 45° and 60° .
- Change the setting of polarizer P2 to horizontally (P-) polarization and repeat the procedure. However, DO NOT optimise again, otherwise the two sets of measurements cannot be compared. The reason for this will be explained in section 4.

3.3 Procedure to measure the spectral distribution of light scattered from the wing

The spectral distribution from 400 nm to 900 nm was measured in the following way:

- The angle of incidence is fixed to 60° in the same way as has been described in section 3.1.
- Set polarizers P1 and P2 to vertical (S-) polarization.
- Optimise the set-up with the collecting lens (L).
- Set the wing so that line CC is vertical, i.e. the rotation angle is 0° .

- Scan the wavelengths between 400 nm and 900 nm with the monochromator in steps of 25 nm. At each step take readings with polarizer P1 set for S- and P-polarization respectively.
- Change the rotation angle of the wing to -30° , -60° and -90° respectively and repeat the measurements.
- Change the setting of polarizer P2 to horizontally (P-) polarization and repeat the procedure without optimising again.

It is important to note that for wavelengths of 800 nm and greater a filter must be used to prevent second and higher order diffraction lines from passing through the monochromator. An OG53 yellow-orange filter was used for this purpose.

4. Calculation of the total power diffracted from the wing

It is known that the polarization state of a beam incident on a diffraction grating is not maintained if the grating is tilted in its own plane. The same is also true for the wing. Consequently, the total diffracted power can only be obtained by recording both the horizontally and the vertically polarized diffracted components independently. These two sets of measurements are then added to obtain the total diffracted power. This can be explained in term of Jones matrices. Note that the case where one starts off with S-polarization will be discussed here. The case for P-polarization is similar.

The electric field for incoming S-polarized light is given by:

$$\vec{E}_0 = \begin{bmatrix} 0 \\ E_0 \end{bmatrix}.$$

The moth is represented with a matrix:

$$\overline{\overline{M}}_1 = \begin{bmatrix} \tilde{a} & \tilde{b} \\ \tilde{c} & \tilde{d} \end{bmatrix},$$

where the tildes indicates that the matrix elements can be complex.

After reflection from the moth wing, the electric field is given by

$$\vec{E}_1 = \overline{\overline{M}}_1 \vec{E}_0 = \begin{bmatrix} \tilde{a} & \tilde{b} \\ \tilde{c} & \tilde{d} \end{bmatrix} \begin{bmatrix} 0 \\ E_0 \end{bmatrix} = \begin{bmatrix} \tilde{b} E_0 \\ \tilde{d} E_0 \end{bmatrix} = \begin{bmatrix} E_{x1} e^{i\phi_x} \\ E_{y1} e^{i\phi_y} \end{bmatrix}.$$

The total diffracted intensity is then

$$I_1 = \vec{E}_1^+ \vec{E}_1 = \begin{bmatrix} E_{x1} e^{i\phi_x} & E_{y1} e^{i\phi_y} \end{bmatrix} \cdot \begin{bmatrix} E_{x1} e^{i\phi_x} \\ E_{y1} e^{i\phi_y} \end{bmatrix} = E_{x1}^2 + E_{y1}^2. \quad (6)$$

The diffraction efficiency is therefore given as

$$\eta \equiv \frac{I_1}{I_0} = \frac{E_{x1}^2 + E_{y1}^2}{E_0^2},$$

with I_0 the intensity of the incoming light.

A slightly different quantity is, however, measured. \vec{E}_1 is first passed through polarizer P1 described by:

$$\overline{\overline{P}}_1 = \begin{bmatrix} 0 & 0 \\ 0 & \eta_t \end{bmatrix},$$

where η_t represents the transmission of the polarizer, which is set for S-polarization. The monochromator is described by a diagonal matrix

$$\overline{\overline{M}}_2 = \begin{bmatrix} \eta_p & 0 \\ 0 & \eta_s \end{bmatrix}.$$

The monochromator can be described by a diagonal matrix, since the incoming S- and P-polarized light are eigenfunctions of the operator describing the monochromator, and since the grooves of the grating are vertical.

The electric field on the output side of the monochromator is therefore

$$\vec{E}_2 = \overline{\overline{M_2 P_1}} \vec{E}_1 = \overline{\overline{M_2}} \begin{bmatrix} 0 \\ \eta_t E_{y1} e^{i\phi_y} \end{bmatrix} = \begin{bmatrix} 0 \\ \eta_s \eta_t E_{y1} e^{i\phi_y} \end{bmatrix}.$$

Finally, the intensity detected by the photomultiplier is then

$$I_s = \eta_m \eta_s^2 \eta_t^2 E_{y1}^2,$$

with η_m the sensitivity of the photomultiplier.

For polarizer P1 set for P-polarization:

$$\overline{\overline{P_1'}} = \begin{bmatrix} \eta_t & 0 \\ 0 & 0 \end{bmatrix}$$

and the output electric field is then

$$\vec{E}'_2 = \overline{\overline{M_2 P_1'}} \vec{E}_1 = \overline{\overline{M_2}} \begin{bmatrix} \eta_t E_{x1} e^{i\phi_x} \\ 0 \end{bmatrix} = \begin{bmatrix} \eta_p \eta_t E_{x1} e^{i\phi_x} \\ 0 \end{bmatrix},$$

with the intensity seen by the photomultiplier given by

$$I_p = \eta_m \eta_p^2 \eta_t^2 E_{x1}^2.$$

Use a correction factor $f = \frac{\eta_s^2}{\eta_p^2}$ and define the total diffracted intensity as:

$$\begin{aligned} I_{Tot} &= I_s + f I_p = \frac{\eta_s^2}{\eta_p^2} \eta_m \eta_t^2 \eta_p^2 E_{x1}^2 + \eta_m \eta_t^2 \eta_s^2 E_{y1}^2 \\ &= \eta_m \eta_t^2 \eta_s^2 (E_{x1}^2 + E_{y1}^2). \end{aligned}$$

It is evident that I_{Tot} is the same as I_1 except for a constant factor and it can thus be used to obtain relative measurements.

The correction factor f is wavelength dependent and can be measured experimentally by using the following procedure:

- Remove the moth wing and position the collimating telescope so that the light falls directly onto the entrance slit of the monochromator. To prevent the photomultiplier from saturating, a PM voltage of 600 V is used.
- Set the monochromator reading for a wavelength of 400 nm.
- Set polarizer P1 for S-polarization (vertical position or 0° rotation angle) and rotate polarizer P2 until a maximum reading is reached.
- Repeat this for P1 changed to P-polarization (horizontal position, or both -90° and 90° rotation angles).
- Repeat this procedure for wavelengths 400 nm to 850 nm in 25 nm steps.
- Remember that for wavelengths of 800 nm and greater the OG53 filter must be used.

In this case the two recorded intensities are:

$$I_s'' = |E_0 \eta_s \eta_t|^2 \eta_m$$

$$I_p'' = |E_0 \eta_p \eta_t|^2 \eta_m$$

The required correction factor is now given by

$$f = \frac{I_s}{I_p} = \left| \frac{\eta_s}{\eta_p} \right|^2$$

In this procedure the phase relationship between the two components is not measurable, but this does not influence the determination of the main parameters such as total diffraction efficiency.

The results of the measurements will be discussed in the chapter on results and discussions.

Part B:

In part B the measuring techniques and equipment used for the LIPS-experiments will be discussed. Section 1 to 3 will cover the experimental set-up, apparatus used and experimental procedures followed, while section 4 will cover some calculations done for the calibration of the ellipsometer and the calculation of the refractive index and oxide thicknesses.

1. Experimental set-up

Fig. 5.4 shows a schematic layout of the experimental set-up and instrumentation used in the LIPS-experiments. A Gaertner model L119 ellipsometer combined with a 3 mW He-Ne laser and an EMI 6094 photomultiplier were used to observe polarization effects on polished single crystal Si and GaAs samples. The energy of the pulsed ruby laser was measured with a Scientech Mentor MA10 energy meter, by illuminating it with part of the laser beam. Blocking filters were used in the photomultiplier to reduce the background and scattered laser light. The photomultiplier pulse was recorded on a Tektronix storage oscilloscope, which was triggered from a fast photo diode illuminated by part of the ruby laser beam.

The He-Ne probe laser was placed 3.43 m from the ellipsometer. It was focused with a 0.55 m focal lens placed 0.68 m from the entrance aperture of the ellipsometer. Inside the ellipsometer itself is a 0.25 m collimating lens, and the combination of the two lenses produced a gaussian spot with a 1 mm waist diameter on the sample.

P-type ($\sim 11.2 \Omega \text{ cm}$) (111)-orientated and n-type ($1\text{-}2 \Omega \text{ cm}$) (111)-orientated single-crystal Si disks and a n-type single-crystal GaAs disk were used for the experimental work. The GaAs was doped with Si ($N_D > 10^{18} \text{ cm}^{-3}$). The samples were mounted in the ellipsometer in such a way that the probe beam hit the surface at an angle of incidence of

70° and the beam of the pulsed ruby laser struck the same spot on the surface close to normal incidence.

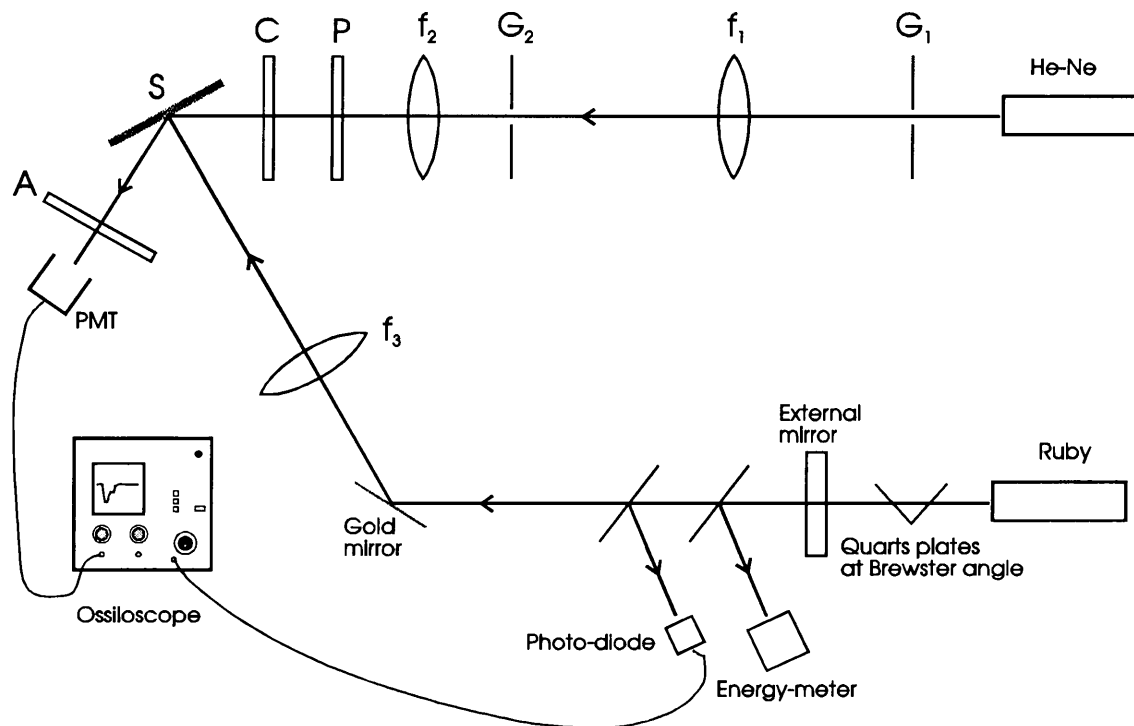


Fig. 5.4 Schematic layout of the LIPS-experiment. The layout shows the He-Ne laser, an aperture (G_1), focal lenses (f_1 , f_3), ellipsometer, photomultiplier (PMT), the ruby laser, quartz plates and gold mirror. The ellipsometer consists of an entrance aperture (G_2), a collimating lens (f_2), a polarizer (P), compensator (C), sample (S) and analyser (A).

A pulsed ruby laser with a pulse width (FWHM) of 40 ns and a rise time (10-90%) of 5 ns at a wavelength of 694.3 nm, was used to irradiate the samples in the ellipsometer. The ruby laser provided multimode transverse mode pulses of energies of ~ 150 mJ, but the temporal and spatial profile of the beam was smooth, so that no “hot spots” formed on the illuminated area. The output beam was linearly polarized and was focused onto the sample by a 0.3 m focal lens. For the silicon samples the lens was placed 0.27 m from the sample and this produced a spot with a diameter of 2 mm on the sample. When the same lens distance was used for the GaAs sample, the GaAs was damaged when irradiated with the ruby laser. The lens was then placed 0.192 m from the sample and this produced a spot with diameter of 3 mm on the sample. This produced energy densities of 3.5 and 1.6 Jcm⁻² for the silicon and GaAs experiments respectively.

2. Equipment

In this section the equipment used in the experiments will be discussed. This includes the oscilloscope, ellipsometer, photo diode and ruby laser. The photomultiplier has been discussed in part A, section 2.2.

2.1 The oscilloscope and photomultiplier

An EMI 6094 photomultiplier together with a Tektronix storage oscilloscope model no. 7633 were used to record the amount of light reflected from the sample surface after passing through the analyser of the ellipsometer.

The EMI 6094 photomultiplier is an eleven stage (S-11) photomultiplier and has a quantum efficiency of $Q(\lambda) \sim 0.008$ at a wavelength of 632.8 nm [EMI catalogue] and a risetime of about 4 ns. The response time of the combination, oscilloscope and photomultiplier, is then calculated in the following way:

The oscilloscope has a bandwidth of $\Delta\nu = 3 \times 10^8$ Hz and thus a period of $1/(3 \times 10^8) = 3$ ns. The risetime (10 - 90 %) of the oscilloscope is approximatedly a third of its period and is therefore $\tau_{osc} \sim 1$ ns.

The risetime of the combination is then given by

$$\tau_{Tot} = \sqrt{\tau_{PMT}^2 + \tau_{osc}^2} = 4.1 \text{ ns.}$$

This was confirmed experimentally:

- Connect the photomultiplier to the oscilloscope and set the oscilloscope timing to the smallest setting.
- Set the oscilloscope on auto-trigger and record a pulse.

- Read the risetime of the pulse. This gave $\tau_{Tot} = 4$ ns.

This is in good agreement with the calculated value. Thus the response time is considerably shorter than the laser pulse width and reliable recordings can be expected.

All the experiments were done with a photomultiplier voltage of 1800 V.

2.2 The photo diode

A pin silicon photo diode (MRD 721) was used to trigger the oscilloscope, by illuminating it with part of the ruby laser beam. It has an ultra fast response (< 1.0 ns Typ) and a relative spectral response of about 83% at 694.3 nm [Motorola Semiconductor catalogue (1982)].

2.3 The ellipsometer

All the experiments were done using a Gaertner model L119 ellipsometer. Azzam [Azzam R. M. A. and Bashara N. M (1989) chapter 3] performed an extensive study of the operation and theory of the ellipsometer and provide a detailed mathematical description. In the first part of this section a short description will be given of the principles of the ellipsometer and in the second part the expression for the ellipsometer transmission will be derived.

2.3.1 Principles of the ellipsometer

Consider a surface with plane polarized light incident on it at 45° as in Fig. 5.5(a). The incident electric field has S- and P-polarization components as in Fig. 5.5(a). These two components are not reflected at the same depth in the sample and this causes a phase-shift between them. The result is elliptically polarized light.

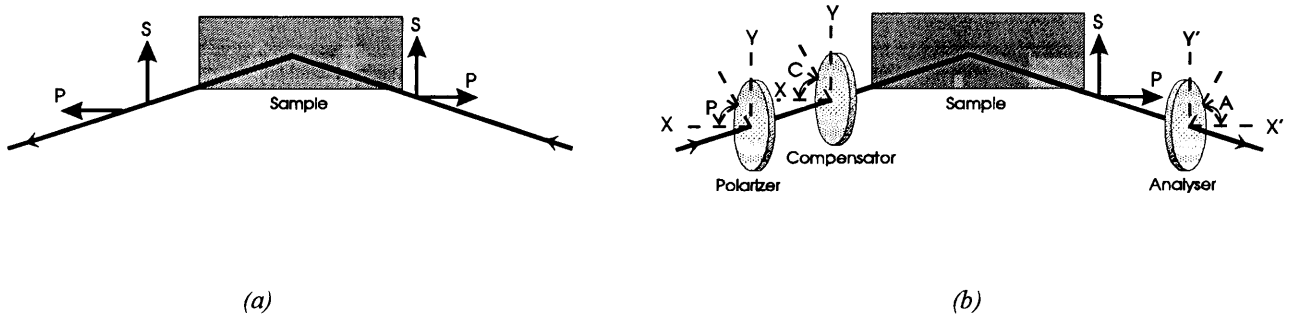


Fig. 5.5 (a) Schematic drawing showing a surface with plane polarized light incident on it. After reflection from the sample, the light is elliptically polarized. (b) A schematic layout of the ellipsometer.

In the ellipsometer this process is turned around (see Fig. 5.5(b)). A quarter wave plate is placed in the path of the incident light to make it elliptically polarized in such a way that it will be plane polarized after reflection from the sample. By using a second polarizer - called the analyser - to block this light, the direction of polarization of the light can be determined.

2.3.2 The ellipsometer transmission

The ellipsometer transmission is given by

$$T = GLL^*$$

G is a proportionality constant that is best determined experimentally. The expression for L is calculated by using Jones vectors and matrices for the incident light and ellipsometer components.

Consider again Fig. 5.5(b). The polarizer has transmit (t) and extinguish (e) axes with the transmit axis at angle P to the x -axis. The compensator is a $\lambda/4$ -plate which has fast (f) and slow (s) axes with the fast axis at an angle C to the x -axis. Lastly, the analyser also has t and e axes with t at an angle A to the x' -axis.

Start at the output side of the polarizer (P):

$$\vec{E}_{Po}^{te} = a_P \begin{bmatrix} 1 \\ 0 \end{bmatrix}$$

where the superscript denotes the co-ordinate system used, the first subscript denotes the ellipsometer component referred to and the second subscript is either an i or an o , depending on whether the observer is at the input or output side of the component.

At the input side of the compensator (C) a rotation through the angle $-(P-C)$ must be performed to change from the te to the fs system:

$$\begin{aligned} \vec{E}_{Ci}^{fs} &= R(-(P-C))\vec{E}_{Po}^{te} \\ &= a_P \begin{bmatrix} \cos(P-C) & -\sin(P-C) \\ \sin(P-C) & \cos(P-C) \end{bmatrix} \begin{bmatrix} 1 \\ 0 \end{bmatrix} \\ &= a_P \begin{bmatrix} \cos(P-45^\circ) \\ \sin(P-45^\circ) \end{bmatrix} \end{aligned}$$

since $C = 45^\circ$. In the fs system the Jones matrix for the compensator is given by:

$$T_C = a_C \begin{bmatrix} 1 & 0 \\ 0 & e^{-i\delta_c} \end{bmatrix} = a_C \begin{bmatrix} 1 & 0 \\ 0 & e^{-i\frac{\pi}{2}} \end{bmatrix} = a_C \begin{bmatrix} 1 & 0 \\ 0 & -1 \end{bmatrix}.$$

Therefore at the output side of C :

$$\vec{E}_{Co}^{fs} = a_P a_C \begin{bmatrix} 1 & 0 \\ 0 & -1 \end{bmatrix} \begin{bmatrix} \cos(P-45^\circ) \\ \sin(P-45^\circ) \end{bmatrix} = a_P a_C \begin{bmatrix} \cos(P-45^\circ) \\ -\sin(P-45^\circ) \end{bmatrix}.$$

To compute the influence of reflection from the sample, a rotation of the axes through an angle of $-C = -45^\circ$ must be performed to change to the xy (or ps) system. Therefore

$$\begin{aligned} \vec{E}_{Si}^{ps} &= R(-45^\circ)\vec{E}_{Co}^{fs} \\ &= a_P a_C \begin{bmatrix} \cos 45^\circ & -\sin 45^\circ \\ \sin 45^\circ & \cos 45^\circ \end{bmatrix} \begin{bmatrix} \cos(P-45^\circ) \\ \sin(P-45^\circ) \end{bmatrix} \\ &= \frac{a_P a_C}{\sqrt{2}} \begin{bmatrix} \cos(P-45^\circ) + \sin(P-45^\circ) \\ \cos(P-45^\circ) - \sin(P-45^\circ) \end{bmatrix}. \end{aligned}$$

After reflection from the sample,

$$\vec{E}_{So}^{ps} = \begin{bmatrix} \tilde{r}_p & 0 \\ 0 & \tilde{r}_s \end{bmatrix} \vec{E}_{Si}^{ps} = \frac{a_p a_c}{\sqrt{2}} \begin{bmatrix} \tilde{r}_p \{ \cos(P - 45^\circ) + \sin(P - 45^\circ) \} \\ \tilde{r}_s \{ \cos(P - 45^\circ) - \sin(P - 45^\circ) \} \end{bmatrix}.$$

At the input of the analyser (A), rotate the axes through an angle A :

$$\begin{aligned} \vec{E}_{Ai}^{te} &= \frac{a_p a_c}{\sqrt{2}} \begin{bmatrix} \cos A & \sin A \\ -\sin A & \cos A \end{bmatrix} \begin{bmatrix} \tilde{r}_p \{ \cos(P - 45^\circ) + \sin(P - 45^\circ) \} \\ \tilde{r}_s \{ \cos(P - 45^\circ) - \sin(P - 45^\circ) \} \end{bmatrix} \\ &= \frac{a_p a_c}{\sqrt{2}} \begin{bmatrix} \tilde{r}_p \cos A \{ \cos(P - 45^\circ) + \sin(P - 45^\circ) \} + \tilde{r}_s \sin A \{ \cos(P - 45^\circ) - \sin(P - 45^\circ) \} \\ -\tilde{r}_p \sin A \{ \cos(P - 45^\circ) + \sin(P - 45^\circ) \} + \tilde{r}_s \cos A \{ \cos(P - 45^\circ) - \sin(P - 45^\circ) \} \end{bmatrix} \end{aligned}$$

At the analyser output,

$$\begin{aligned} \vec{E}_{Ao}^{te} &= \frac{a_p a_c a_A}{\sqrt{2}} \begin{bmatrix} 1 & 0 \\ 0 & 0 \end{bmatrix} \times \\ &\begin{bmatrix} \tilde{r}_p \cos A \{ \cos(P - 45^\circ) + \sin(P - 45^\circ) \} + \tilde{r}_s \sin A \{ \cos(P - 45^\circ) - \sin(P - 45^\circ) \} \\ -\tilde{r}_p \sin A \{ \cos(P - 45^\circ) + \sin(P - 45^\circ) \} + \tilde{r}_s \cos A \{ \cos(P - 45^\circ) - \sin(P - 45^\circ) \} \end{bmatrix} \\ &= \frac{a_T}{\sqrt{2}} \begin{bmatrix} \tilde{r}_p \cos A \{ \cos(P - 45^\circ) + \sin(P - 45^\circ) \} + \tilde{r}_s \sin A \{ \cos(P - 45^\circ) - \sin(P - 45^\circ) \} \\ 0 \end{bmatrix} \\ &= a_T \begin{bmatrix} L \\ 0 \end{bmatrix} \end{aligned}$$

Therefore, the light intensity transmitted through the whole system is the ellipsometer transmission

$$T = GLL^*,$$

where $G = (a_p a_c a_A)^2$ and

$$\begin{aligned} L &= \frac{\tilde{r}_p \cos A}{\sqrt{2}} \{ \cos(P - 45^\circ) + \sin(P - 45^\circ) \} \\ &\quad + \frac{\tilde{r}_s \sin A}{\sqrt{2}} \{ \cos(P - 45^\circ) - \sin(P - 45^\circ) \} \end{aligned}$$

This expression will be used in section 4.3 to calculate the transmission needed for the calibration. It is also used in the mathematical model described in chapter 4.

2.4 The ruby laser

A TRG Model 104 Q-switched pulsed ruby laser was used for the experimental work. The laser has a 7.3 cm long \times 1 cm diameter ruby rod excited by a xenon flashlamp. The one laser mirror is a high speed (30 000 RPM) rotating prism used for Q-switching, while the other is the output mirror, which has an 8 m radius of curvature. The laser requires an 1000 J input to produce a 150 mJ output. It operates at room temperature and is air cooled.

Since the ends of the laser rod are cut perpendicular to the axis and not at Brewster's angle, the laser light is not polarized. The formation of the LIPS-structures requires a horizontal polarization. This was achieved by placing two quartz plates, set at the Brewster angle, inside the cavity (see Fig. 5.4). This required the output mirror to be moved to enlarge the cavity.

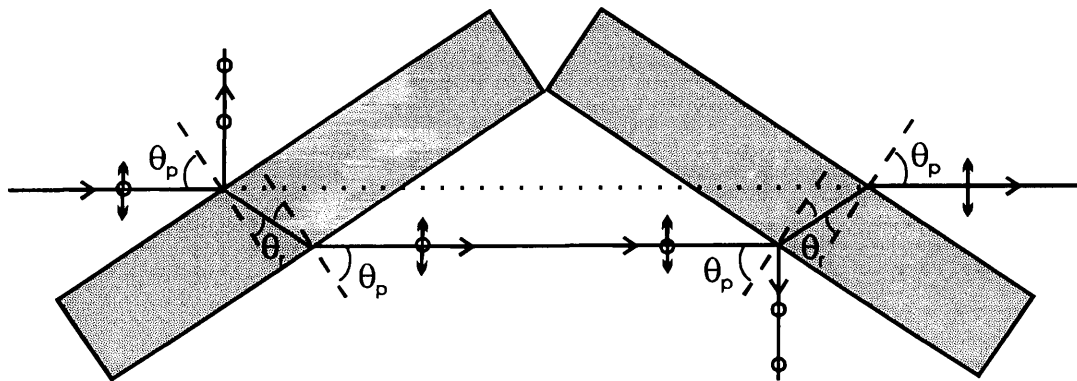


Fig. 5.6 Illustration of a Brewster window. θ_p is the Brewster angle.

The polarization of the laser in this way is based on the principle of a Brewster window. When unpolarized light is incident on the quartz plate set at the Brewster angle ($= 56.3^\circ$), the electric field's vertical component is partially reflected off the surface and the horizontal component is transmitted without loss. This is shown in Fig. 5.6. However,

since the quartz has a larger refractive index than air, the light beam is displaced after exiting the medium. This will complicate the alignment procedure for the laser mirrors and therefore a second quartz plate, also set at the Brewster angle, is used to cancel the displacement. Another reason for the use of the second plate is that it provides more surfaces from which the unwanted polarization can be reflected and thus introducing more losses to the vertical polarization.

Experimental measurements showed that the laser was now polarized horizontally, with a 20:1 ratio.

3. Experimental techniques

In this section the procedures for setting up the equipment, calibration and experimental work will be described and discussed.

3.1 Alignment of the He-Ne system

3.1.1 Alignment of the He-Ne beam from the laser to the entrance aperture of the ellipsometer

This procedure describes the alignment of the probe beam from the laser to the entrance aperture of the ellipsometer. The ellipsometer telescopes must already be aligned correctly. The procedure is as follows:

(Please refer to Fig. 5.4)

- Remove the aperture G_1 and focal lens f_1 .
- Steer the beam with the mirrors (M_1 and M_2) until the beam is aligned through the ellipsometer entrance aperture (G_2) and through the centre of the $\lambda/4$ -compensator (C).

- Replace the focal lens f_1 . It is important that the beam passes through the centre of the lens, otherwise the beam will be deviated. The lens should also be perpendicular to the beam direction.
- Optionally, aperture G_1 can now be replaced. The aperture only serves as reference for re-alignment that may be necessary later on.

3.1.2 Calibration of the analyser and polarizer circles and the $\lambda/4$ -compensator

The analyser and polarizer circles have to be calibrated to compensate for an offset of the actual 0° setting.

The analyser circle is calibrated as follows:

- Place a quartz plate in the sample holder. The quartz plate must be matted on its back-surface to prevent additional reflections.
- Open the ellipsometer entrance aperture (G_2) and rotate the ellipsometer table until the reflection from the quartz plate retraces the incoming beam. If necessary, adjust the sample holder by tilting it until the reflection is correct.
- Rotate the table through $180^\circ - \theta_B$ and fasten. θ_B is the Brewster angle and for quartz this angle is 55.54° .
- Rotate the telescope until the ellipsometer table is set to θ_B . It is important to confirm that the He-Ne beam passes through the centre of the analyser circle.
- Set the analyser circle for zero transmission. This is the analyser zero setting. Refer to this setting as δA . To find the correct analyser angle, A , δA must be subtracted from the reading, A_{reading} . Therefore $A = A_{\text{reading}} - \delta A$.

The procedure for the calibration of the polarizer circle is as follows:

- Remove the quartz plate and rotate the analyser telescope so that the He-Ne beam passes straight through the ellipsometer. Set the ellipsometer table on 180° and fasten.
- Remove the $\lambda/4$ -compensator and set the polarizer for zero transmission of the beam. This is the 90° setting of the polarizer. For this setting, P_{setting} , on the circle, let $\delta P = P_{\text{setting}} - 90^\circ$. The polarizer reading, P , will then be $P = P_{\text{reading}} - \delta P$.

The compensator is calibrated in the following way:

- Cross the polarizer and analyser circles with $P \sim +45^\circ$ and $A \sim -45^\circ$.
- Replace the $\lambda/4$ -compensator and set it at $\sim +45^\circ$ with the fast axis.
- Confirm that the He-Ne beam is extinguished and fasten the compensator.

The ellipsometer is now calibrated. The calibration can be fine-tuned by repeating these calibration procedures.

3.1.3 Sample alignment

The sample is aligned to ensure that the beam travels along the optical axis through the ellipsometer. It is done as follows:

- Place a quartz plate in the sample holder. The quartz plate must be matted on its back-surface to prevent additional reflections.
- Open the ellipsometer entrance aperture (G_2) and rotate the ellipsometer table until the reflection from the quartz plate retraces the incoming beam. If necessary, adjust the sample holder by tilting it until the reflection retraces the incoming beam path. Note that the sample holder rests on the sample table, which in turn rests on top of the ellipsometer table. The sample table can be rotated independently from the ellipsometer table.

- Turn the ellipsometer table until it reads 180° and fasten it. Loosen the sample table from the ellipsometer table, rotate it so that the reflection again retraces the path of the incoming beam and fasten it. The sample table and ellipsometer table will now move as a unit.
- Rotate the ellipsometer table to read $180^\circ - 70^\circ = 110^\circ$ and fasten it.
- Adjust the analyser telescope until the reflection passes through the centre of the telescope. Fasten the telescope.

3.2 Alignment of the ruby laser beam

A second He-Ne laser is needed to align the set-up from the ruby laser to the sample. The He-Ne is placed as in Fig. 5.7, so that its reflection from the ruby rod can be used for the alignment.

3.2.1 Alignment of the He-Ne beam with the ruby beam

In order to ensure that the ruby will, after completion of the alignment procedure, strike the sample on the same spot as the probe beam, it is necessary to let the ruby beam coincide with the alignment He-Ne beam.

- Adjust the gold mirror (M_1) and the glass plate (Q_3) until the He-Ne spot falls on the centre of the ruby rod.
- Place an aperture in the beam path and adjust M_1 , Q_3 , the ruby laser direction and the aperture until the reflection from the ruby rod centres on the aperture.
- Remove the gold mirror (M_2) and place a piece of blackened photographic paper as far away as possible in the path of the beam. Fire the ruby laser once and confirm that the

damage spot coincides with the He-Ne spot. If they do not coincide, adjust the He-Ne beam with mirror M_1 until they do.

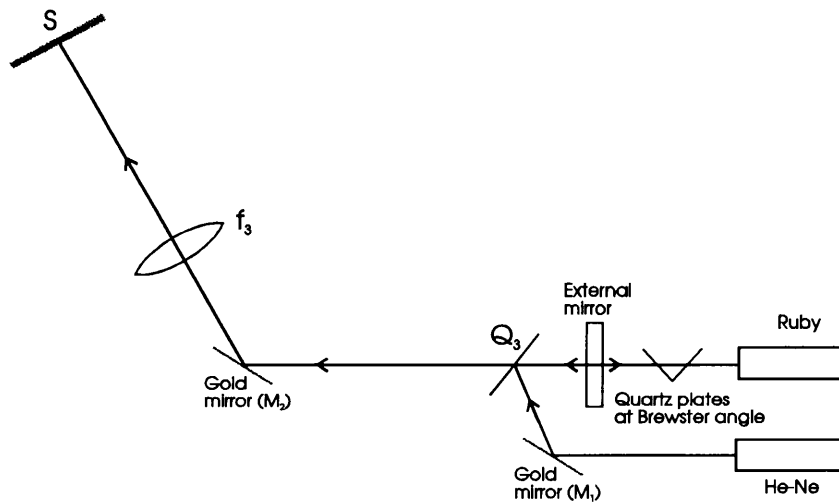


Fig. 5.7 Alignment set-up for the ruby laser system. The set-up shows the ruby and He-Ne lasers, the quartz plates, gold mirrors (M_1 and M_2), a quartz plate (Q_3), focal lens (f_3) and sample (S).

3.2.2 Procedure to align the ruby spot with the probe beam spot on the sample

- Replace the mirror M_2 and adjust it until the two He-Ne spots (from the probe and alignment lasers) coincide on the sample. To ensure that the ruby beam is normally incident on the sample, place an aperture between the mirror M_2 and the sample and adjust M_2 and the aperture until the reflection from the sample retraces the beam path.
- The beam is then focused with the focusing lens (L_1).
- Do the photographic paper test again to confirm coincidence of the two spots on the sample.

The entire set-up is now aligned. The refractive index and the oxide layer thickness of the samples can now be determined and the LIPS-experiments performed.

The same experiment was performed for Si and GaAs. The required sample was placed in the sample holder and the ellipsometer set for zero transmission of the probe beam. The ruby was then fired six times and the signal due to the change in polarization of the probe beam recorded on the oscilloscope.

3.3 Calibration of the ellipsometer transmission

The experimental and theoretical results can only be compared if the ellipsometer transmission for all the recorded signals is known. It is thus necessary to calibrate the ellipsometer for transmission. The experimental set-up is shown in Fig. 5.8.

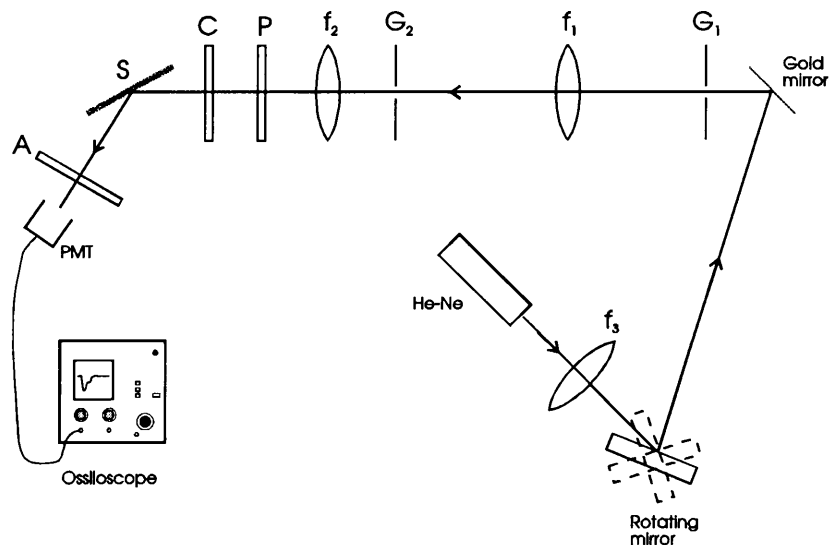


Fig. 5.8 The experimental set-up for the calibration of the ellipsometer transmission. The symbols have the same meaning as in Fig. 5.4.

Since the LIPS-experiment described in section 1 was performed with a pulsed ruby laser, it is preferable to perform the calibration experiment also with a similar pulsed laser. The He-Ne was focused with a 1m focal lens (f_3) onto a rotating mirror that sweeps the beam across the slit aperture G_2 repeatedly. The rotating mirror was placed about 6.15 m from the ellipsometer entrance aperture (G_2) and rotated at a maximum speed of 5220 RPM. The rest of the set-up is the same as for the LIPS-experiment. This produced a beam of about 2 μ s pulse width.

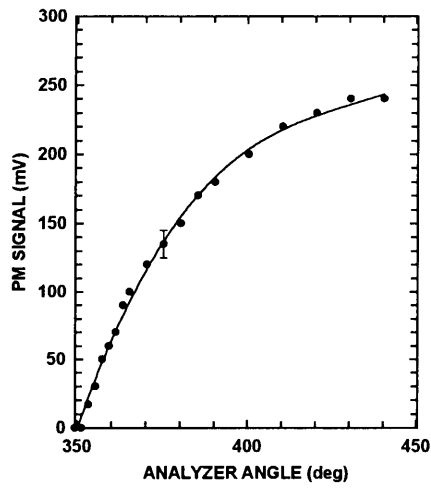
This pulse width can be calculated as follows:

The mirror rotates at 5220 RPM. It therefore makes one revolution in 1.15×10^{-2} seconds. If the mirror is considered to be at the centre of a circle with radius equal to the path length of the He-Ne beam (≈ 6.15 m), the circumference of the circle is 38.64 m. However, the beam rotates through twice the angle through which the mirror rotates. If the diameter of the ellipsometer entrance aperture is 2.2 mm, it means that the beam rotates through an angle of 7.15×10^{-4} rad while traversing the aperture. Since one revolution takes 1.15×10^{-2} seconds, the pulse width of the beam is therefore about 1.3 μ s, in fair agreement with the measured pulse width of about 2 μ s. The discrepancy is due to the finite spot size.

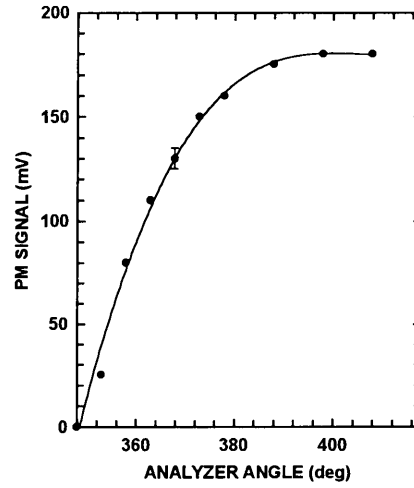
For the calibration the ellipsometer was firstly zeroed for transmission of the He-Ne beam and the analyser setting recorded. The analyser circle was then rotated through small steps and the signal on the oscilloscope recorded at each step. These results for Si and GaAs are shown in Fig. 5.9(a) and (b) respectively. It is clear from the graphs that the photomultiplier started saturating around 150 mV. This happened due to the longer pulse width of the He-Ne (~ 2 μ s) compared to the pulse width of the ruby laser (40 ns). It was therefore decided to use only the first linear part of the graphs for the calibration calculations.

The photomultiplier signals, however, differ for different experiments. Reasons for this include the photomultiplier voltage used, the alignment of the photomultiplier with the set-up and the noise factor described in part A, section 2.2. It is therefore necessary to convert the photomultiplier signals to ellipsometer transmissions.

The transmissions for the analyser angles in Fig. 5.9(a) and (b) can then be calculated from the expressions derived in section 2.3.2. The results are shown in Fig. 5.10.(a) and (b). To do this, values for G are needed for the samples. Since the transmission is the ratio of the amount of light intensity that passes through the ellipsometer system, to the input intensity,

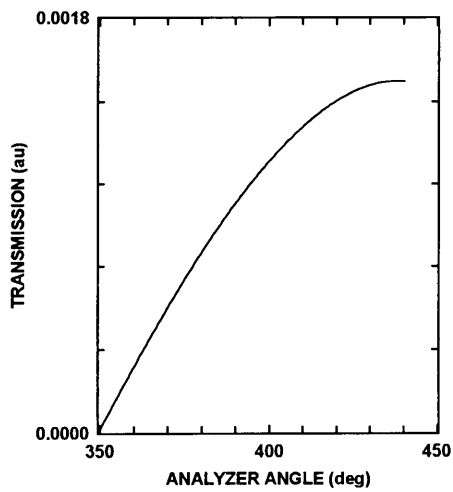


(a)

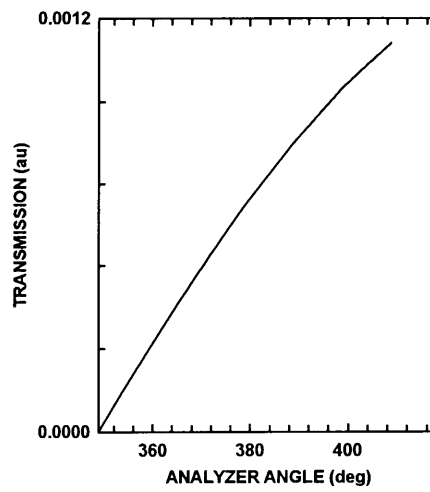


(b)

Fig. 5.9 (a) The photomultiplier signal recorded for Si, as a function of the analyser angles. (b) The photomultiplier signal for GaAs, as a function of the analyser angles.



(a)



(b)

Fig. 5.10 (a) The ellipsometer transmission for Si calculated as a function of the analyser angles. (b) The ellipsometer transmission for GaAs calculated as a function of the analyser angles.

one can measure these intensities for the different analyser angles and compare the ratios with the calculated LL^* -values at these angles to find G . This gave values for G of $\sim 2.65 \times 10^{-4}$ and $\sim 2.55 \times 10^{-3}$ for Si and GaAs respectively. The small values of G are due to the fact that the transmission axis of the polarizer was set almost perpendicular to the polarization direction of the He-Ne. The ellipsometer transmissions can now be plotted as a function of the PM signals and thus the transmissions for each of the six ruby shots can be found. This will be discussed in the chapter on results and discussions.

4. Calculation of some properties of the silicon and GaAs samples

This section will show the calculations for the energy densities, peak intensities, the refractive indices and oxide layer thicknesses of the silicon and GaAs samples.

4.1 The energy densities and peak intensities

As was mentioned before, the energy of the ruby laser was measured with an energy meter, by illuminating it with part of the laser beam. This was done by placing a transparent glass plate in the beam path, which then reflected 8% of the beam onto the energy meter. The meter registered an energy of 12 mJ. Therefore, the total energy that the ruby laser produces is $12/0.08 = 150$ mJ.

Next, the amount of laser energy that reaches the sample, must be calculated. The transmission of a glass/quartz interface is 0.96. There are six such interfaces in the beam path: two glass plates and one lens (see Fig. 5.4). Furthermore, it is assumed that the angle of incidence of the beam on the gold mirror is $\sim 45^\circ$. According to the Fresnell equations this gives a reflection of $R_p = 0.9357$. Therefore, the energy that reaches the sample is: $\text{Energy} = 0.15 \times (0.96)^6 \times 0.9357 = 109.86 \text{ mJ} \cong 0.11 \text{ J}$.

The area of the ruby spot on the silicon is given by: $\text{area} = \pi(0.1)^2 = 0.0314 \text{ cm}^2$. This gives an energy density of: $\text{ED}_{\text{Si}} = 0.11/0.0314 = 3.5 \text{ J cm}^{-2}$.

The area of the ruby spot on the GaAs is given by: $\text{area} = \pi(0.15)^2 = 0.071 \text{ cm}^2$ and this gives an energy density of: $\text{ED}_{\text{GaAs}} = 0.11/0.071 = 1.6 \text{ J cm}^{-2}$.

The pulse width (FWHM) of the ruby laser is 40 ns. The peak intensity of the silicon is therefore: $\text{PI}_{\text{Si}} = 3.5/40 \times 10^{-9} = 8.75 \times 10^7 \text{ W cm}^{-2}$, and for the GaAs it is: $\text{PI}_{\text{GaAs}} = 1.6/40 \times 10^{-9} = 4.0 \times 10^7 \text{ W cm}^{-2}$.

4.2 Refractive indices and oxide layer thicknesses of the samples

The refractive indices and oxide layer thicknesses were calculated using standard ellipsometer methods - see for example Azzam [Azzam R. M. A. and Bashara N. M. (1989) chapter 3].

The refractive indices of the samples were measured with the ellipsometer by finding polarizer and analyser angles for which there is zero transmission of the He-Ne and then using the standard ellipsometer expressions to calculate $\tilde{n} = n - ik$. For silicon $\tilde{n} = 3.867 - 0.192i$ and for GaAs $\tilde{n} = 3.619 - 0.768i$. These values differ from those for the pure substances and therefore an oxide layer must be present on the sample surfaces.

Assume a refractive index of $\tilde{n} = 3.882 - 0.019i$ for pure silicon and that the oxide layer consists of SiO_2 , which has a refractive index of $n = 1.4572$ [Handbook of Chemistry and Physics (1962 - 1963)]. This gives an oxide layer thickness of $\sim 24 \text{ \AA}$.

For pure GaAs a refractive index of $\tilde{n} = 3.860 - 0.198i$ was assumed. Its native oxides are a combination of Ga_2O_3 and As_2O_3 , which has a refractive index of $n \cong 1.81$ [Aspnes D. E. *et al.* (1981) pp. 590-597]. This gives an oxide thickness of $\sim 80 \text{ \AA}$.

CHAPTER 6

RESULTS AND DISCUSSION

In this chapter the experimental and theoretical results will be discussed. The chapter is divided into two parts: part A, which will concentrate on the results of the optical properties of the moth wing, and part B, which will cover the characteristics of the light induced periodic surface structures.

Part A:

In part A the experimental and theoretical optical properties of the moth wing will be compared and discussed. This includes the angular spread of light scattered from the wing, the dependence of diffraction efficiency on the wing orientation, wavelength, dispersion of the scale material, variation in the angle of incidence and dimensional variations.

The good qualitative agreement obtained with the theoretical model indicates that one can interpret the optical characteristics of the wing in terms of diffraction from the three-dimensional grating structure on the scale surface.

1. Angular spread of light on the wing

One of the most prominent features of the moth wing is its ability to reflect light specularly, thus resembling a metallic film, which obeys the law of reflection. This aspect was investigated by using the method described in part A, section 3.1 of the chapter on measuring techniques.

Fig. 6.1(a) shows the experimental results for light (wavelength 550 nm) incident at an angle of 60° . A strong peak is observed at the position for specular reflection, i.e. $\theta_i = \theta_d = 60^\circ$ and it is important to note that the diffracted beam has an appreciable angular spread around the peak position. The collection lens was covered with a vertical slit aperture limiting the observation angle to about 3° , which is substantially less than the observed spread. The observed angular spread is somewhat smaller when the wing is rotated through 90° about the Z-axis (see Fig. 3.3(a)).

In Fig. 6.1(b) and (c) the results of the theoretical model are shown. The expected angular spread is less than 1° for both orientations if coherent diffraction is assumed for one complete wingscale, which is clearly not in agreement with the observations. The angular spread is primarily determined by the dimensions over which the diffracting ribs appear consistent and coherent to the incoming light. In Fig. 6.1(b) it was assumed to be equal to the exposed part of a single scale on the wing, i.e. about sixty by sixty micron or approximately 300 micro ribs in the Y-direction and 36 strips along the X-direction.

A close inspection of the SEM-micrograph in chapter 3 Fig. 3.1(a) shows that there are frequent breaks in the pattern along the vertical (Y-) direction. The best match between measurement of the angular width of the diffracted beam and the calculated values is obtained if the summation was done over 40 micro ribs along Y and one single strip along X. Therefore, in the model index values of 40 and 2 were used for q and p respectively (see Fig. 3.8(b)). The model also predicts a shift in the peak position of the vertical position of the wing and secondary maxima, which was not observed experimentally. A possible explanation for this is the fact that the wing scales and membrane are not perfectly flat and that the scales are not all oriented in the same way. The secondary maxima on the calculated results may be related to the raised ridges spaced by $1.6 \mu\text{m}$ and since these maxima are expected to be much weaker than the main peak, they are not observed experimentally.

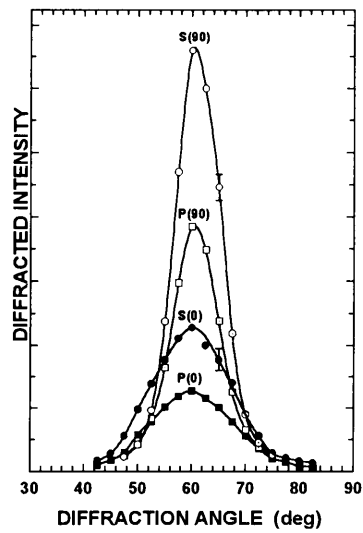


Fig. 6.1 (a) Experimental measurement of the angular spread of the diffracted beam for line CC vertical and rotated through -90° in the plane of the wing. The solid dots and open circles represent S-polarization and the solid and open squares represent P-polarization. Wavelength is 550 nm.

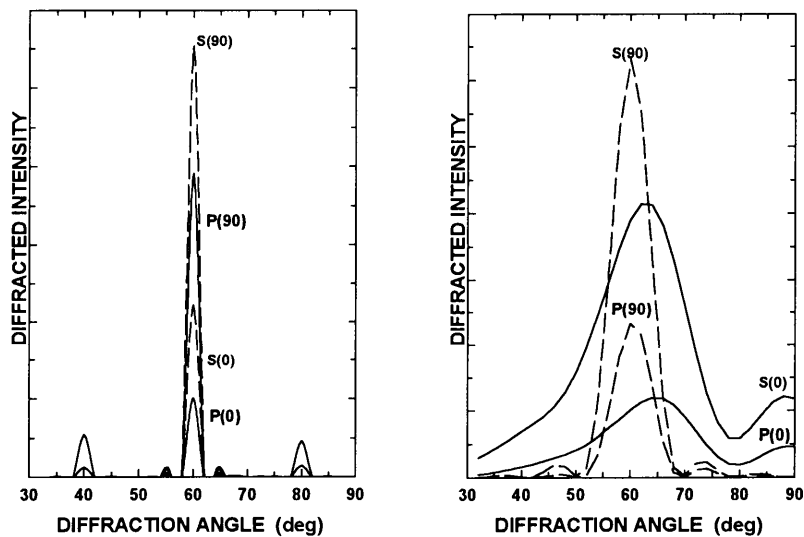


Fig 6.1 (b) Calculated angular spread for line CC vertical (solid line) and rotated by 90° (dashed line), with values of 300 and 72 for indices q and p respectively. Wavelength is 550 nm. (c) Calculated angular spread for line CC vertical (solid line) and rotated by 90° (dashed line). Wavelength is 550 nm.

2. Wing orientation

The intensity of diffracted light depends strongly on the angle of incidence and the orientation of the wing in its own plane (different angles ϕ_r). Note that the condition for specular reflection is maintained in this part of the work. Figs. 6.2(a) and (b) show the experimental results for incident S- and P-polarized light respectively and Fig. 6.2(c) shows the calculated results. Significantly less diffracted light is observed and predicted when the wing is vertical ($\phi_r = 0^\circ$), except in the case of P-polarized light incident at 30° .

A slight asymmetry in the position of the minimum and in the height of the left ($\phi_r = -90^\circ$) and right ($\phi_r = 90^\circ$) maxima is predicted and also supported by observation. Changing the wing orientation from -90° to 90° is equivalent to interchanging the directions of the incident and diffracted beams. It is therefore evident that the wing scale acts as a non-reversible polarizing element. Both predicted and measured results indicate a somewhat enhanced efficiency for S-polarized light. Consequently, when viewed in essentially unpolarized light, as in nature, the diffracted light will be linearly polarized to a fairly high degree, depending on the orientation of the wing with respect to the observer.

3. Spectral distribution

Fig. 6.3(a) shows the spectral distribution of the diffracted light for S- and P-polarization. In all the spectra the blue component of the spectra is diffracted less efficiently than the other spectral components. The wing therefore has a golden-yellow appearance. In Fig. 6.3(b) the calculated spectra are shown. The calculated spectra compare favourably with the experimental spectra, except for the hump around 500 nm. This is possibly due to shortcomings in the Stratton-Silver-Chu formulation and to unknown material properties (i.e. the refractive index could be complex).

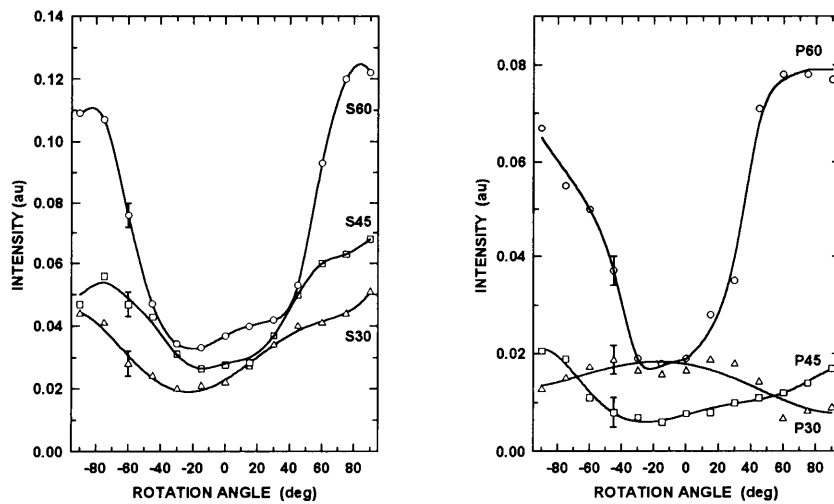


Fig. 6.2 (a) Measured dependence of diffracted power on wing orientation (rotation in the plane of the wing. Rotation angle = 0° for line CC vertical) for S-polarized incident light at angles of incidence 30°, 45° and 60°. Wavelength is 550 nm. The units on the Y-axis are the photomultiplier output normalised to a direct reading without reflection from the moth wing. However, since the light collection efficiency may differ for the collimated direct beam and the diffracted beam, the units should be regarded as arbitrary (au). They can, however, be used to compare Figs. 6.2(a), (b) and Fig. 6.3(a). (b) Measured dependence of diffracted power on wing orientation for P-polarized incident light. Conditions as for (a).

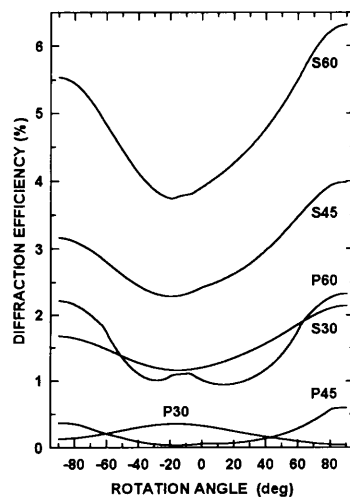


Fig 6.2 (c) Calculated dependence of diffraction efficiency on wing orientation. Conditions as for (a) and (b).

Azzam and Bashara [Azzam R. M. A. and Bashara N. M (1972) pp. 4721-4729] pointed out that the Stratton-Silver-Chu integral suffers from considerable inaccuracy when used to calculate absolute diffraction efficiencies. By making use of a simple renormalisation procedure described in App. B, the accuracy should be improved. If this normalisation procedure is not followed, the blue components appear stronger than the red components, which is totally at variance with the observed spectral properties. Also a zero dispersion of the scale material was assumed, that is a fixed value of 1.56 for the refractive index. Other explanations could be the presence of an absorbing substance rendering refractive index complex or the fact that the sub-structure of the scale (see chapter 3 Fig 3.1(b)) was not included in the calculation.

4. Dispersion of the scale material

The effect of dispersion of the scale material was investigated and the results are shown in Fig. 6.4. The values used for the refractive index fits are: 1.7, 1.56 and 1.4 (dashed line) for $\lambda = 400$ nm, 550 nm and 800 nm respectively, 1.57, 1.56 and 1.55 (dot dash) for $\lambda = 400$ nm, 550 nm and 800 nm respectively and 1.56 (constant) (dotted line) for $\lambda = 400$ nm, 550 nm and 800 nm respectively. It is clear that dispersion of the scale material does not play a significant role and therefore a fixed value of 1.56 could be assumed.

5. Angle of incidence

Physical restrictions on the experimental set-up made measurements over a wider range of angles impossible, but it can be readily calculated. The diffraction efficiency for the wing rotated in its own plane by $\phi_r = +90^\circ$ is shown in Fig. 6.5. As can be seen, the wing is a much better reflector at high angles of incidence and strong polarization effects can be expected when $\theta_i \approx 30^\circ$. The experimental points, taken from Fig 6.2 and scaled to provide a best fit, are in qualitative agreement with the calculated predictions.

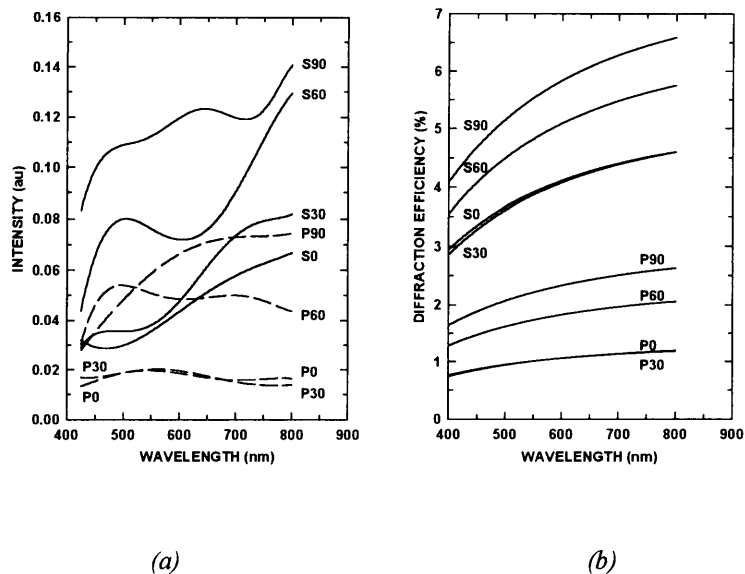


Fig. 6.3 (a) Measured spectral distribution of diffracted light for S- (solid) and P-polarized (dashed line) incident light at rotation angles 0° , -30° , -60° and -90° . Angle of incidence is 60° . (b) Calculated spectral distribution. Conditions as for Fig. 0.3(a).

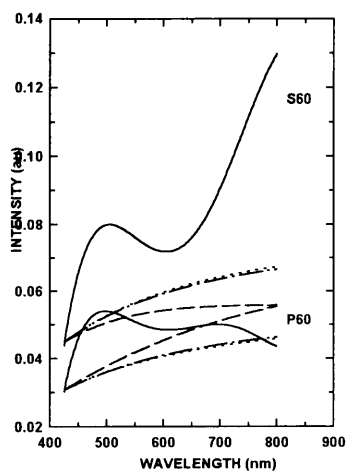


Fig. 6.4 Calculated spectral distribution for the dispersion of the scale material. Values used for the refractive index fits are: 1.7, 1.56 and 1.4 (dashed line) for $\lambda = 400$ nm, 550 nm and 800 nm respectively, 1.57, 1.56 and 1.55 (dot dash) for $\lambda = 400$ nm, 550 nm and 800 nm respectively and 1.56 (constant) (dotted line) for $\lambda = 400$ nm, 550 nm and 800 nm respectively.

6. Dimensional variations

The question now arises why the wing is constructed with this specific set of parameters? Why not another set? By varying the different parameters one can try to answer this question. The results are shown in Fig. 6.6(a) and (b).

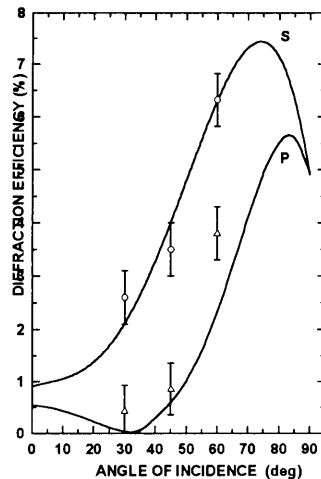


Fig. 6.5 Calculated dependence of diffraction efficiency for S- and P-polarized incident light on angle of incidence θ_i . Diffraction angle is equal to θ_i . Wavelength is 550 nm. Rotation angle is 90° .

The dashed line in the figures represents the variation in the flat portions between the micro ribs, i.e. the fraction of the wing allocated to planes of the types 5 and 6. As can be seen there is not much variation due to this parameter and the actual value corresponds roughly to the best overall efficiency.

With the line CC vertical ($\phi_r = 0^\circ$), variations in the spacing between micro ribs have little influence on diffraction efficiency, except for very small spacings (of the order of 40 nm), for which the efficiency drops considerably. Rotating the wing through 90° results in the opposite situation with a small spacing giving an enhanced efficiency. The actual spacing therefore seems to be a good trade-off for best diffraction efficiency at any wing orientation. Changing the height of the micro ribs results in a similar situation with the actual height giving a best trade-off between the two orientations investigated.

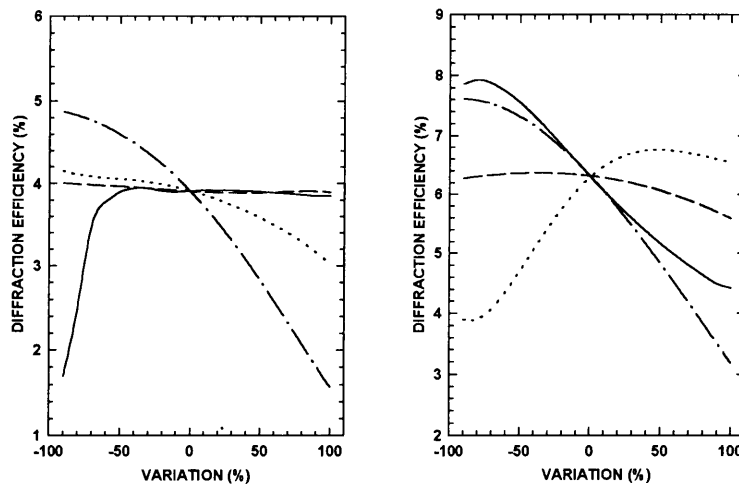


Fig. 6.6 (a) Calculated influence of variation in parameter values (variation = $\left(\frac{P - P_0}{P_0}\right)100$) on diffraction efficiency for line CC vertical. Parameters changed are: spatial period of pattern ($2h + f$) (solid line), fraction of area taken up by planes 5 and 6 ($\frac{f}{2h + f}$) (dashed line), height of the micro ribs (d) (dotted line) and depression of the centre of a strip (ϕ_d) (dot dash). Wavelength is 550 nm. Angle of incidence is 60° . (b) Calculated influence of variations of parameter values on diffraction efficiency for the wing rotated by 90° in its own plane. Curves are identified as in (a).

Consider now the variation in the depression of the central part of a strip (line CC in Fig. 3.3(a)). The efficiency is improved for all orientations of the wing when the depression is reduced to zero. However, this will result in a spectral distribution in which the characteristic yellow color is lost. Qualitatively one can understand this effect by noting that the depth modulation is approaching half a wavelength for the ultra violet and blue parts of the spectrum, which should result in destructive interference reducing the diffraction efficiency. It is also conceivable that structural strength may play a role in this case.

7. Conclusion

It is evident that the observed optical characteristics of the wing can be explained as a diffraction process which is primarily due to the micro structure on the scales of the wing. It is also apparent that the Stratton-Silver-Chu formulation provides fairly accurate results providing that the normalisation procedure is followed.

Part B:

In part B the experimental and theoretical results of the investigation of the light-induced periodic surface structures will be compared and discussed. Firstly, though, a brief overview of the carrier-lattice interaction will be given. This is important, since the temperature dependent expressions used in the model are taken from the Melting Model described by Wood [Wood R. F. *et al.* (1984) pp. 165-250]. One of the concerns of the Melting Model is the transfer of energy from the carrier system to the lattice, resulting in melting of the top layer of the surface. The techniques used for the experimental measurements were discussed in the chapter on experimental techniques and apparatus, part B. The theoretical predictions were produced using the mathematical modelling discussed in chapter 4.

1. The carrier-lattice interaction

The carrier-lattice interaction that occurs after the laser pulse strikes the surface is discussed in detail by Wood [Wood R. F. *et al.* (1984) pp. 165-250]. A brief overview of this process will be discussed at the hand of a schematic outline, adapted from von Allmen [von Allmen M. (1980) p.6]. This outline is given in Fig. 6.7.

Energy from the laser pulse is absorbed by the semiconductor, causing band-to-band electronic transitions indicated by event **a** in the figure. Free carrier absorption by the excited electrons then occurs (events **b** and **c**), followed by electron-electron collisions. These collisions produce a thermal equilibrium distribution among the carriers about the energy kT_e (crossed-hatched area), where T_e is greater than the lattice temperature. This happens in times of the order of 10^{-14} sec. Impact ionisation and Auger recombination bring the electron and hole populations into thermal equilibrium at about the same time. Note that there is energy transfer between the electrons and holes without energy dissipation of the carrier system. Energy is then transferred to the lattice, in times of the order of 10^{-12} sec, by phonon emission. This can cause heating of the lattice to the melting point in a few picoseconds. Simultaneously, the carrier density is reduced by Auger

recombination. However, since the carrier densities estimated by the model used in this presentation were lower than 10^{21} cm^{-3} , the Auger recombination effect was ignored.

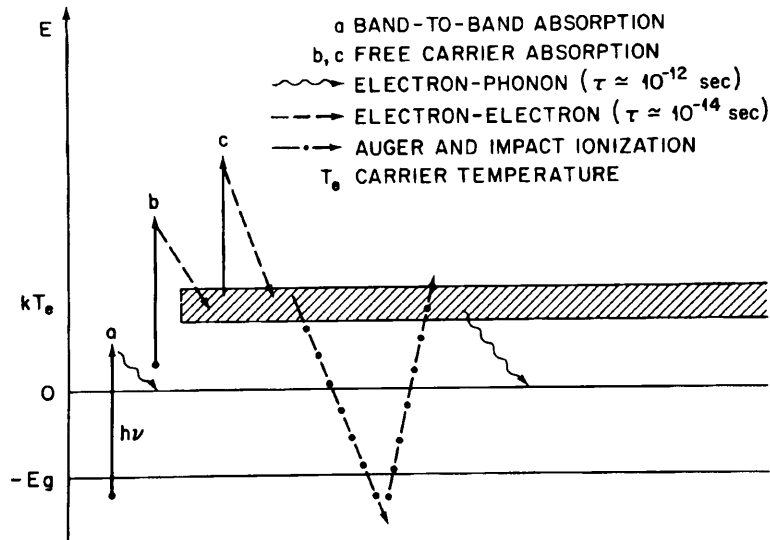


Fig. 6.7 Schematic illustration of the elementary photoexcitation processes, carrier equilibration mechanisms, and electron-phonon interactions in a semiconductor exposed to laser radiation with $h\nu \geq E_g$. Adapted from von Allmen (1980). [Wood R. F. (1984) pp.177]

Thermal diffusion of the carriers also plays an important role in the heating of the lattice., The thermal diffusion length is estimated to be $\sim 4 \mu\text{m}$. Together with the absorption length of $\sim 4 \mu\text{m}$ (inverse of absorption coefficient), it gives a penetration depth of $\leq 8 \mu\text{m}$.

2. Results: Experimental and theoretical

In order to be able to compare the experimental results with the theoretical results from the model, it was first of all necessary to calibrate the ellipsometer transmission. Fig. 6.8(a) and (b) shows the ellipsometer transmission as a function of the PM signal recorded for Si and GaAs respectively. The upward curvature of the graphs is the result of the

photomultiplier starting to saturate at 150 mV. The first part of the graphs shows the expected linear relationship between the transmission and the intensity. It was therefore decided to use only the linear parts of the graphs to calculate a proportionality constant, k , for each sample.

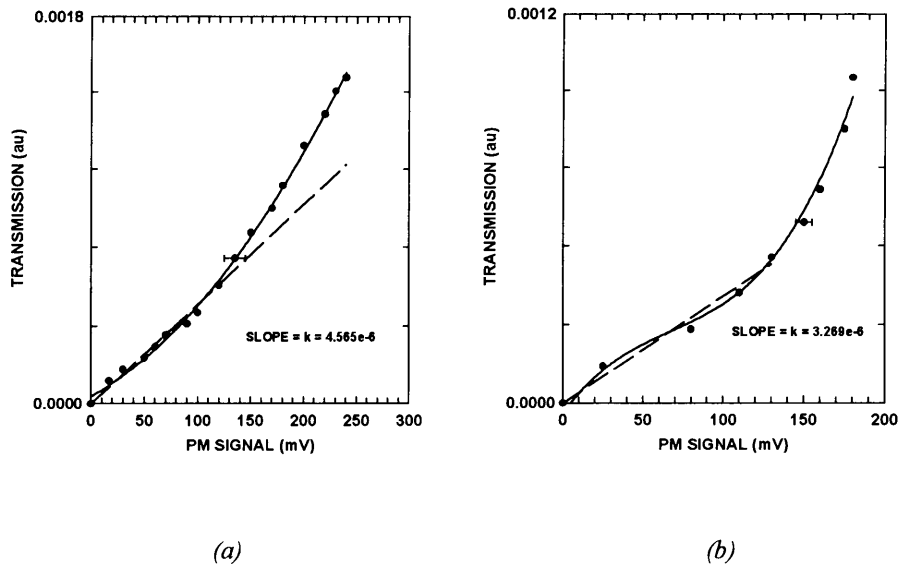


Fig. 6.8 (a) The ellipsometer transmission as a function of the recorded PM signal for Si. (b) The ellipsometer transmission for GaAs.

Although the LIPS-structures can be formed with a single laser pulse, there exists during the first few pulses both temporal and spatial evolutionary processes, before a distinctive and shot-independent structure is formed [Young, J. S. *et al.* (1983) pp. 1155-1172].

The ellipsometer transmission for the six sequential shots for Si is shown in Fig. 6.9(a) and those for GaAs in Fig. 6.9(b). The first shot in each graph shows a very low transmission and it is unlikely that any structure was formed. The experiment was performed twice and the transmission for the second shot of each experiment calculated. These two values were then subtracted to find the error, which is around 10%. The LIPS-structures appears to reach a maximum and approximately stable height around the fifth shot, clearly demonstrating the evolutionary development of the LIPS-structures.

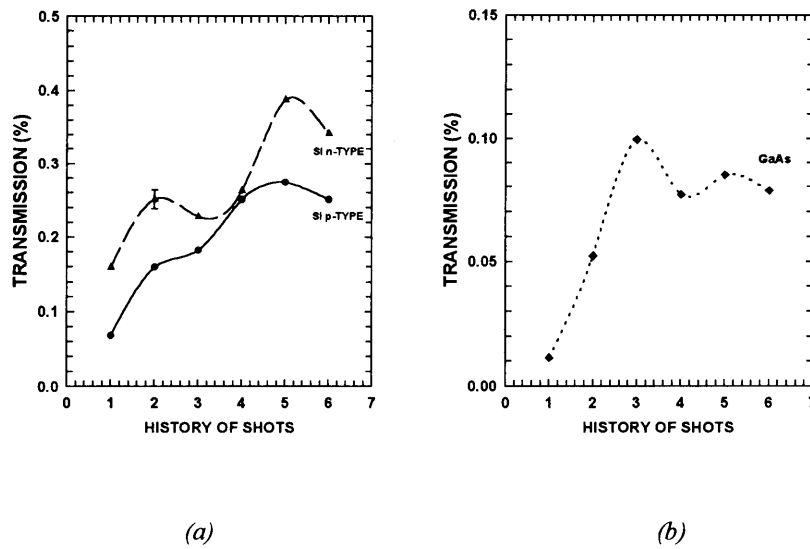


Fig. 6.9 (a) The ellipsometer transmission results for n- and p-type Si. The pulse width of the ruby laser used is 40 ns and the laser energy density is 3.5 J cm^{-1} . (b) The ellipsometer transmission results for GaAs. The laser energy density is 1.6 J cm^{-1} . Therefore, the results of (a) and (b) cannot be compared.

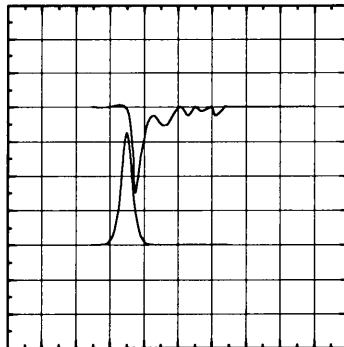


Fig. 6.10 Scematic drawing showing the oscilloscope recording of the ruby laser pulse and the LIPS-structures. The time scale on the horizontal axis is 50 ns for each small division. On the vertical axis each small division represents a scale of 2 V and 200 mV respectively.

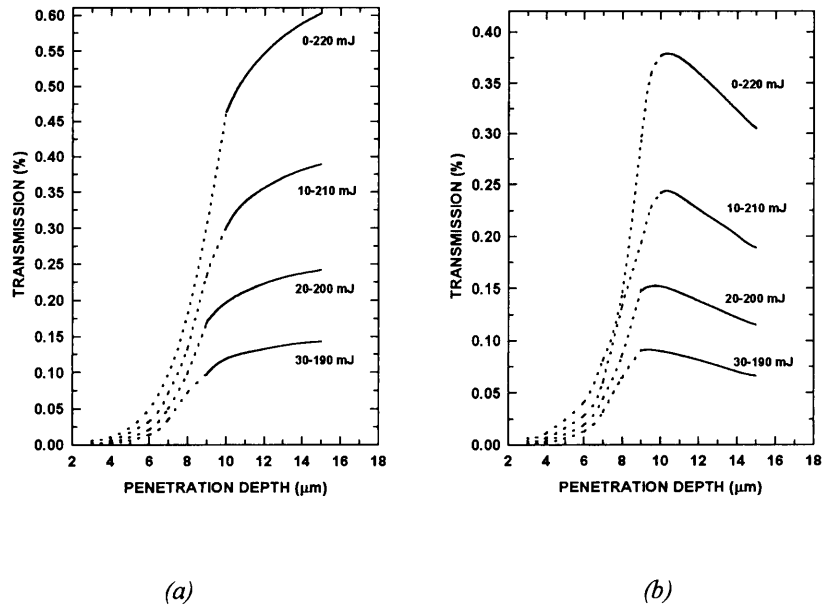


Fig. 6.11 (a) Calculated ellipsometer transmissions for the case where the effect of the light-induced carrier density is ignored. The transmission is shown as a function of the penetration depth, for different energy distributions. The solid lines represent the unmolten Si and the dashed lines the molten Si. (b) The same as (a), but now with the effect of the carrier density included.

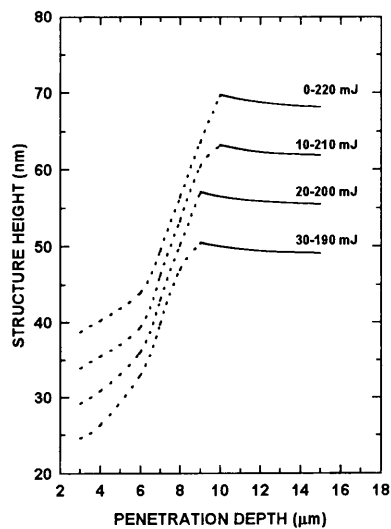


Fig. 6.12 The structure height as a function of the penetration depth. The representation is the same as in Fig. 6.11(a).

Although the LIPS-structures formed on GaAs follow the same tendency as those on Si, the two sets of measurements can not be directly compared, since a lower laser energy density of 1.6 Jcm^{-2} (compared to 3.5 Jcm^{-2} for Si) had to be used for the GaAs to prevent surface damage to the substrate. At these low energy densities no evidence of any LIPS-structures could be seen on the Si. The somewhat higher absorption coefficient of GaAs at the ruby wave-length ($\sim 29\,000 \text{ cm}^{-1}$ compared to 2705 cm^{-1} for Si) is probably responsible for this behaviour [Blakemore J. S. (1982) pp. R150; Aspnes D. E. (1987) RN=17807 pp. 72-79].

The next point to consider is the time evolution of the structures. Fig. 6.10 shows the laser pulse and an example of the LIPS-structures. The time scale on the horizontal axis is 50 ns for each small division. On the vertical axis each small division represents scales of 2 V and 200 mV respectively. It is clear that the formation of the structures reached a maximum approximately 20 ns after the laser pulse maximum. The structures also take about 250 ns to decay, indicating that melting did occur.

The model was developed only for Si and therefore the theoretical results will only be compared with Fig. 6.9(a). The model was not applied to GaAs, due to an incomplete knowledge of the temperature dependence of the optical properties of the GaAs.

In Fig. 6.11(a) the theoretical results are shown for the case in which the effect of the photo-induced carrier density is ignored. The transmission is shown as a function of the penetration depth (d) for different energy distributions. For each energy distribution the average energy is 110 mJ, which is the energy of the laser beam that reached the sample. The solid line in the graph represents the unmolten silicon and the dashed line the molten state. It is clear from the graph that the transmission increases with increased penetration depth.

When a material is heated, it expands. As the heated surface expands, the structure height is increased, influencing the polarization to a larger degree and thus yielding a higher transmission. The structure height as a function of penetration depth is shown in Fig. 6.12. It is clear that as the temperature is raised, the surface expands and the structure height is

increased. This height reaches a maximum just before melting occurs. In chapter 4, section 4 the structure height was given by the expression

$$H = d(\beta_{\max} T_{\max} - \beta_{\min} T_{\min}).$$

If the value of d , i.e. the penetration depth, gets small enough, the structure height decreases, as is clearly seen on the graph. This in turn will lead to a decrease in transmission (see Fig. 6.11(b)).

Fig. 6.11(b) shows the same results, but with the effect of the carrier densities included. The inclusion of the carrier densities causes a change in the refractive index of Si. For example, for a temperature of 1650 K the refractive index changes from $5.804 - 0.353i$ for the case without the carrier densities included, to $5.967 - 1.43i$ for this case. Therefore the Fresnell coefficients will differ and thus also the values for the transmission. In this case the transmission reaches a peak around $9 \mu\text{m}$ penetration depth.

Comparing the experimental results (see Fig 6.9(a)) and the calculated theoretical results (see Fig. 6.11(b) and Fig. 6.12) it is estimated that the observed structure has a height of 60 - 70 nm, the energy and temperature in the valley of the structure is $\sim 0 - 10 \text{ mJ}$ and $\sim 300 - 350 \text{ K}$ respectively and the energy and temperature at the top of the structure is $\sim 210 - 220 \text{ mJ}$ and $\sim 1685 - 1700 \text{ K}$ respectively. The melting temperature of Si is 1685 K, so this indicates that the top layer of the surface structure indeed melts.

It must be noted that these values for the height, energies and temperatures are only rough estimates and are strongly model dependent. The reason for this is two-fold. Firstly, as been noted in part A, section 3, the Stratton-Silver-Chu integral suffers from considerable inaccuracy when used to calculate absolute diffraction efficiencies. The second reason involves the calibration of the ellipsometer transmission. In chapter 5, part B, section 3.3, this calibration procedure was discussed. The pulse width of the He-Ne was $\sim 2 \mu\text{sec}$, where the pulse width of the ruby laser was only 40 nsec. Due to the physical dimensions of the laboratory it was impossible to increase the path length of the He-Ne. Also the

rotating mirror was rotated at maximum speed and these two factors limited the pulse width that could be reached.

CHAPTER 7

CONCLUSIONS

Part of this study attempted to explain the way light is scattered by the golden patch on the wings of the *Trichoplusia orichalcea* moth. The observed optical properties can be explained as a diffraction process due to the micro structure on the wing. When the angle of incidence is almost equal to the angle of diffraction, the diffracted intensity shows a strong peak. This indicates that a zero order diffraction process is dominating. The intensity of the diffracted light also strongly depends on the angle of incidence and the orientation of the wing in its own plane. It also appears that the micro structures on the wing are roughly optimised to give the best overall diffraction efficiency.

The study also demonstrated the basic feasibility of using real-time ellipsometry to detect and characterise the formation of the LIPS-structures on single-crystal Si and GaAs. If this technique is compared to diffractometry (described in ch. 1, part B), it is clear that ellipsometry is much more sensitive to very small surface structures and that larger signals are generated. The mathematical model used suggests that the LIPS-structures has a height of approximately 65 nm and that there are energy and temperature distribution profiles across the structures. It also seems that melting of the top layer of the surface occurred in narrow strips spaced by the wavelength of the ruby laser.

A shortcoming to the moth theory is the lack of detailed information on the refractive index of the material the diffracting structure is made of, and the substructure of the scale. Future work is planned to measure the complex refractive index of the wingscale material using the ellipsometer.

It is also planned to investigate the time evolution of the LIPS-structures in more detail by employing normal incidence ellipsometry. In this case the ellipsometer signal should be due only to an asymmetry of the reflecting surface giving a more unambiguous result.

APPENDIX A

In chapter 2 the derivation of the Stratton-Silver-Chu integral is given. The vector theorems and identities needed for the derivation will be stated, without proof, in this appendix. Only the “vector” Helmholtz equations will be derived from the Maxwell equations.

A.1 Divergence Theorem

Let V be a volume bounded by a surface S . The surface integral of the normal component of a vector over S is equal to the integral of the divergence of the vector over V . That is:

$$\oiint_S \vec{F} \cdot \hat{n} ds = \iiint_V \nabla \cdot \vec{F} dv.$$

A.2 Stokes Theorem

The line integral of a vector around a closed curve C is equal to the integral of the curl of the vector’s normal component over a surface S bounded by the curve C . That is:

$$\oint_C \vec{F} \cdot d\vec{l} = \iint_S \nabla \times \vec{F} \cdot \hat{n} ds.$$

A.3 Green’s Theorem for multiple-connected planes

Consider a volume V bounded by surfaces S_1, \dots, S_n . Let \vec{F} and \vec{G} be two continuous vector position functions and let their first and second derivatives be continuous

everywhere inside V and on all the boundaries. Also, let \hat{n} be a unit vector normal to any boundary surface, directed into V . Then

$$\begin{aligned} & \iiint_V (\vec{F} \cdot \nabla \times \nabla \times \vec{G} - \vec{G} \cdot \nabla \times \nabla \times \vec{F}) dV \\ &= \iint_{S_1 + \dots + S_n} (\vec{G} \times \nabla \times \vec{F} - \vec{F} \times \nabla \times \vec{G}) \cdot \hat{n} dS. \end{aligned}$$

Vector identities:

Let \vec{F} be a vector function and ψ a scalar function. Then:

$$\mathbf{A.4} \quad \nabla \times (\psi \vec{F}) = (\nabla \psi) \times \vec{F} + \psi \nabla \times \vec{F}.$$

$$\mathbf{A.5} \quad \nabla \cdot (\psi \vec{F}) = (\nabla \psi) \cdot \vec{F} + \psi (\nabla \cdot \vec{F}).$$

$$\mathbf{A.6} \quad \iiint_V \nabla \times \vec{F} dV = \iint_S (\hat{n} \times \vec{F}) dS.$$

A.7 "Vector" Helmholtz equations

The general time-periodic Maxwell equations are:

$$\nabla \times \vec{E} + i\omega \vec{B} = 0 \tag{A.7.1}$$

$$\nabla \times \vec{H} = \vec{J} + i\omega \vec{D} \tag{A.7.2}$$

$$\nabla \cdot \vec{D} = \rho \tag{A.7.3}$$

$$\nabla \cdot \vec{B} = 0 \tag{A.7.4}$$

In order to derive the equation for the electric field, take the curl of eq. (A.7.1). This gives:

$$\begin{aligned}\nabla \times \nabla \times \vec{E} &= \nabla \times (-i\omega \vec{B}) \\ &= -i\omega (\nabla \times \vec{B})\end{aligned}\tag{A.7.5}$$

Since $\vec{B} = \mu \vec{H}$, eq. (A.7.2) can be substituted into eq. (A.7.5) to give

$$\begin{aligned}\nabla \times \nabla \times \vec{E} &= -i\omega \mu (\vec{J} + i\omega \epsilon \vec{E}) \\ &= -i\omega \mu \vec{J} + k^2 \vec{E}\end{aligned}$$

or

$$\nabla \times \nabla \times \vec{E} - k^2 \vec{E} = -i\omega \mu \vec{J}.\tag{A.7.6}$$

The equation for the magnetic field is derived in the same way and will therefore not be shown here.

APPENDIX B

Chapter 3 describes the mathematical modelling for the moth wing. In this appendix the accompanying computer program, written in C++, is given. A shortcoming of the Stratton-Silver-Chu integral is that it does not give correct absolute values for the scattered intensities. One way of overcoming this is to consider the situation where the wing is taken to be flat without any structures or elevated regions, i.e. it is approximated by a simple flat plane. The Fresnell coefficients for this plane are then calculated and the intensities calculated from the integral normalised to these values. This is done in the normalisation routine in the program.

/* PROGRAM StratSilverChu

Program to calculate diffraction integral of Stratton Silver Chu
 for moth wing

V6.0 Sept '94 Prof D J Brink

V7.0 Nov '94 Miss J E Smit

symetric grooves: alfa_1=alfa_2=alfa_3=alfa_4
 beta_1=beta_2=beta_3=beta_4

* flat portion in valley region included

shadowing only on input beams

polarized & unpolarized beams

exact integral v2

singularities avoided

 marked as: wrn=11,12,21,22,31,32,41,42

output normalized to zero profile-depth values

index of refr calculated from polynomial

double angular scan: ia more / da less

* depression of centre included

* complex index of refraction */

#include<stdio.h>

#include<conio.h>

#include<ctype.h>

#include<math.h>

#include<complex.h>

double xcomp,ycomp,zcomp,RtoD,DtoR,rcomp,icomp;

double ww=0.81e-6,wp=85e-9,wd=60e-9,wr=0.3,sa=0.0,ba=0.635,ta,elv,wh,wf;

double ia,da,ea,wl=0.55e-6,klam,pa=0,irre,irim,beta,lam=0.0,ang=0.0;

double kix,kiy,kiz,kox,koy,koz,clai[8];

double nx[8],ny[8],nz[8],qx[8],qy[8];

double px=2,py=40; /* total beam width = 1 strip X 40 ribs */

double dx,dy,dyx,dz,ds,area; /* steps used in scan */

double cint[8],sint[8]; /* real and im parts of integrals */

double ddx,dky,dkz;

double a0=1.56,a1=0,a2=0,a3=0,a4=0; /* expansion coefft's for real part of ind of refr */

double b0=0,b1=0,b2=0,b3=0,b4=0; /* expansion coefft's for imag part of ind of refr */

complex ir = complex(irre, irim);

complex clar[8],EHKx[8],EHKy[8],EHKz[8];

complex xcomp,ycomp,zcomp;

complex IP,In,IPs,IPp;

complex scint[8];

int s[8],as=0,stf=0,nrm=0,rflg=0;

int rept=1,wrn=0,swrn[16];

char selct;

FILE *outfile;

double dot(double x1,double y1,double z1,double x2,double y2,double z2);

complex dotcom(complex x1,complex y1,complex z1,double x2,double y2,double z2);

void cross(double x1,double y1,double z1,double x2,double y2,double z2);

void crosscom(double x1,double y1,double z1,complex x2,complex y2,complex z2);

void mmenu();

void wing();

```

void probe();
void geom();
void emf();
void scan();
void pln1(double xx,double yy);
void pln2(double xx,double yy);
void pln3(double xx,double yy);
void pln4(double xx,double yy);
void calc();
void calc2();
void ioutpt();
void ascan();
void ascan2();
void wscan();
void rscan();
void stfl();
void cddiv(double x1, double y1, double x2, double y2);
void cmul(double x1, double y1, double x2, double y2);
void norm();
void indrefr();

void main()
{
  DtoR=M_PI/180.0; RtoD=180.0/M_PI;
  wf=2.0*wp*wr; wh=wp-wf/2.0;
  ba=35.0*DtoR; ia=60.0*DtoR; da=60.0*DtoR; ea=10.0*DtoR;
  ta=M_PI-2.0*ba;
  elv=ww*tan(ea);
  area=px*py*ww*wp;
  do
  { mmenu(); } while(rept==1);
}

void mmenu()
{
  nrm=0;
  clrscr();
  puts(" ***** MAIN MENU *****");
  printf("\n\n");
  puts("PRESS A KEY AS REQUIRED"); printf("\n\n");
  puts("W: Wing parameters      P: Probe parameters");
  puts("A: Angle scan          D: Double angle scan");
  puts("L: Wavelength scan     R: Rotation scan");
  puts("S: Storage file open   C: Calculate single run");
  puts("Q: Quit");
  selct=toupper(getch());
  switch(selct)
  {
    case 'W' : wing() ; break;
    case 'P' : probe() ; break;
    case 'C' : norm() ; calc() ; break;
    case 'A' : norm() ; ascan() ; break;
    case 'D' : norm() ; ascan2(); break;
    case 'L' : wscan() ; break;
    case 'R' : norm() ; rscan() ; break;
  }
}

```



```

    case 'S' : stfl() ; break;
    default : break;
    case 'Q' : rept=0; break;
  }
}

/*****

double dot(double x1, double y1, double z1, double x2, double y2, double z2)
{
  return(x1*x2 + y1*y2 + z1*z2);
}

/*****

complex dotcom(complex x1, complex y1, complex z1, double x2, double y2, double z2)
{
  return(x1*x2 + y1*y2 + z1*z2);
}

/*****

void cross(double x1, double y1, double z1, double x2, double y2, double z2)
{
  xcomp=y1*z2-y2*z1; ycomp=z1*x2-z2*x1; zcomp=x1*y2-x2*y1;
}

/*****

void crosscom(double x1, double y1, double z1, complex x2, complex y2, complex z2)
{
  xccomp=y1*z2-y2*z1; yccomp=z1*x2-z2*x1; zccomp=x1*y2-x2*y1;
}

/*****

void cmul(double x1, double y1, double x2, double y2)
{
  rcomp=x1*x2-y1*y2;
  icomp=x1*y2+x2*y1;
}

/*****

void wing()
{
  int rs=1;
  do
  {
    clrscr();
    indrefr();
    ta=M_PI-2.0*ba;
    area=px*py*ww*wp;
    wf=2.0*wp*wr;
    wh=wp - wf/2.0;
    puts(" ***** STRUCTURE OF WING *****");
    printf("\n\n");
  }
}

```

```

puts("PRESS A KEY AS REQUIRED"); printf("\n\n");
printf("W: Width   = %E    V: V.patt.rep = %E \n\n", ww, wp);
printf("D: Depth   = %E    F: Flat frac = %E\n\n", wd, wr);
printf(" height  = %E    flat part = %E\n\n", wh, wf);
printf("R: Rotation = %4.1f\n\n", sa*RtoD);
printf("B: Base angle = %4.1f          Top angle = %4.1f\n\n", ba*RtoD, ta*RtoD);
printf("E: Elev angle = %4.1f          Elevation = %E\n\n", ea*RtoD, elv);
printf("I: Indx refr = %4.3f + %4.6f i\n\n", real(ir), imag(ir));
puts("Q: Quit");
selct=toupper(getch());
switch(selct)
{
  case 'W' : printf("projected width of planes (along x) (m) = ");
             scanf("%lg",&ww);
             break;
  case 'F' : printf("fraction of flat plane width (along y) (wf/2wp) = ");
             scanf("%lg",&wr);
             break;
  case 'V' : printf("vertical half pattern repeat (along y) (m) = ");
             scanf("%lg",&wp);
             break;
  case 'D' : printf("depth of structure (m) = ");
             scanf("%lg",&wd);
             break;
  case 'E' : printf("Elevation angle of strip sides = ");
             scanf("%lg",&ea);
             ea=ea*DtoR;
             elv=ww*tan(ea);
             break;
  case 'R' : printf("rotation angle of wing (deg) = ");
             scanf("%lg",&sa);
             sa=sa*DtoR;
             break;
  case 'I' : clrscr();
             printf("expansion coeff'ts for index of refraction:\n");
             printf("a0 = ");
             scanf("%lg",&a0);
             printf("a1 = ");
             scanf("%lg",&a1);
             printf("a2 = ");
             scanf("%lg",&a2);
             printf("a3 = ");
             scanf("%lg",&a3);
             printf("a4 = ");
             scanf("%lg",&a4);
             printf("b0 = ");
             scanf("%lg",&b0);
             printf("b1 = ");
             scanf("%lg",&b1);
             printf("b2 = ");
             scanf("%lg",&b2);
             printf("b3 = ");
             scanf("%lg",&b3);
             printf("b4 = ");
             scanf("%lg",&b4);
             indrefr();
}

```

```

        break;
    case 'B' : printf("base angle of planes (deg) = ");
                scanf("%lG",&ba);
                ba=ba*DtoR;
                break;
    default : break;
    case 'Q' : rs=0; break;
}
} while (rs==1);
}

//*****

void probe()
{
int rs=1;
do
{
ta=M_PI-2.0*ba;
area=px*py*ww*wp;
clrscr();
puts(" ***** PROBE BEAM PARAMETERS *****");
printf("\n\n");
puts("PRESS A KEY AS REQUIRED"); printf("\n\n");
printf("I: Inc angle = %4.1f    D: Diff angle = %4.1f\n\n",ia*RtoD,da*RtoD);
printf("N: no X-planes = %3.0f    M: no Y-planes = %3.0f\n\n",px,py);
printf("W: Wavelength = %4.0f A    P: Pol angle = %3.0f\n\n",wl*1e10,pa*RtoD);
puts("Q: Quit");
selct=toupper(getch());
switch(selct)
{
    case 'I' : printf("Incidence angle (deg) = ");
                scanf("%lG",&ia);
                ia=ia*DtoR;
                break;
    case 'D' : printf("Diffraction angle (deg) = ");
                scanf("%lG",&da);
                da=da*DtoR;
                break;
    case 'N' : printf("number of planes along X = ");
                scanf("%lG",&px);
                break;
    case 'M' : printf("number of planes along Y = ");
                scanf("%lG",&py);
                break;
    case 'W' : printf("Wavelength (A) = ");
                scanf("%lG",&wl);
                wl=wl*1e-10;
                break;
    case 'P' : printf("polarization angle in YZ-plane from Y-axis\n");
                printf("(p=90 / s=0 / un pol=400\n");
                printf("Enter angle (Deg) = ");
                scanf("%lG",&pa);
                pa=pa*DtoR;
    default : break;
    case 'Q' : rs=0; break;
}
}
}

```

```

    }
  } while (rs==1);
}

//*****

void calc()
{
  int j;
  for(j=1;j<7;j++)
  {
    cint[j]=0.0; sint[j]=0.0;
  }
  wrn=0;
  for(j=1;j<13;j++) swrn[j]=0;
  klam=2.0*M_PI/wl;
  indrefr();
  geom();
  emf();
  scan();
  ioutpt();
}

//*****

void geom() /* calculate normal-vectors, k-vectors, local angles */
{
  int j=0;
  double ux,uy,uz,vx,vy,vz,con1,con2,cea,sea,csa,ssa;
  complex con3;
  for(j=1;j<7;j++) s[j]=0; /* set all shadowing to zero */
  /***** find non-rotated n-vector *****/
  con1=ba;
  ux=cos(con1) ; uy=sin(con1) ; uz=0.0 ;
  beta=atan(wd/(wh*cos(ba)));
  con2=cos(beta);
  vx=-con2*uy; vy=con2*ux; vz=sqrt(1-con2*con2);
  cross(ux,uy,uz,vx,vy,vz);
  nx[1]=xcomp; ny[1]=ycomp; nz[1]=zcomp;
  /*****
  ux=-ux; uy=-uy;
  vx=-vx; vy=-vy;
  cross(ux,uy,uz,vx,vy,vz);
  nx[2]=xcomp; ny[2]=ycomp; nz[2]=zcomp;
  /*****
  con1=ba+ta;
  ux=-cos(con1) ; uy=-sin(con1) ; uz=0.0 ;
  vx=-con2*uy; vy=con2*ux; vz=sqrt(1-con2*con2);
  cross(ux,uy,uz,vx,vy,vz);
  nx[3]=xcomp; ny[3]=ycomp; nz[3]=zcomp;
  /*****
  ux=-ux; uy=-uy;
  vx=-vx; vy=-vy;
  cross(ux,uy,uz,vx,vy,vz);
  nx[4]=xcomp; ny[4]=ycomp; nz[4]=zcomp;
  /*****

```

```

nx[5]=0.0; ny[5]=0.0; nz[5]=1.0;
nx[6]=0.0; ny[6]=0.0; nz[6]=1.0;

/***** rotate about y-axis *****/
cea=cos(ea); sea=sin(ea);
for(j=1;j<3;j++)
{
  con1=nx[j]; con2=nz[j];
  nx[j]= con1*cea + con2*sea;
  nz[j]=-con1*sea + con2*cea;
  qx[j]=-nx[j]/nz[j]; qy[j]=-ny[j]/nz[j];
}
j=5;
con1=nx[j]; con2=nz[j];
nx[j]= con1*cea + con2*sea;
nz[j]=-con1*sea + con2*cea;
qx[j]=-nx[j]/nz[j]; qy[j]=-ny[j]/nz[j];
for(j=3;j<5;j++)
{
  con1=nx[j]; con2=nz[j];
  nx[j]= con1*cea - con2*sea;
  nz[j]= con1*sea + con2*cea;
  qx[j]=-nx[j]/nz[j]; qy[j]=-ny[j]/nz[j];
}
j=6;
con1=nx[j]; con2=nz[j];
nx[j]= con1*cea - con2*sea;
nz[j]= con1*sea + con2*cea;
qx[j]=-nx[j]/nz[j]; qy[j]=-ny[j]/nz[j];
/***** rotate about z-axis *****/
csa=cos(sa); ssa=sin(sa);
for(j=1;j<7;j++)
{
  con1=nx[j]; con2=ny[j];
  nx[j]=con1*csa - con2*ssa;
  ny[j]=con1*ssa + con2*csa;
}
/*****
kix=sin(ia); kiy=0.0; kiz=-cos(ia);
kox=sin(da); koy=0.0; koz=cos(da);
con1=klam*(kox-kix); dkz=klam*(koz-kiz); /* kiy=koy=0 */
dkx=con1*cos(sa); dky=-con1*sin(sa); /* rotate back to unrotated wing */
/*****
for(j=1;j<7;j++)
{
  clai[j]=-dot(kix,kiy,kiz,nx[j],ny[j],nz[j]);
  if(clai[j]<0) s[j]=1; /* shadowing of input beam */
  con1=acos(clai[j]);
  con3=sin(con1)/ir;
  clar[j]=sqrt(1.0-con3*con3);
}
}

/*****

```

```

void emf() /* calculate electric & magnetic fields */
{
  double ELis,ELip;
  double eLisx,eLisy,eLisz,eLipx,eLipy,eLipz;
  double eLosx,eLosy,eLosz,eLopx,eLopy,eLopz;
  double Eix,Eiy,Eiz,Hix,Hiy,Hiz;
  double kLox,kLoy,kLoz;
  double con1,con2,sroot2;
  int j;
  complex rp,rs;
  complex ELos,ELop;
  complex Eox,Eoy,Eoz,Hox,Hoy,Hoz;
  complex Etotx,Etoty,Etotz,Htotx,Htoty,Htotz;
  complex EHx,EHy,EHz;

  sroot2=1.0/sqrt(2.0);
  /* input */
  if(RtoD*pa<360) /* polarized input */
  {
    Eix=sin(pa)*cos(ia); Eiy=cos(pa); Eiz=sin(pa)*sin(ia);
    Hix=kiy*Eiz-kiz*Eiy;
    Hiy=kiz*Eix-kix*Eiz;
    Hiz=kix*Eiy-kiy*Eix;
  }
  for(j=1;j<7;j++)
  {
    cross(nx[j],ny[j],nz[j],kix,kiy,kiz);
    con2=sqrt(xcomp*ycomp+ycomp*zcomp+zcomp*xcomp);
    if(fabs(con2)<1e-30)
    {
      con2=1e-30;
      puts("WARNING: eLis zero"); getch();
    }
    eLisx=xcomp/con2; eLisy=ycomp/con2; eLisz=zcomp/con2; /* unit vector local in s */
    cross(eLisx,eLisy,eLisz,kix,kiy,kiz);
    eLipx=xcomp; eLipy=ycomp; eLipz=zcomp; /* unit vector local in p */
    if(RtoD*pa<360)
    {
      ELis=dot(Eix,Eiy,Eiz,eLisx,eLisy,eLisz); /* local s */
      ELip=dot(Eix,Eiy,Eiz,eLipx,eLipy,eLipz); /* local p */
    }
    else
    {
      ELis=sroot2; ELip=sroot2; /* normalized Jones vector */
      Eix=eLisx+eLipx; Eiy=eLisy+eLipy; Eiz=eLisz+eLipz;
      con1=sqrt(Eix*Eix+Eiy*Eiy+Eiz*Eiz);
      Eix=Eix/con1; Eiy=Eiy/con1; Eiz=Eiz/con1; /* normalize input */
      Hix=kiy*Eiz-kiz*Eiy;
      Hiy=kiz*Eix-kix*Eiz;
      Hiz=kix*Eiy-kiy*Eix;
    }
  }
  /* output electric */
  rp=(ir*clai[j] - clar[j])/(ir*clai[j] + clar[j]);
  rs=(clai[j] - ir*clar[j])/(clai[j] + ir*clar[j]);
  ELos=rs*ELis; ELop=rp*ELip;
  con1=dot(kix,kiy,kiz,nx[j],ny[j],nz[j]);

```

```

kLox=kix-2.0*nx[j]*con1;
kLoy=kiy-2.0*ny[j]*con1;
kLoz=kiz-2.0*nz[j]*con1;
cross(nx[j],ny[j],nz[j],kLox,kLoy,kLoz);
con2=sqrt(xcomp*xcomp+ycomp*ycomp+zcomp*zcomp);
if(fabs(con2)<1e-30)
{
    con2=1e-30;
    puts("WARNING: eLos zero"); getch();
}
eLos=xcomp/con2; eLosy=ycomp/con2; eLosz=zcomp/con2; /* unit vector local out s */
cross(eLosx,eLosy,eLosz,kLox,kLoy,kLoz);
eLopx=xcomp; eLopy=ycomp; eLopz=zcomp; /* unit vector local out p */
Eox=ELos*eLosx + ELop*eLopx;
Eoy=ELos*eLosy + ELop*eLopy;
Eoz=ELos*eLosz + ELop*eLopz;
Hox=kLoy*Eoz-kLoz*Eoy;
Hoy=kLoz*Eox-kLox*Eoz;
Hoz=kLox*Eoy-kLoy*Eox;
Etotx=Eox+Eix; Etoty=Eoy+Eiy; Etotz=Eoz+Eiz;
Htotx=Hox+Hix; Htoty=Hoy+Hiy; Htotz=Hoz+Hiz;
crosscom(nx[j],ny[j],nz[j],Etotx,Etoty,Etotz);
Etotx=xcomp; Etoty=ycomp; Etotz=zcomp;
crosscom(nx[j],ny[j],nz[j],Htotx,Htoty,Htotz);
Htotx=xcomp; Htoty=ycomp; Htotz=zcomp;
crosscom(kox,koy,koz,Htotx,Htoty,Htotz);
EHx=Etotx-xcomp; EHy=Etoty-ycomp; EHx=Etotz-zcomp;
crosscom(kox,koy,koz,EHx,EHy,EHz);
if(s[j]==0) { EHKx[j]=xcomp; EHKy[j]=ycomp; EHKz[j]=zcomp; }
    else { EHKx[j]=0.0; EHKy[j]=0.0; EHKz[j]=0.0; }
}
}
}
/*****
void scan()
{
    double xo,yo,z0,tb,mg;
    double th1,th2,th3,th4;
    double tt[3],t1[3],t2[3],t3[3],t4[3],t5;
    int ix,iy,iii;
    tb=tan(ba);
    /***** plane 1 *****/
    mg=tb; /* same for planes 1 & 2 & 5 */
    z0=elv;
    th1=dky+qy[1]*dkz;
    th2=dkx+qx[1]*dkz+mg*th1;
    th1=th1*wh; th2=th2*ww;
    th4=dkz*z0;
    t4[1]=cos(th4); t4[2]=sin(th4);
    t5=-wh*ww; /* same for planes 1 & 2 */
    if(fabs(th1)>1e-30)
    {
        t1[1]=(cos(th1)-1.0)/th1;
        t1[2]=sin(th1)/th1;
    }
    else
    {

```

```

    t1[1]=0.0;
    t1[2]=1.0;
    wrn=1; swrn[1]=1;
  }
  if(fabs(th2)>1e-30)
  {
    t2[1]=(cos(th2)-1.0)/th2;
    t2[2]=sin(th2)/th2;
  }
  else
  {
    t2[1]=0.0;
    t2[2]=1.0;
    wrn=1; swrn[2]=2;
  }
  cmul(t1[1],t1[2],t2[1],t2[2]);
  cmul(rcomp,icomp,t4[1],t4[2]);
  tt[1]=t5*rcomp; tt[2]=t5*icomp;
  for(ix=0;ix<px;ix=ix+2)
  {
    xo=ww*(ix-px/2.0);
    for(iy=0;iy<py;iy=iy+2)
    {
      yo=wp*(iy-py/2.0);
      th3=dkx*xo+dky*yo;
      t3[1]=cos(th3); t3[2]=sin(th3);
      cmul(t3[1],t3[2],tt[1],tt[2]);
      cint[1]=cint[1]+rcomp;
      sint[1]=sint[1]+icomp;
    }
  }
  /***** plane 2 *****/
  z0=elv+wd;
  th1=dky+qy[2]*dkz;
  th2=dkx+qx[2]*dkz+mg*th1;
  th1=th1*wh; th2=th2*ww;
  th4=dkz*z0;
  t4[1]=cos(th4); t4[2]=sin(th4);
  if(fabs(th1)>1e-30)
  {
    t1[1]=(cos(th1)-1.0)/th1;
    t1[2]=sin(th1)/th1;
  }
  else
  {
    t1[1]=0.0;
    t1[2]=1.0;
    wrn=1; swrn[3]=1;
  }
  if(fabs(th2)>1e-30)
  {
    t2[1]=(cos(th2)-1.0)/th2;
    t2[2]=sin(th2)/th2;
  }
  else
  {

```



```

    t2[1]=0.0;
    t2[2]=1.0;
    wrn=1; swrn[4]=2;
  }
  cmul(t1[1],t1[2],t2[1],t2[2]);
  cmul(rcomp,icomp,t4[1],t4[2]);
  tt[1]=t5*rcomp; tt[2]=t5*icomp;
  for(ix=0;ix<px;ix=ix+2)
  {
    xo=ww*(ix-px/2.0);
    for(iy=0;iy<py;iy=iy+2)
    {
      yo=wp*(iy-py/2.0)+wh;
      th3=dkx*xo+dky*yo;
      t3[1]=cos(th3); t3[2]=sin(th3);
      cmul(t3[1],t3[2],tt[1],tt[2]);
      cint[2]=cint[2]+rcomp;
      sint[2]=sint[2]+icomp;
    }
  }
  /***** plane 5 *****/
  z0=elv;
  th1=dky+qy[5]*dkz;
  th2=dkx+qx[5]*dkz+mg*th1;
  th1=th1*wf; th2=th2*ww;
  th4=dkz*z0;
  t4[1]=cos(th4); t4[2]=sin(th4);
  t5=-wf*ww;
  if(fabs(th1)>1e-30)
  {
    t1[1]=(cos(th1)-1.0)/th1;
    t1[2]=sin(th1)/th1;
  }
  else
  {
    t1[1]=0.0;
    t1[2]=1.0;
    wrn=1; swrn[1]=1;
  }
  if(fabs(th2)>1e-30)
  {
    t2[1]=(cos(th2)-1.0)/th2;
    t2[2]=sin(th2)/th2;
  }
  else
  {
    t2[1]=0.0;
    t2[2]=1.0;
    wrn=1; swrn[2]=2;
  }
  cmul(t1[1],t1[2],t2[1],t2[2]);
  cmul(rcomp,icomp,t4[1],t4[2]);
  tt[1]=t5*rcomp; tt[2]=t5*icomp;
  for(ix=0;ix<px;ix=ix+2)
  {
    xo=ww*(ix-px/2.0);

```

```

for(iy=0;iy<py;iy=iy+2)
{
  yo=wp*(iy-py/2.0)+2.0*wh;
  th3=dkx*xo+dky*yo;
  t3[1]=cos(th3); t3[2]=sin(th3);
  cmul(t3[1],t3[2],tt[1],tt[2]);
  cint[5]=cint[5]+rcomp;
  sint[5]=sint[5]+icomp;
}
}
/***** plane 3 *****/
mg=-tb; /* same for planes 3 & 4 & 6 */
th1=dky+qy[3]*dkz;
th2=dkx+qx[3]*dkz+mg*th1;
th1=th1*wh; th2=th2*ww;
t5=-wh*ww; /* same for plane 4 */
if(fabs(th1)>1e-30)
{
  t1[1]=(cos(th1)-1.0)/th1;
  t1[2]=sin(th1)/th1;
}
else
{
  t1[1]=0.0;
  t1[2]=1.0;
  wrn=1; swrn[5]=1;
}
if(fabs(th2)>1e-30)
{
  t2[1]=(cos(th2)-1.0)/th2;
  t2[2]=sin(th2)/th2;
}
else
{
  t2[1]=0.0;
  t2[2]=1.0;
  wrn=1; swrn[6]=2;
}
cmul(t1[1],t1[2],t2[1],t2[2]);
tt[1]=t5*rcomp; tt[2]=t5*icomp;
for(ix=1;ix<px;ix=ix+2)
{
  xo=ww*(ix-px/2.0);
  for(iy=0;iy<py;iy=iy+2)
  {
    yo=wp*(iy-py/2.0)+ww*tb;
    th3=dkx*xo+dky*yo;
    t3[1]=cos(th3); t3[2]=sin(th3);
    cmul(t3[1],t3[2],tt[1],tt[2]);
    cint[3]=cint[3]+rcomp;
    sint[3]=sint[3]+icomp;
  }
}
/***** plane 4 *****/
z0=wd;
th1=dky+qy[4]*dkz;

```

```

th2=dkx+qx[4]*dkz+mg*th1;
th1=th1*wh; th2=th2*ww;
th4=dkz*z0;
t4[1]=cos(th4); t4[2]=sin(th4);
if(fabs(th1)>1e-30)
{
    t1[1]=(cos(th1)-1.0)/th1;
    t1[2]=sin(th1)/th1;
}
else
{
    t1[1]=0.0;
    t1[2]=1.0;
    wrn=1; swrn[7]=1;
}
if(fabs(th2)>1e-30)
{
    t2[1]=(cos(th2)-1.0)/th2;
    t2[2]=sin(th2)/th2;
}
else
{
    t2[1]=0.0;
    t2[2]=1.0;
    wrn=1; swrn[8]=2;
}
cmul(t1[1],t1[2],t2[1],t2[2]);
cmul(rcomp,icomp,t4[1],t4[2]);
tt[1]=t5*rcomp; tt[2]=t5*icomp;
for(ix=1;ix<px;ix=ix+2)
{
    xo=ww*(ix-px/2.0);
    for(iy=0;iy<py;iy=iy+2)
    {
        yo=wp*(iy-py/2.0)+ww*tb+wh;
        th3=dkx*xo+dky*yo;
        t3[1]=cos(th3); t3[2]=sin(th3);
        cmul(t3[1],t3[2],tt[1],tt[2]);
        cint[4]=cint[4]+rcomp;
        sint[4]=sint[4]+icomp;
    }
}
/***** plane 6 *****/
th1=dky+qy[6]*dkz;
th2=dkx+qx[6]*dkz+mg*th1;
th1=th1*wf; th2=th2*ww;
t5=-wf*ww; /* same for plane 4 */
if(fabs(th1)>1e-30)
{
    t1[1]=(cos(th1)-1.0)/th1;
    t1[2]=sin(th1)/th1;
}
else
{
    t1[1]=0.0;
    t1[2]=1.0;

```

```

    wrn=1; swrn[5]=1;
  }
  if(fabs(th2)>1e-30)
  {
    t2[1]=(cos(th2)-1.0)/th2;
    t2[2]=sin(th2)/th2;
  }
  else
  {
    t2[1]=0.0;
    t2[2]=1.0;
    wrn=1; swrn[6]=2;
  }
  cmul(t1[1],t1[2],t2[1],t2[2]);
  tt[1]=t5*rcomp; tt[2]=t5*icomp;
  for(ix=1;ix<px;ix=ix+2)
  {
    xo=ww*(ix-px/2.0);
    for(iy=0;iy<py;iy=iy+2)
    {
      yo=wp*(iy-py/2.0)+ww*tb+2.0*wh;
      th3=dkx*xo+dky*yo;
      t3[1]=cos(th3); t3[2]=sin(th3);
      cmul(t3[1],t3[2],tt[1],tt[2]);
      cint[6]=cint[6]+rcomp;
      sint[6]=sint[6]+icomp;
    }
  }
}

//*****

void ioutpt()
{
  double con1,con2;
  double eEosx,eEosy,eEosz,eEopx,eEopy,eEopz;
  complex ax,ay,az,EEos,EEop,ESP;
  int j;
  if((as==0)&&(nrm==0))
  {
    clrscr();
    puts("SHADOWING:");
  }
  for(j=1;j<7;j++)
  {
    scint[j] = complex(cint[j],sint[j]);
  }
  for(j=1;j<7;j++)
  {
    ax=ax+EHKx[j]*scint[j];
    ay=ay+EHKy[j]*scint[j];
    az=az+EHKz[j]*scint[j];
    if((as==0)&&(nrm==0))
    {
      printf(" plane%d = %ld\n",j,s[j]);
    }
  }
}

```

```

}
eEosx=0; eEosy=1.0; eEosz=0;
cross(eEosx,eEosy,eEosz,kox,koy,koz);
eEopx=xcomp; eEopy=ycomp; eEopz=zcomp;
con1=0.5e-6/(wl*area);
EEos=dotcom(ax,ay,az,eEosx,eEosy,eEosz)*con1;
EEop=dotcom(ax,ay,az,eEopx,eEopy,eEopz)*con1;
IP=ax*conj(ax)+ay*conj(ay)+az*conj(az);
IP=IP*con1*con1;
if (abs(EEop*conj(EEop))!=0.0)
{
  ESP = EEos/EEop;
}
else
{
  ESP= complex(1e20,1e20);
}
if((as==0)&&(nrm==0))
{
  printf("\n\nOUTPUT: Es = %E + i %E\n",real(EEos),imag(EEos));
  printf("      Ep = %E + i %E\n",real(EEop),imag(EEop));
  printf("      Es/Ep = %E + i %E\n",real(ESP),imag(ESP));
  if(wrn>0)
  {
    printf("singularities (planes 1 to 6): %1d%1d %1d%1d %1d%1d %1d%1d %1d%1d\n",
           swrn[1],swrn[2],swrn[3],swrn[4],swrn[5],swrn[6],swrn[7],swrn[8],swrn[9],swrn[10],
           swrn[11],swrn[12]);
    printf("          at angle = %6.2f WL = %5.0f\n",ang,lam);
  }
  printf("\n\nOUTPUT: I = %E   NORMALIZED(%%) = %8.7f\n",real(IP),real(IP*100/In));
  getch();
}
wrn=0; lam=0.0; ang=0.0;
}

//*****

void rscan()
{
  double sta,astep,oldsa,oldpa;
  int ja,num;
  clrscr();
  puts("*****ROTATION SCAN*****");
  printf("\n\nstart rotation angle (deg) = ");
  scanf("%lG",&sta);
  sta=sta*DtoR;
  printf("step size (deg) = ");
  scanf("%lG",&astep);
  astep=astep*DtoR;
  printf("number of steps = ");
  scanf("%d",&num);
  printf("\n\nRot Ang Int(s)(%%) Int(p)(%%) Int(av)(%%)\n");
  oldsa=sa;
  oldpa=pa;
  sa=sta;
  rflg=1;as=1;
}

```

```

for(ja=1;ja<=num+1;ja++)
{
    pa=0.0;
    calc();
    IPs=IP*100.0/In;
    pa=90.0*DtoR;
    calc();
    IPp=IP*100.0/In;
    printf("%5.1f %10.7f %10.7f %10.7f\n",sa*RtoD,real(IPs),real(IPp),real((IPs+IPp)/2.0));
    if(stf==1) fprintf(outfile,"%E %E %E %E\n",sa*RtoD,real(IPs),real(IPp),real((IPs+IPp)/2.0));
    sa=sa+astep;
}
getch();
sa=oldsa;
pa=oldpa;
if(stf==1) fclose(outfile);
as=0; stf=0; rflg=0;
}

//*****

void ascan()
{
    double sta,astep,oldda;
    int ja,num;
    clrscr();
    as=1;
    puts("*****ANGLE SCAN*****");
    printf("\n\nstart diffraction angle (deg) = ");
    scanf("%lG",&sta);
    sta=sta*DtoR;
    printf("step size (deg) = ");
    scanf("%lG",&astep);
    astep=astep*DtoR;
    printf("number of steps = ");
    scanf("%d",&num);
    printf("\n\n Diff Ang   Is(%%)   Ip(%%)   Iav(%%)\n");
    oldda=da;
    da=sta;
    for(ja=1;ja<num+1;ja++)
    {
        pa=0.0;
        norm();
        calc();
        IPs=IP*100.0/In;
        pa=90.0*DtoR;
        norm();
        calc();
        IPp=IP*100.0/In;
        printf("%5.1f %10.7f %10.7f %10.7f\n",da*RtoD,real(IPs),real(IPp),real((IPs+IPp)/2.0));
        if(stf==1) fprintf(outfile,"%E %E %E %E\n",da*RtoD,real(IPs),real(IPp),real((IPs+IPp)/2.0));
        da=da+astep;
    }
    pa=0.0;
    getch();
    da=oldda;
}

```

```

    if(stf==1) fclose(outfile);
    as=0; stf=0;
}

//*****

void ascan2()
{
    double centa,offa,astep,oldda,oldia;
    int ja,num;
    clrscr();
    as=1;
    puts("*****DOUBLE ANGLE SCAN*****");
    printf("\n\n\ncentral angle da=ia (deg) = ");
    scanf("%lG",&centa);
    centa=centa*DtoR;
    printf("offset angle (deg) = ");
    scanf("%lG",&offa);
    offa=offa*DtoR;
    printf("step size (deg) = ");
    scanf("%lG",&astep);
    astep=astep*DtoR;
    num=offa*2/astep+2;
    printf("\n\n IncAng DiffAng      Is(%%)      Ip(%%)      Iav(%%)\n");
    oldda=da;
    oldia=ia;
    da=centa-offa; ia=centa+offa;
    for(ja=1;ja<num+1;ja++)
    {
        pa=0.0;
        norm();
        calc();
        IPs=IP*100/In;
        pa=90.0*DtoR;
        norm();
        calc();
        IPp=IP*100.0/In;
        printf("%5.1f %5.1f      %10.7f %10.7f
              %10.7f\n",ia*RtoD,da*RtoD,real(IPs),real(IPp),real((IPs+IPp)/2.0));
        if(stf==1) fprintf(outfile,"%E %E %E
              %E\n",ia*RtoD,da*RtoD,real(IPs),real(IPp),real((IPs+IPp)/2.0));
        da=da+astep; ia=ia-astep;
    }
    pa=0.0;
    getch();
    da=oldda;
    ia=oldia;
    if(stf==1) fclose(outfile);
    as=0; stf=0;
}

//*****

void wscan()

```

```

{
  double stw,wstep,oldwl;
  complex Is,Ip;
  int jw,num;
  clrscr();
  as=1;
  puts("*****WAVE LENGTH SCAN*****");
  printf("\n\nstart wavelength (A) = ");
  scanf("%lG",&stw);
  stw=stw*1e-10;
  printf("step size (A) = ");
  scanf("%lG",&wstep);
  wstep=wstep*1e-10;
  printf("number of steps = ");
  scanf("%d",&num);
  printf("\n\n WL          Is(%%)          Ip(%%)          Iav(%%)\n");
  oldwl=wl;
  wl=stw;
  for(jw=1;jw<num+1;jw++)
  {
    pa=0.0;
    norm();
    calc();
    Is=IP;
    IPs=IP*100.0/In;
    pa=90.0*DtoR;
    norm();
    calc();
    Ip=IP;
    IPP=IP*100.0/In;
    printf("%5.0f  %E %10.7f  %E %10.7f
           %10.7f\n",wl*1e10,real(Is),real(IPs),real(Ip),real(IPP),real((IPs+IPP)/2.0));
    if(stf==1) fprintf(outfile,"%E  %E %E  %E %E
           %E\n",wl*1e10,real(Is),real(IPs),real(Ip),real(IPP),real((IPs+IPP)/2.0));
    wl=wl+wstep;
  }
  pa=0.0;
  getch();
  wl=oldwl;
  if(stf==1) fclose(outfile);
  as=0; stf=0;
}

//*****

void stf1()
{
  char outname[20];
  clrscr();
  puts("OPEN A STORAGE FILE FOR DATA OF A SCAN");
  puts("\n\nfile is closed and deactivated after a scan");
  printf("\n\nname of storage file = ");
  scanf("%s",outname);
  outfile=fopen(outname,"w");
  stf=1;
}

```



```

//*****

void norm()
{
  double pxold,pyold,wdold,areaold,daold,iaold,elvold,eaold;
  complex con1,con2;
  elvold=elv; eaold=ea;
  pxold=px;
  pyold=py;
  wdold=wd;
  areaold=area;
  iaold=ia;
  daold=da;
  ea=0.0; elv=0.0;
  if(fabs(ia)<0.0001) ia=0.0001;
  ia=0.001;da=0.001;
  px=4; py=10;
  wd=wd*0.2e-7;
  area=px*py*ww*wp;
  nrm=1;
  calc();
  In=IP;
  if(abs(In)<1e-10)
  {
    puts("WARNING: normalization zero"); getch();
  }
  con1=sin(ia)/ir;
  con2=asin(con1);
  if(pa<1) con1=(cos(ia)-ir*cos(con2))/(cos(ia)+ir*cos(con2));
  else con1=(ir*cos(ia) - cos(con2))/(ir*cos(ia) + cos(con2));
  In=In/(con1*conj(con1));
  px=pxold;
  py=pyold;
  wd=wdold;
  area=areaold;
  ia=iaold;
  da=daold;
  ea=eaold; elv=elvold;
  nrm=0;
}

//*****

void indrefr()
{
  double l;
  l=w*1e6;
  irre=a0+l*a1+l*a2+l*a3+l*a4;
  irim=b0+l*b1+l*b2+l*b3+l*b4;
  ir = complex(irre,-irim);
}

//*****

```

APPENDIX C

Chapter 4 describes the mathematical modelling for the LIPS-structures. In this appendix the accompanying computer program, written in C++, is given. A shortcoming of the Stratton-Silver-Chu integral is that it does not give correct absolute values for the scattered intensities. One way of overcoming this is to consider the situation where the structure height is zero and the whole surface is kept at room temperature. The Fresnell coefficients for reflection from a simple flat surface are then calculated and the intensities calculated from the integral normalised to these values. This is done in the normalisation routine in the program.

/* PROGRAM StratSilverChu

Program to calculate diffraction integral of Stratton Silver Chu
 for light induced periodic surface structures (LIPS)

V6.0 June '95 Miss J E Smit

- * shadowing only on input beams
- polarized & unpolarized beams
- numerical integral v2
- singularities avoided
- marked as: wrn=11,12,21,22,31,32,41,42
- output normalized to zero profile-depth values
- * index of refr calculated for Si from polynomial
- * complex index of refraction includes conductivity
- * latent heat of fusion included */

```
#include<stdio.h>
#include<conio.h>
#include<ctype.h>
#include<math.h>
#include<complex.h>
```

```
double
xcomp,ycomp,zcomp,xcompre,xcompim,ycompre,ycompim,zcompre,zcompim,RtoD,DtoR,rcomp,icomp;
double sa=0.0,height=0.0,lecb,lect,tempb=300.0,tempt=1600.0,depth,eat=0.0,eab=0.0;
double ia,da,wl=0.6328e-6,wlpl=0.6943e-6,ll=1e-9,klam,pa=0,irre,irim,lam=0.0,ang=0.0;
double kix,kiy,kiz,kox,koy,koz,clai[200];
double x[200],z[200],nx[200],ny[200],nz[200],temp[200],ea[200],neq,conduc;
double px=2,py=40,smax=100; /* index parameters*/
double cint[200],sint[200]; /* real and imag part of integral*/
double dkx,dky,dkz,rrre,rrim,rrnre,rrnim,rr1re,rr1im,rr2re,rr2im;
double rrn1re,rrn1im,rrn2re,rrn2im;
```

```
complex ir[200];
complex clar[200],EHKx[200],EHKy[200],EHKz[200];
complex xcomp = complex(xcompre,xcompim);
complex ycomp = complex(ycompre,ycompim);
complex zcomp = complex(zcompre,zcompim);
complex rr = complex(rrre,rrim);
complex rr1 = complex(rr1re,rr1im);
complex rr2 = complex(rr2re,rr2im);
complex rrn1 = complex(rrn1re,rrn1im);
complex rrn2 = complex(rrn2re,rrn2im);
complex rrn = complex(rrnre,rrnim);
complex scint[200];
```

```
int s[200],as=0,nrm=0,rflg=0;
int rept=1,wrn=0,swrn[16];
char selct;
FILE *outfile;
FILE *infile;
```

```
double dot(double x1,double y1,double z1,double x2,double y2,double z2);
complex dotcom(complex x1,complex y1,complex z1,double x2,double y2,double z2);
void cross(double x1,double y1,double z1,double x2,double y2,double z2);
void crosscom(double x1,double y1,double z1,complex x2,complex y2,complex z2);
```

```

void mmenu();
void frame();
void probe();
void geom();
void emf();
void scan();
void calc();
void ioutpt();
void cardens();
void indrefr();
void cddiv(double x1, double y1, double x2, double y2);
void cmul(double x1, double y1, double x2, double y2);
void norm();

void main()
{
  DtoR=M_PI/180.0; RtoD=180.0/M_PI;
  ia=70.0*DtoR; da=70.0*DtoR;
  do
  { mmenu(); } while(rept==1);
}

void mmenu()
{
  nrm=0;
  clrscr();
  puts(" ***** MAIN MENU *****");
  printf("\n\n");
  puts("PRESS A KEY AS REQUIRED"); printf("\n\n");
  puts("W: LIPSS parameters      P: Probe parameters");
  puts("C: Calculate single run");
  puts("R: Calculate complex index of refraction");
  puts("Q: Quit");
  selct=toupper(getch());
  switch(selct)
  {
    case 'W' : frame() ; break;
    case 'P' : probe() ; break;
    case 'C' : norm() ; calc() ; break;
    case 'R' : indrefr(); break;
    default : break;
    case 'Q' : rept=0; break;
  }
}

//*****

double dot(double x1, double y1, double z1, double x2, double y2, double z2)
{
  return(x1*x2 + y1*y2 + z1*z2);
}

//*****

complex dotcom(complex x1, complex y1, complex z1, double x2, double y2, double z2)

```

```

{
    return(x1*x2 + y1*y2 + z1*z2);
}

//*****

void cross(double x1, double y1, double z1, double x2, double y2, double z2)
{
    xcomp=y1*z2-y2*z1; ycomp=z1*x2-z2*x1; zcomp=x1*y2-x2*y1;
}

//*****

void crosscom(double x1, double y1, double z1, complex x2, complex y2, complex z2)
{
    xccomp=y1*z2-y2*z1; yccomp=z1*x2-z2*x1; zccomp=x1*y2-x2*y1;
}

//*****

void cmul(double x1, double y1, double x2, double y2)
{
    rcomp=x1*x2-y1*y2;
    icomp=x1*y2+x2*y1;
}

//*****

void frame()
{
    int rs=1;
    do
    {
        clrscr();
        puts(" ***** STRUCTURE OF SAMPLE *****");
        printf("\n\n");
        puts("PRESS A KEY AS REQUIRED"); printf("\n\n");
        printf("E: Energies (bottom \ top) = %6.2f mJ %6.2f mJ\n\n", eab,eat);
        printf("H: Heating depth = %E m\n\n",depth);
        printf("W: Wavelength of pulsed laser = %4.0f A\n\n", wpl*1e10);
        printf("D: LIPS length = %E m\n\n",ll);
        printf("R: Rotation = %4.1f\n\n",sa*RtoD);
        puts("Q: Quit");
        selct=toupper(getch());
        switch(selct)
        {
            case 'E' : printf("Energies at bottom and top of structure (mJ) = ");
                        scanf("%lG %lG",&eab,&eat);
                        break;
            case 'H' : printf("Heating depth (m) = ");
                        scanf("%lG",&depth);
                        break;
            case 'R' : printf("Rotation angle of sample (deg) = ");
                        scanf("%lG",&sa);
                        sa=sa*DtoR;
                        break;
            case 'W' : printf("Wavelength of pulsed laser (A) = ");

```

```

        scanf("%lG",&wlp);
        wlp=wlp*1e-10;
        break;
    case 'D' : printf("Length of LIPS structure (m) = ");
        scanf("%lG", &ll);
        break;
    default : break;
    case 'Q' : rs=0; break;
}
} while (rs==1);
}

//*****

void probe()
{
int rs=1;
do
{
clrscr();
puts(" ***** PROBE BEAM PARAMETERS *****");
printf("\n\n");
puts("PRESS A KEY AS REQUIRED"); printf("\n\n");
printf("I: Inc angle = %4.1f    D: Diff angle = %4.1f\n\n",ia*RtoD,da*RtoD);
printf("N: no X-planes = %3.0f    M: no Y-planes = %3.0f\n\n",px,py);
printf("W: Wavelength = %4.0f A    P: Pol angle = %3.0f\n\n",wl*1e10,pa*RtoD);
printf("S: no divisions over one period = %3.0f\n\n",smax);
puts("Q: Quit");
selct=toupper(getch());
switch(selct)
{
case 'I' : printf("Incidence angle (deg) = ");
        scanf("%lG",&ia);
        ia=ia*DtoR;
        break;
case 'D' : printf("Diffraction angle (deg) = ");
        scanf("%lG",&da);
        da=da*DtoR;
        break;
case 'N' : printf("number of planes along X = ");
        scanf("%lG",&px);
        break;
case 'M' : printf("number of planes along Y = ");
        scanf("%lG",&py);
        break;
case 'S' : printf("number of divisions over one period = ");
        scanf("%lG",&smax);
        break;
case 'W' : printf("Wavelength (A) = ");
        scanf("%lG",&wl);
        wl=wl*1e-10;
        break;
case 'P' : printf("polarization angle in YZ-plane from Y-axis\n");
        printf("(p=90 / s=0 / un pol=400\n");
        printf("Enter angle (Deg) = ");
        scanf("%lG",&pa);

```

```

        pa=pa*DtoR;
        break;
    default : break;
    case 'Q' : rs=0; break;
    }
} while (rs==1);
}

//*****

void calc()
{
    int j;
    for(j=1;j<smax+1;j++)
    {
        cint[j]=0.0; sint[j]=0.0;
    }
    wrn=0;
    for(j=1;j<smax+1;j++) swrn[j]=0;
    klam=2.0*M_PI/wl;
    geom();
    emf();
    scan();
    ioutpt();
}

//*****

void geom() /* calculate normal-vectors, k-vectors, local angles */
{
    int j;
    double con1,con2,con4,real,imag,stap;
    complex con3 = complex(real,imag);
    /*****find n-vector*****/
    temp[1]=tempb;
    for(j=1;j<smax+1;j++)
    {
        s[j]=0; /* set all shadowing to zero */
        x[j]=(j*wlpl)/smax -wlpl/(2*smax);
        con1=(2*M_PI*x[j])/wlpl -0.5*M_PI;
        z[j]=0.5*height*(sin(con1)+1);
        con2=M_PI*(height/wlpl)*cos(con1);
        con4=atan(con2);
        nz[j]=cos(con4);
        nx[j]=-sin(con4);
        ny[j]=0.0;
    }
    /*****
    kix=sin(ia); kiy=0.0; kiz=-cos(ia);
    kox=sin(da); koy=0.0; koz=cos(da);
    dkx=klam*(kox-kix); dkz=klam*(koz-kiz);
    dky=0.0; /* kiy=koy=0 */
    /*****
    for(j=1;j<smax+1;j++)
    {
        clai[j]=-dot(kix,kiy,kiz,nx[j],ny[j],nz[j]);

```

```

    if(clai[j]<0) s[j]=1; /* shadowing of input beam */
    con1=acos(clai[j]);
    con3=sin(con1)/ir[j];
    clar[j]=sqrt(1.0-con3*con3);
}
}

//*****

void emf() /* calculate electric & magnetic fields */
{
    double ELis,ELip,rpre,rpim,rsre,rsim;
    double eLisx,eLisy,eLisz,eLipx,eLipy,eLipz;
    double eLosx,eLosy,eLosz,eLopx,eLopy,eLopz;
    double kLox,kLoy,kLoz;
    double Eix,Eiy,Eiz;
    double Hix,Hiy,Hiz;
    double con1,con2;
    int j;
    complex rp = complex(rpre,rpim);
    complex rs = complex(rsre,rsim);
    complex ELos,ELop;
    complex Eox[200],Eoy[200],Eoz[200];
    complex Hox[200],Hoy[200],Hoz[200];
    complex Etotx,Etoty,Etotz;
    complex Htotx,Htoty,Htotz;
    complex EHx,EHy,EHz;

    /* input */
    Eix=sin(pa)*cos(ia); Eiy=cos(pa); Eiz=sin(pa)*sin(ia);
    Hix=kiy*Eiz-kiz*Eiy;
    Hiy=kiz*Eix-kix*Eiz;
    Hiz=kix*Eiy-kiy*Eix;

    for(j=1;j<smax+1;j++)
    {
        cross(nx[j],ny[j],nz[j],kix,kiy,kiz);
        con2=sqrt(xcomp*xcomp+ycomp*ycomp+zcomp*zcomp);
        if(fabs(con2)<1e-30)
        {
            con2=1e-30;
            puts("WARNING: eLis zero"); getch();
        }
        eLisx=xcomp/con2; eLisy=ycomp/con2; eLisz=zcomp/con2; /* unit vector local in s */
        cross(eLisx,eLisy,eLisz,kix,kiy,kiz);
        eLipx=xcomp; eLipy=ycomp; eLipz=zcomp; /* unit vector local in p */
        ELis=dot(Eix,Eiy,Eiz,eLisx,eLisy,eLisz); /* local s */
        ELip=dot(Eix,Eiy,Eiz,eLipx,eLipy,eLipz); /* local p */
    }
    /* output electric */
    for(j=1;j<smax+1;j++)
    {
        rp=(ir[j]*clai[j] - clar[j])/(ir[j]*clai[j] + clar[j]);
        rs=(clai[j] - ir[j]*clar[j])/(clai[j] + ir[j]*clar[j]);
        ELos=rs*ELis; ELop=rp*ELip;
        con1=dot(kix,kiy,kiz,nx[j],ny[j],nz[j]);
    }
}

```



```

kLox=kix-2.0*nx[j]*con1;
kLoy=kiy-2.0*ny[j]*con1;
kLoz=kiz-2.0*nz[j]*con1;
cross(nx[j],ny[j],nz[j],kLox,kLoy,kLoz);
con2=sqrt(xcomp*xcomp+ycomp*ycomp+zcomp*zcomp);
if(fabs(con2)<1e-30)
{
  con2=1e-30;
  puts("WARNING: eLos zero"); getch();
}
eLosx=xcomp/con2; eLosy=ycomp/con2; eLosz=zcomp/con2; /* unit vector local out s */
cross(eLosx,eLosy,eLosz,kLox,kLoy,kLoz);
eLopx=xcomp; eLopy=ycomp; eLopz=zcomp; /* unit vector local out p */
Eox[j]=ELos*eLosx + ELox*eLopx;
Eoy[j]=ELos*eLosy + ELox*eLopy;
Eoz[j]=ELos*eLosz + ELox*eLopz;
Hox[j]=kLoy*Eoz[j]-kLoz*Eoy[j];
Hoy[j]=kLoz*Eox[j]-kLox*Eoz[j];
Hoz[j]=kLox*Eoy[j]-kLoy*Eox[j];
}
for(j=1;j<smax+1;j++)
{
  Etotx=Eox[j]+Eix; Etoty=Eoy[j]+Eiy; Etotz=Eoz[j]+Eiz;
  Htotx=Hox[j]+Hix; Htoty=Hoy[j]+Hiy; Htotz=Hoz[j]+Hiz;
  crosscom(nx[j],ny[j],nz[j],Etotx,Etoty,Etotz);
  Etotx=xccomp; Etoty=yccomp; Etotz=zccomp;
  crosscom(nx[j],ny[j],nz[j],Htotx,Htoty,Htotz);
  Htotx=xccomp; Htoty=yccomp; Htotz=zccomp;
  crosscom(kox,koy,koz,Htotx,Htoty,Htotz);
  EHx=Etotx-xccomp; EHy=Etoty-yccomp; EHz=Etotz-zccomp;
  crosscom(kox,koy,koz,EHx,EHy,EHz);
  if(s[j]==0) { EHKx[j]=xccomp; EHKy[j]=yccomp; EHKz[j]=zccomp; }
  else { EHKx[j]=0.0; EHKy[j]=0.0; EHKz[j]=0.0; }
}
}

//*****

void scan()
{
  double con1;
  int j;
  for(j=1;j<smax+1;j++)
  {
    con1=dkz*z[j];
    cint[j]=cos(con1);
    sint[j]=sin(con1);
  }
}

//*****

void ioutpt()
{
  double a,p,axre=0.0,axim=0.0,ayre=0.0,ayim=0.0,azre=0.0,azim=0.0;

```

```

double con1,con2,EEosre,EEosim,EEopre,EEopim;
double eEosx,eEosy,eEosz,eEopx,eEopy,eEopz,Lre,Lim;
complex ax = complex(axre,axim);
complex ay = complex(ayre,ayim);
complex az = complex(azre,azim);
complex EEos = complex(EEosre,EEosim);
complex EEop = complex(EEopre,EEopim);
complex L;
complex T;
complex Rs,Rp;
int j;
if((as==0)&&(nrm==0))
{
  clrscr();
}
for(j=1;j<smax+1;j++)
{
  scint[j] = complex(cint[j],sint[j]);
}
for(j=1;j<smax+1;j++)
{
  ax=ax+EHKx[j]*scint[j];
  ay=ay+EHKy[j]*scint[j];
  az=az+EHKz[j]*scint[j];
}
eEosx=0; eEosy=1.0; eEosz=0;
cross(eEosx,eEosy,eEosz,kox,koy,koz);
eEopx=xcomp; eEopy=ycomp; eEopz=zcomp;
con1=0.5e-6/(wl*smax);
EEos=dotcom(ax,ay,az,eEosx,eEosy,eEosz)*con1;
EEop=dotcom(ax,ay,az,eEopx,eEopy,eEopz)*con1;
if(pa<45*DtoR) rr=EEos;
if (fabs(pa-45*DtoR)<0.001)
{
  rr1=sqrt(2)*EEos;
  rr2=sqrt(2)*EEop;
}
if (pa>45*DtoR) rr=EEop;
if((as==0)&&(nrm==0))
{
  if ((fabs(pa-45*DtoR)>0.001))
  {
    printf("\n\nOUTPUT: Es = rs = %E + %E i\n",real(EEos),imag(EEos));
    printf("    Ep = rp = %E + %E i\n",real(EEop),imag(EEop));
    printf("\n\nOUTPUT: NORMALIZED r(p)s = %8.7f + %8.7f i\n",real(rr/rn),imag(rr/rn));
  }
  if (fabs(pa-45*DtoR)<0.001)
  {
    printf("\n\nOUTPUT: Es = rs = %E + %E i\n",sqrt(2)*real(EEos),sqrt(2)*imag(EEos));
    printf("    Ep = rp = %E + %E i\n",sqrt(2)*real(EEop),sqrt(2)*imag(EEop));
    printf("\n\nOUTPUT: NORMALIZED rs = %8.7f + %8.7f i\n",real(rr1/rn1),imag(rr1/rn1));
    printf("    NORMALIZED rp = %8.7f + %8.7f i\n",real(rr2/rn2),imag(rr2/rn2));
    a=350.4; p=314.7;
    con1=real(rr2/rn2)*cos((p-45)*DtoR)+imag(rr2/rn2)*sin((p-45)*DtoR);
    con2=real(rr1/rn1)*cos((p-45)*DtoR)-imag(rr1/rn1)*sin((p-45)*DtoR);
    Lre=(cos(a*DtoR)*con1/sqrt(2)) + (sin(a*DtoR)*con2/sqrt(2));
  }
}

```

```

con1=imag(rr2/rrn2)*cos((p-45)*DtoR)-real(rr2/rrn2)*sin((p-45)*DtoR);
con2=imag(rr1/rrn1)*cos((p-45)*DtoR)+real(rr1/rrn1)*sin((p-45)*DtoR);
Lim=(cos(a*DtoR)*con1/sqrt(2)) + (sin(a*DtoR)*con2/sqrt(2));
L = complex(Lre,Lim);
printf("    L = %8.7f + %8.7f i\n",real(L),imag(L));
T = L*conj(L);
printf("    TRANSMISSION = %8.9f\n",real(T));
Rs=(rr1/rrn1)*conj(rr1/rrn1);
Rp=(rr2/rrn2)*conj(rr2/rrn2);
printf("Rs = %8.9f\n",real(Rs));
printf("Rp = %8.9f\n",real(Rp));

}

getch();
}
wrn=0; lam=0.0; ang=0.0;
}

//*****

void norm()
{
double heightold,daold,iaold,con1re,con1im,con2re,con2im,con3re,con3im;
complex con1 = complex(con1re,con1im);
complex con2 = complex(con2re,con2im);
complex con3 = complex(con3re,con3im);
int j;
complex irroom;

irroom = complex(3.758,-1.494745e-2);
iaold=ia;
daold=da;
heightold=height;
if(fabs(ia)<0.0001) ia=0.0001;
ia=70*DtoR;da=70*DtoR;
height=0.0;
nrm=1;
calc();
if (fabs(pa-45*DtoR)<0.001)
{
rrn1=rr1;
rrn2=rr2;
}
else rrn=rr;
con1=sin(ia)/irroom;
con2=asin(con1);
if(pa<45*DtoR) con1=(cos(ia)-irroom*cos(con2))/(cos(ia)+irroom*cos(con2));
if (fabs(pa-45*DtoR)<0.001)
{
con1=(cos(ia)-irroom*cos(con2))/(cos(ia)+irroom*cos(con2));
con3=(irroom*cos(ia) - cos(con2))/(irroom*cos(ia) + cos(con2));
rrn1=rrn1/con1;
rrn2=rrn2/con3;
}
if (pa>45*DtoR) con1=(irroom*cos(ia) - cos(con2))/(irroom*cos(ia) + cos(con2));

```

```

rrn=rrn/con1;
ia=iaold;
da=daold;
height=heightold;
nrm=0;
}

//*****

void indrefr()
{
double arr,n[200],k[200],wstep,refl,con1,alfa[200],up[200],un[200],con3im,sigma,da;
int j,stap,num;
complex con3;

clrscr();
cardens();
/*calculate ind. refr. without conductivity*/
temp[1]=tempb;
wstep=(tempt-tempb)/49;
num=50;
for(j=1;j<num+1;j++)
{
if (temp[j]<=1685)
    alfa[j]=1340.0*exp(temp[j]/427.0)*100;
else
    alfa[j]=1e+6*100;
k[j]=(wpl*alfa[j])/(4*M_PI);
if(temp[j]<=1000)
    refl=0.324+4e-5*temp[j];
if(temp[j]>1000 & temp[j]<=1685)
    refl=0.584-4.8e-4*temp[j]+2.6e-7*temp[j]*temp[j];
if (temp[j]>1685)
    refl=0.72;
con1=(1+refl)*(1+refl)-((1-refl)*(1-refl)*(1+k[j]*k[j]));
if(temp[j]<=1685) n[j]=((1+refl)+sqrt(con1))/(1-refl);
else n[j]=((1+refl)-sqrt(con1))/(1-refl);
temp[j+1]=temp[j]+wstep;
}
for (j=1;j<((0.5*smax)+1);j++)
{
    irre=n[j]; irim=-k[j];
    ir[j] = complex(irre,irim);
    /*printf("%E    %E + %E i\n",temp[j],irre,irim);*/
}
stap=smax/2;
for(j=((0.5*smax)+1);j<smax+1;j++)
{
    irre=n[stap]; irim=-k[stap];
    alfa[j]=alfa[stap];
    temp[j]=temp[stap];
    ir[j] = complex(irre,irim);
    /*printf("%E    %E + %E i\n",temp[stap],irre,irim);*/
    stap=stap-1;
}
/*calculate ind. refr. with conductivity*/

```

```

for(j=1;j<smax+1;j++) /*calculate mobilities*/
{
  un[j]=1360*pow(temp[j]/300,-2);
  up[j]=473*pow(temp[j]/300,-2.2);
  /*printf("temp/un/up = %E %E %E\n",temp[j],un[j],up[j]);*/
}
/* calculate carrier density, conductivity and ind. ref.*/
for(j=1;j<smax+1;j++)
{
  if(temp[j]<=1685)
  {
    neq=(2e12*ea[j])/40e-9;
    conduc=1.60218e-19*neq*(un[j]+up[j]);
  }
  if(temp[j]>1685)
  {
    neq=6.02e23;
    conduc=1.25e4;
  }
  con3im=conduc/(8.85418e-14*2*M_PI*4.318e14);
  con3 = complex(0,con3im);
  ir[j]=sqrt(ir[j]*ir[j] -con3);
  /*printf("ir(%1d) = %E + %E i\n",j,real(ir[j]),imag(ir[j]));*/
}
puts("\nPress a key to continue"); getch();
}

//*****

void cardens()
{
  double ar,modul,estep,con1,d,ceat,ceab,es,e1,e2,tt1,tt2;
  int j,num,stap;
  clrscr();
  ar=M_PI*0.1*0.1; /*radius = 2mm; (units:cm2) */
  ceat=eat*1e-3/ar; /*energy density in J/cm2 */
  ceab=eab*1e-3/ar;
  modul=(ceat-ceab)/(2*(0.110/ar));
  printf("\nModulation = %E\n\n",modul);
  d=depth*100;
  tempb=(0.63*0.7*ceab)/(2.33*0.97*d); /*temp. difference*/
  tempt=(0.63*0.7*ceat)/(2.33*0.97*d);
  es=1800*2.33*ar*d; /* melting energy */
  if(tempt>1385)
  {
    e1=(ceat*ar)-0.005;
    tt1=(0.63*0.7*(e1/ar))/(2.33*0.97*d);
    do
    {
      e1=e1-0.005;
      tt1=(0.63*0.7*(e1/ar))/(2.33*0.97*d);
    } while (tt1>1385);
    tt1=1385;
    e2=(ceat*ar)-e1;
    e2=e2-es;
    if(e2>0) tt2=(0.28*0.7*(e2/ar))/(2.53*d);
  }
}

```

```
    else tt2=0;
    tempt=tt1+tt2;
}
tempb=300+tempb;
tempt=300+tempt;
lecb=3.725e-6*(1-exp(-5.88e-3*(tempb-124))) + 5.548e-10*tempb;
lect=3.725e-6*(1-exp(-5.88e-3*(tempt-124))) + 5.548e-10*tempt;
height=depth*(lect*tempt - lecb*tempb);
printf("temp = %E %E (K)\n\n",tempb,tempt);
printf("height = %E (m)\n\n",height);
ea[1]=eeab;
estep=(ecat-eeab)/49;
for(j=2;j<((0.5*smax)+1);j++)
{
    ea[j]=ea[j-1]+estep;
}
stap=smax/2;
for(j=((smax/2)+1);j<smax+1;j++)
{
    ea[j]=ea[stap];
    stap=stap-1;
}
}
}
//*****
```

BIBLIOGRAPHY

- Anderson T. F. and Richards A. G. 1942 An electron microscope study of some structural colors of insects *J. Appl. Phys.* **13** 748
- Aspnes D. E., Schwartz G. P., Studna A. A. and Schwartz B. 1981 Optical properties of GaAs and its electrochemically grown anodic oxide from 1.5 to 6.0 eV *J. Electrochem. Soc.* **128**(3) 590
- Aspnes D. E. 1987 Optical functions of intrinsic Si: Table of refractive index, extinction coefficient and absorption coefficient vs energy (0 to 400 eV); EMIS Datareview Series no. 4 RN=17807 in *Properties of Silicon* (London: INSPEC, The institution of electrical engineers) 72
- Azzam R. M. A. and Bashara N. M. 1972 Polarization characteristics of scattered radiation from a diffraction grating by ellipsometry with application to surface roughness *Phys. Rev. B* **5**(12) 4721
- Azzam R. M. A. and Bashara N. M. 1989 *Ellipsometry and polarized light* (Amsterdam: North-Holland)
- Blakemore J. S. 1982 Semiconducting and other major properties of gallium arsenide *J. Appl. Phys.* **53**(10) R123
- Botten L. C., Cadilhac M., Derrick G. H., Maystre D., McPhedran R. C., Nevière M., Petit R. and Vincent P. 1980 *Electromagnetic theory of gratings* (Berlin: Springer-Verlag)
- Brink D. J. and Smit J. E. 1993 Detection and characterization of transient surface periodic structures formed during pulsed-laser annealing of semiconductor surfaces by ellipsometry *Thin Solid Films* **233** 189
- Brink D. J., Smit J. E., Lee M. E. and Möller A. Optical diffraction by the micro structure on the wing of a moth. *Appl. Opt.* **34**(27) 6049

- Ehrlich D. J., Brueck S. R. J. and Tsao J. Y. 1982 Time-resolved measurements of stimulated surface polariton wave scattering and grating formation in pulsed-laser-annealed germanium *Appl. Phys. Lett.* **41**(7) 630
- Emel'yanov V.I. and Kashkarov P. K. 1992 Laser-induced defect formation in semiconductors *Appl. Phys.* **A55** 161
- EMI catalogue 1970: EMI South Africa (Pty) Ltd Electronic Division
- Emmony D. C., Howson R. P. and Willis L. J. 1973 Laser mirror damage in germanium at 10.6 μm *Appl. Phys. Lett.* **23**(11) 598
- Fung A. K. 1966 Scattering and depolarization of EM waves from a rough surface *Proc. IEEE* **54** 395
- Galvin G. J., Thompson M. O. and Mayer J. W. 1983 Time-resolved conductance and reflectance measurements of silicon during pulsed-laser annealing *Phys. Rev. B* **27**(2) 1079
- Ghiradella H. 1991 Light and color on the wing: structural colors in butterflies and moths *Appl. Opt.* **30**(24) 3492
- Greenewalt C. H., Brandt W. and Friel D. D. 1960 Iridescent colors of hummingbird feathers *J. Opt. Soc. Am.* **50**(10) 1005
- Guenter R. D. 1990 *Modern Optics* (New York: John Wiley & Sons)
- Hecht E. 1989 *Optics, 2nd ed.* (Reading, Massachusetts: Addison-Wesley Publishing Company)
- Land M. F. 1972 The physics and biology of animal reflectors *Progr. Biophys. molec. Biol.* **24** 75
- Marais T. K., Pretorius R., Allie M. S. and Schackleton M. O. 1990 Laser doping of silicon with antimony *S. Afr. J. Phys.* **13**(2) 111

- Mole P. J. 1987 Electron mobility at a (100) Si surface; EMIS Datareview Series no. 4 RN=15740 in *Properties of Silicon* (London: INSPEC, The institution of electrical engineers) 129
- Mole P. J. 1987 Hole mobility in bulk Si; EMIS Datareview Series no. 4 RN=15742 in *Properties of Silicon* (London: INSPEC, The institution of electrical engineers) 153
- Morris R. B. 1975 Iridescence from diffraction structures in the wing scales of *Callophrys rubi*, the green hairstreak *J. Entomol Ser.* **A49** 149
- Mossakowski D. 1979 Reflection measurements used in the analysis of structural colours of beetles *J. Microscopy* **116** 351
- Motorola catalogue: MOTOROLA Semiconductor Products Inc., Phoenix Arizona USA
- Neville A. C. and Caveney S. 1969 Scarabaeid beetle exocuticle as an optical analogue of cholesteric liquid crystals *Biol Rev.* **44** 531
- Pedrotti F. L. and Pedrotti L. S. 1993 *Introduction to Optics, 2nd ed.* (London: Prentice-Hall International Inc.)
- Reitz J. R., Milford F. J. and Christy R. W. 1979 *Foundations of electromagnetic theory, 3rd ed.* (Reading, Massachusetts: Addison-Wesley Publishing Company)
- Shvarev K. M., Baum B. A. and Gel'd P. V. 1975 Optical properties of liquid silicon *Sov. Phys. Solid State* **16**(11) 2111
- Siegman A. E. and Fauchet P. M. 1986 Stimulated Wood's anomalies on laser-illuminated surfaces *IEEE J. Quantum Electron.* **QE-22**(8) 1384
- Silver S. 1949 *Microwave antenna theory and design* (New York: McGraw-Hill)
- Sipe J. E., Young J. F., Preston J. S. and van Driel H. M. 1983 Laser-induced periodic surface structure. I. Theory *Phys. Rev. B* **27**(2) 1141
- Smith R. A. 1978 *Semiconductors, 2nd ed.* (Cambridge: Cambridge University Press)

- Soma T. and Matsuo Kagaya H. 1987 Thermal expansion coefficient of Si; EMIS Datareview Series no. 4 RN=15706 in *Properties of Silicon* (London: INSPEC, The institution of electrical engineers) 33
- Sze S. M. 1981 *Physics of Semiconductor Devices, 2nd ed.* (New York: John Wiley & Sons)
- Wood R. F., White C. W. and Young R. T. 1984 *SEMICONDUCTORS AND SEMIMETALS Volume 23: Pulsed laser processing of semiconductors* (Orlando, Florida: Academic Press, Inc.)
- Wood R. W. 1902 On a remarkable case of uneven distribution of light in a diffraction grating spectrum *Proc. Phys. Soc. (London)* **18** 269
- von Allmen M. 1980 *Laser and Electron Beam Processing of Materials* (New York: Academic Press)
- Young J. F., Preston H. M., van Driel H. M. and Sipe J. E. 1983 Laser-induced periodic surface structure. II. Experiments on Ge, Si, Al and brass *Phys. Rev. B* **27**(2) 1155
- Young J. F., Sipe J. E. and van Driel H. M. 1984 Laser-induced periodic surface structure. III. Fluence regimes, the role of feedback, and details of the induced topography in germanium. *Phys. Rev. B* **30**(4) 2001